# Experimental study of instabilities in turbulent Rayleigh Benard Convection and Path instability of rising bubbles

Viswa Maitreyi Moturi

# UNIVERSITÉ DE STRASBOURG

*ÉCOLE DOCTORALE MATHÉMATIQUES, SCIENCES DE L'INFORMATION ET DE L'INGÉNIEUR*

**[ ICUBE]**

# THÈSE présentée par :


## Viswa Maitreyi MOTURI


soutenue le : **30 Septembre 2019**

pour obtenir le grade de : **Docteur de l'université de Strasbourg**

Discipline/ Spécialité : Mécanique des Fluides

# Étude expérimentale d'instabilités à travers la convection turbulente de Rayleigh-Bénard et les instabilités de trajectoires de bulles en ascension.

**THÈSE dirigée par :**

| | |
|---|---|
| **[M FUNFSCHILLING Denis]** | Charge de recherche, ICUBE, CNRS, Strasbourg |

**RAPPORTEURS :**

| | |
|---|---|
| **[Mme SHISHKINA Olga]** | Group leader, MPI-DS, Göttingen |
| **[Mme METIVIER Christel]** | Maître de conference HDR, Université de Lorraine |

---

**EXAMINATEURS:**

| | |
|---|---|
| **[M HOARAU Yannick]** | Professeur, Université de Strasbourg |
| **[M JAN Dušek]** | Professeur, Université de Strasbourg |
| **[M WEISS Stephan]** | Group leader, MPI-DS, Göttingen |
| **[M RIMBERT Nicolas]** | Professeur, Université de Lorraine |
| **[M MOSÉ Robert]** | Professeur, ENGEES, Strasbourg |

# Acknowledgement

I would like to express my gratitude to the director of ICUBE laboratory, Dr. Michel de Mathelin for giving me the opportunity to pursue my PhD studies at ICUBE laboratory and University of Strasbourg.

I would like to thank the head of the Mechanics department of ICUBE, Prof. Yannick Hoarau for his immense encouragement and his enthusiastic attitude.

I would like to thank my supervisor Dr. Denis Funfschilling for guiding me in every step of my thesis. I have learnt a lot during my PhD career due to his excellent teaching skills and immense patience.

I would like to express my gratitude to my co-supervisor Prof. Jan Dušek for his immense support and valuable discussions during the thesis.

My sincere thanks to the team of Dr. Eberhard Bodenschatz, MPI-DS Göttingen, especially, Dr. Stephan Weiss for his guidance and valuable suggestions on the rotating Rayleigh Bénard convection experiments.

I am also grateful to Dr. Guillaume Castanet and his team at LEMTA Nancy, for their help and support in the fluorescence experiments.

I would like to express my gratitude to the jury members Dr. Olga Shishkina, Dr. Metivier Christel, Dr. Stephan Weiss, Prof. Nicolas Rimbert and Prof. Robert Mose for validating my thesis.

I would like to thank our group of “Instabilités, Turbulences, Diphasique” especially: Vincent Leautaud, Chao-Kun, Ali Al-kebsi, Anthony Ponce, Abderahmane Marouf and Mahdi Razaei. You are very kind and helpful.

I thank my friends Sathya Prakash Reddy, Dr. Pravin Badarayani, Dr. Divyesh Arora, Dr. Satya Narayanswamy, Dr. Sumedha Premi and Dr. Khyati Verma for their valuable discussions, which helped me to stay positive and optimistic during the thesis.

Last and the most important, I would like to thank my family Moturi Durga Ramalakshmi, Moturi Hari Prasada Rao, Kolli Divya Prathima, Moturi Chaitanya Deep, Bokka Siddardha and Bokka Sri Harsha for always encouraging me to achieve my dreams!

Thank you

# *Abstract*

Le développement d'instabilités fait partie des problèmes classiques de la mécanique des fluides. Les instabilités surviennent lorsqu'un écoulement régulié et organisé change pour un autre état plus complexe, voir le chaos ou la turbulence. Des phénomènes intéressants peuvent se produire lors de transitions vers le développement d'instabilités comme par exemple les allées de Von Karman. La turbulence est étudiée depuis des siècles à l'aide de modèles numériques, expérimentaux et théoriques sans que l'on ait pu percer tous ses mystères. Beaucoup de techniques expérimentales mises au point pour étudier ces transitions sont intrusives et peuvent de ce fait, modifier la dynamique de l'écoulement, d'où la nécessité de développer des techniques expérimentales non intrusives pour étudier expérimentalement les instabilités et la turbulence. Les techniques optiques sont les plus à même d'être non-intrusives tout en donnant des informations qualitatives et quantitatives sur les phénomènes physiques étudiés. A l'aide de ces techniques de visualisation, nous avons étudié le seuil, la naissance et la croissance des premières instabilités d'une bulle en ascension ainsi que la convection de Rayleight-Bénard avec ou sans rotation. Les présents travaux portent principalement sur deux problèmes courants de mécanique des fluides: la convection turbulente de Rayleigh-Bénard et l'instabilité de la trajectoire de bulles en ascension dans un liquide.

## 0.1 Structure des panaches dans la convection turbulente de Rayleigh-Bénard

La convection de Rayleigh-Bénard (RBC) est la convection qui a lieu dans un fluide chauffé par le bas par une plaque chaude et refroidi par le haut. Ce phénomène naturel est présent dans l'atmosphère terrestre, dans les océans, dans le manteau terrestre, dans la couche extérieure du soleil et des étoiles et dans de nombreuses applications industrielles telles que les échangeurs de chaleur, le dépôt chimique en phase vapeur, la convection des turbomachines, etc. Les panaches sont le principal moyen de transport de la chaleur entre les couches limites thermiques chaudes et froides en RBC. La plus grande partie du gradient thermique à travers la cellule réside dans les couches limites thermiques. Les panaches sont définis comme des blobs ou entités de fluides chaudes ou froides, générés dans les couches limites, qui respectivement s'élèvent ou s'enfoncent. Leurs mouvements sont organisés en une

circulation à grande échelle lorsque la cellule n'est pas en rotation. La différence de température entre ces panaches de fluides chauds ou froid et le fluide environnant induit une différence de densité qui à son tour induit une différence de temperature, ce qui permet de visualiser ces panaches thermiques au moyen de traceur fluorescents sensible à la température. La dynamique des panaches et de leurs propriétés ne sont pas encore complètement comprises. Les panaches thermiques peuvent être observés par ombroscopie Funfschilling et al., 2004, mais les informations sur leurs températures obtenues par cette technique restent qualitatives. La température des panaches peut être mesurée par de petites thermistances, mais elles ne fournissent que des informations locales limitées. Les panaches thermiques peuvent également être visualisés par des cristaux liquides thermochromiques Zhou et al., 2007 mais seulement sur une plage de température trés limitée. D'où la nécessité de mettre au point une technique expérimentale efficace et non intrusive pour visualiser et caractériser le champ de température des panaches.

En présence de rotation, l'écoulement dans une cellule de Rayleigh-Bénard en convection turbulente, change radicalement par rapport à la convection sans rotation en raison de la force de Coriolis induit par la rotation. En rotation, les panaches subissent le pompage d'Ekman et la succion d'Ekman, et de ce fait, ils émergent de la couche limite en développant une vorticité pour conserver le moment angulaire Vorobieff et al., 2002. Les panaches verticaux forment des colonnes verticales ayant une vorticité. A vitesse de rotation élevée, ces colonnes de vorticité verticale s'étendent sur l'ensemble de la hauteur de la cellule. Des études récentes montrent que la transition d'un régime de circulation à grande échelle au régime de colonnes verticales de vortex ne se produit pas dès la mise en rotation, et n'intervient qu'après un taux de rotation critique, défini par le nombre de Rossby $Ro = \sqrt{(\beta g \delta T / h)}/2\Omega$, $\Omega$ est la vitesse de rotation, h la hauteur de la cellule, $\beta$ est le coefficient d'expansion thermique, et g est la gravité (Vorobieff et al., 2002, Kunnen et al., 2008 Rajaei et al., 2016). La valeur critique du nombre de Rossby à laquelle cette transition se produit et a un effet sur le champ d'écoulement et le transport de chaleur ne sont pas encore complètement compris.

Dans cette étude, deux techniques expérimentales $(i)$ la fluorescence induite par nappe laser (PLIF) (Labergue et al., 2012, Sakakibara et al., 1999) et $(ii)$ la vélocimétrie par image de particules (PIV) sont mises en oeuvre pour visualiser et caractériser le mouvement du panache dans la convection de

Rayleigh-Bénard avec ou sans rotation. Les expériences sont réalisées à différentes valeurs des nombre de Rayleigh, Rossby et Prandtl. Les résultats de PIV sont utilisés pour calculer le champ de vitesse instantané dans un plan coupant la cellule en deux, toute en passant par son axe de symétrie. La cellule RBC est constituée d'une cellule cylindrique de 10 cm de diamètre et de rapport d'aspect (hauteur/largeur) de 1. La plaque inférieure de la cellule est en cuivre et est chauffée par un fil résistif par effet Joule, tandis que la plaque supérieure est en saphir et est refroidie par bain thermostaté. La cellule de Rayleigh-Bénard est montée sur une table tournante pour les expériences en rotation. Dans l'expérience de vélocimétrie par image de particules (PIV), le fluide est inséminé par des billes de verre creuses argentées de 10 $\mu$m de diamètre et la cellule est éclairée par une nappe laser verte (532 nm) passant par le plan vertical central. Les images sont obtenues à l'aide d'une caméra à grande vitesse Phantom Miro. La structure de l'écoulement dépend du nombre de Rossby qui se défini comme le rapport de la force d'inertie à la force de Coriolis. La fluorescence induite par laser (LIF) (Sakakibara et al., 1999) est utilisée pour mesurer le champ de température lors de la transition d'un régime de circulation à grande échelle aux régimes de convections dominés par la rotation où l'on observe la présence de colonnes. Les colorants fluorescents Rodamine 560 et Keton Red sont mélangés à l'eau à des concentrations respectives de $10^{-5}$ et $2.5x10^{-6}$ mol/l. Deux filtres à bande spectrale étroite 475 - 525 nm et 595 - 605 nm sont utilisés pour sélectionner une bande de fluorescence de la Rhodamine 560 et de la Keton Red respectivement.

**Champ de vitesses**

Dans notre étude, nous avons mesuré le champ de vitesse dans le plan médian vertical de la cellule RBC. La figure 1 montre que l'écoulement passe d'une circulation à grande échelle dans le cas sans rotation, à un régime colonnes verticales dans le régime affecté par la rotation (i.e. $0.15 < \mathrm{Ro} < 2.5$). Pour comprendre cette transition et être plus quantitatif, les composantes horizontales et verticales des vecteurs vitesses sont corrélées entre des positions situées près des plaques supérieure et inférieure de la cellule (respectivement à 5 % et 95 % de la hauteur des cellules). D'après la figure 2 les composantes horizontales des vecteurs vitesses proches des couches limites hautes et le basses de la cellule de Rayleigh-Bénard sont en opposition de phase, tandis que les composantes horizontales des vecteurs vitesses sont en phases dans le régime dominé par la rotation où des colonnes de vorticité sont présentes. Les colonnes de vorticité verticales sont alimentées par le

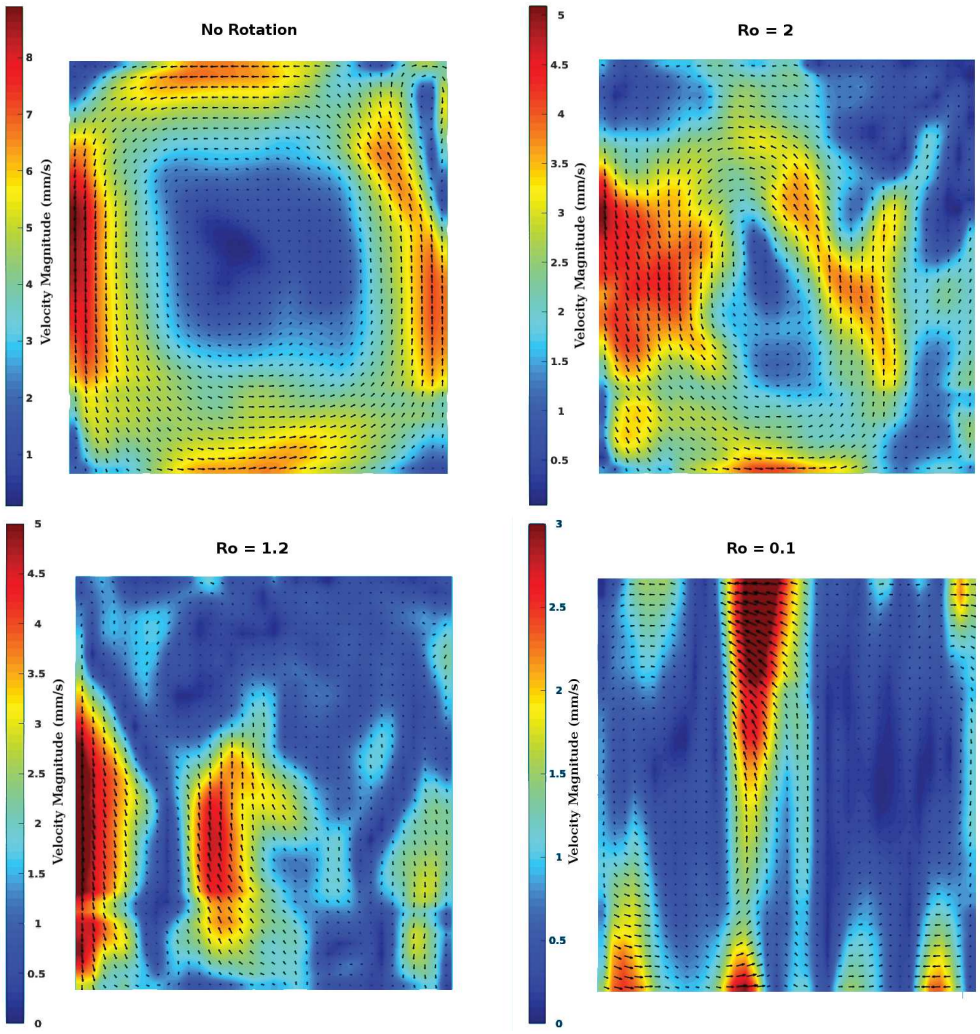


FIGURE 1: Champ de vitesse moyenne (sur 67secondes) et contour de la norme des vecteurs vitesses à Ro = ∞ (haut à gauche, pas de rotation), Ro = 2 (haut à droite ), Ro = 1.2 (bas à gauche) et Ro = 0.1(bas à droite).

pompage d'Ekman. Elles se développent à partir des couches limites thermiques et s'étendent progressivement de la plaque inférieure ou supérieure vers le milieu de la cellule. A plus forte vitesse de rotation, ces colonnes de vorticité se rejoignent et s'étendent sur toute la hauteur de la colonne. Les colonnes ont des vorticités verticales mais tournant dans des directions opposées. Cela a été prédit théoriquement dans les études précédentes, mais à notre connaissance, c'est la première fois que ce changement de vorticité a été observé expérimentalement.

Le nombre de colonnes augmente avec une diminution du nombre de Rossby. L'auto-corrélation spatiale de la composante verticale de la vitesse est effectuée pour différents nombres de Rossby afin de définir la taille des colonnes.

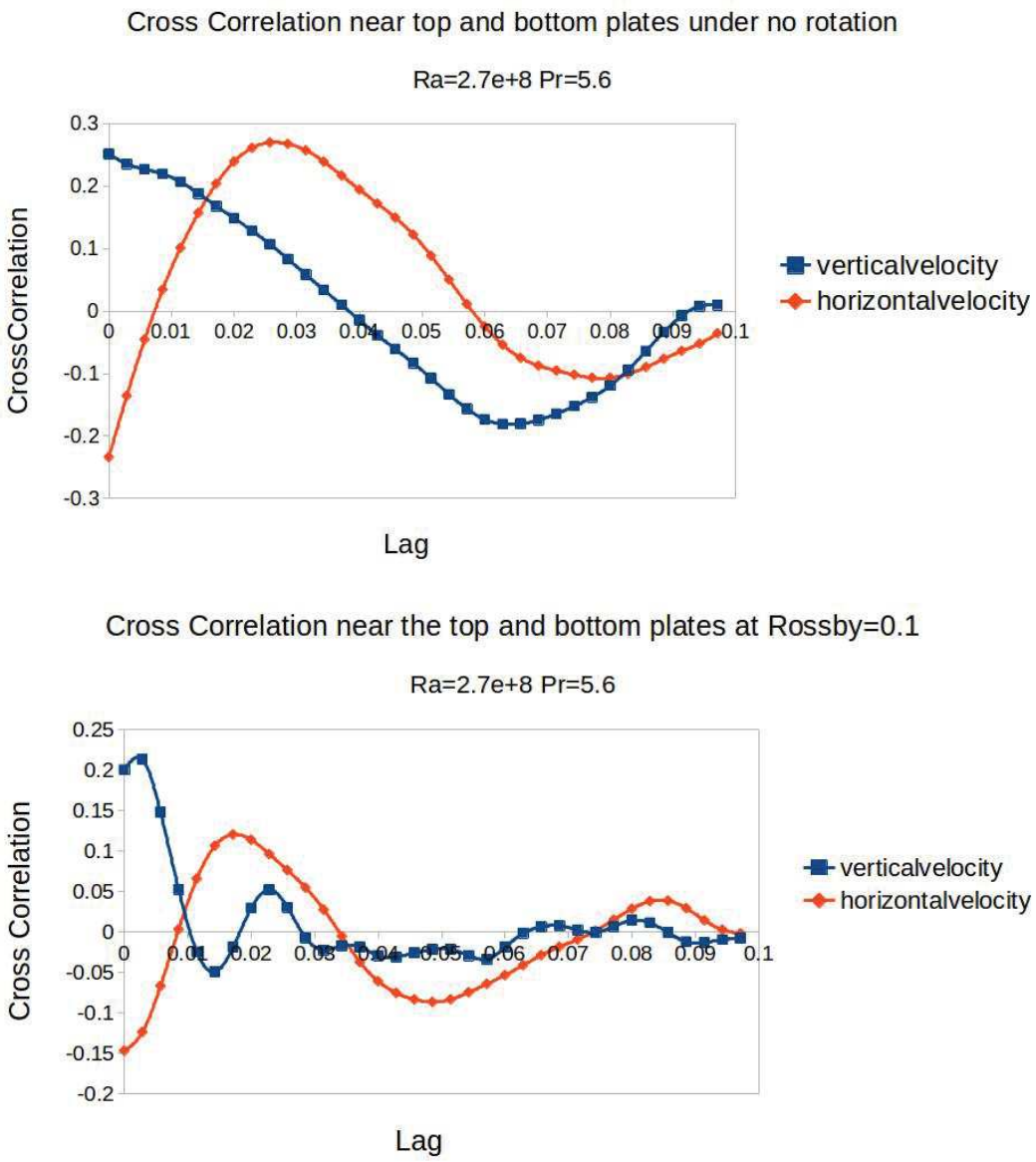


FIGURE 2: Cross corrélation des composantes horizontales et verticales des vecteurs vitesses entre le haut et le bas de la cellule respectivement à Ro = ∞ (haut) et Ro = 0,1 (bas).

D'après la figure 3, on observe une rupture de pente significative lors de la transition du régime non-affecté par la rotation (Ro > 2,5) au régime affecté par la rotation (0,1 < Ro < 2,5). La décorrélation maximale est observé pour le régime non affecté par la rotation (i.e. lorsque les vitesses de rotation sont faibles). Dans le plan vertical contenant l'axe de symétrie de la cellule, les colonnes sont alternativement ascendantes et descendantes et sont constituées respectivement des panaches chauds ascendants en formant un vortex et des panaches froids descendant aussi en formant un vortex. Le premier minimum de l'autocorrélation de la composante verticale du vecteur vitesse

définit la largeur des colonnes. Pour les petits nombres de Rossby, le minimum de l'auto-correlation est à peu près le même pour tous les nombres de Rayleigh. Ceci suggère qu'au-dessus d'une certaine vitesse de rotation, la largeur des colonnes reste constante, et qu'il y a une limite à la taille minimale des colonnes qui peuvent se former à l'intérieur d'une cellule RBC.

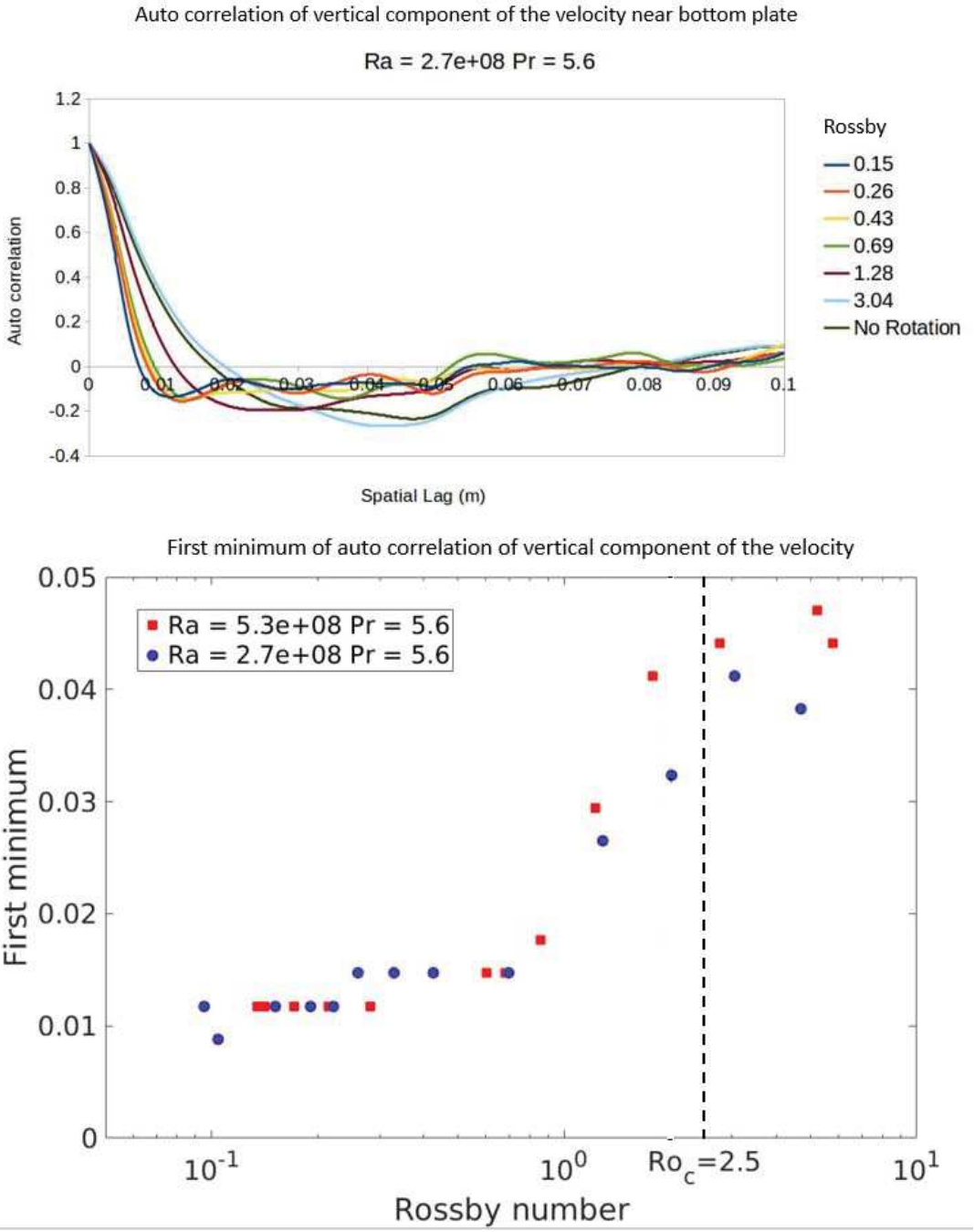


FIGURE 3: Auto corrélation de la composante verticale du vecteur vitesse à divers nombres de Rossby (en haut) et localisation premier minimum de l'autocorrélation (en bas).

Les fluctuations de vitesse sont un marqueur important de l'hydrodynamique

présente dans la cellule. Ainsi, les fluctuations de vitesse dans le régime non affecté par la rotation augmentent avec une diminution du nombre de Rossby jusqu'à la transition vers le régime affecté par la rotation. Après cette transition vers le régime affecté par la rotation, les fluctuations de vitesse diminuent avec une diminution du nombre de Rossby comme représenté sur la figure 4. Les fluctuations se développent d'abord aux abords des couches limites supérieures et inférieures. En effet, le pompage Ekman induit de grandes fluctuations au cours du développement des colonnes verticales qui se propagent à partir des couches limites vers le « bulk » i.e. le centre de la cellule. Les fluctuations de vitesse sont anisotropiques : les fluctuations de la composante verticale de la vitesse sont bien plus importantes que les fluctuations de la composante horizontale de la vitesse. L'anisotropie des fluctuations est également spatiale. Les fluctuations à mi-hauteur sont significativement différentes des fluctuations de vitesse proche des plaques supérieure et inférieure. En effet, les fluctuations horizontales sont plus grandes près des plaques supérieure et inférieure en raison de la forte vorticité provenant du pompage d'Ekman. Le changement de direction de la vorticité dans le plan médian horizontal de la cellule, explique la légère augmentation des fluctuations de la composante verticale de la vitesse à mi-hauteur, comparé aux fluctuations de la composante verticale de la vitesse près des plaques supérieure et inférieure.

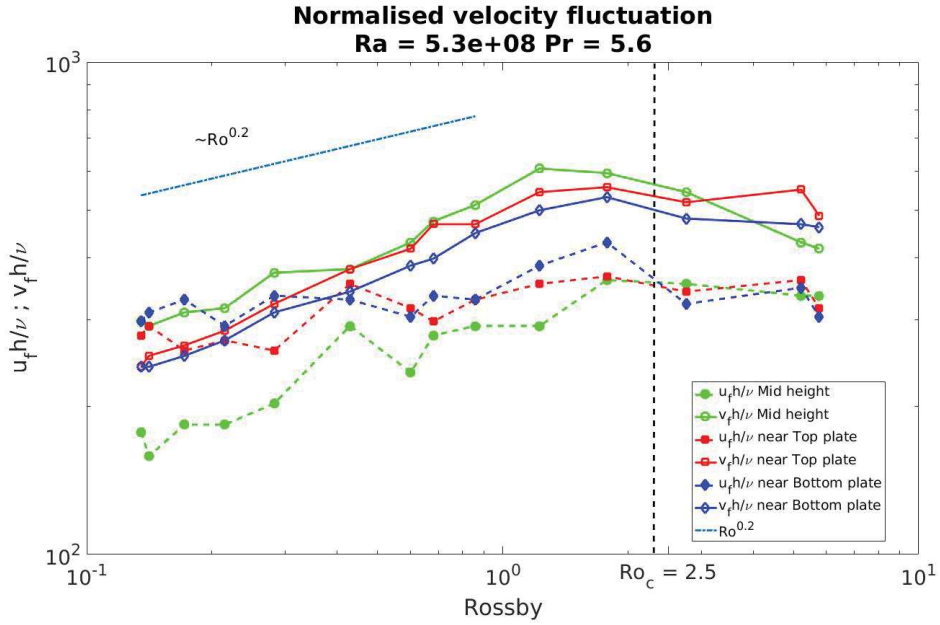


FIGURE 4: Fluctuation normalisée de la vitesse en fonction du nombre de Rossby à différentes hauteurs dans la cellule RBC.

**Conclusion**

Les panaches dans la convection de Rayleigh Bénard sont visualisés expérimentalement à l'aide des techniques PIV et PLIF dans le plan vertical central dans une cellule de Rayleigh-Bénard avec ou sans rotation. Le champ de vitesse passe d'une circulation à grande échelle dans le régime non affecté par la rotation à un régime champ de vitesse composé de colonnes de vortex verticales dans le régime affecté par la rotation. Les résultats obtenus sont en accord avec les résultats expérimentaux obtenus précédemment par Kunnen et al., 2008 et Rajaei et al., 2016. Notre étude a permis d'avoir une vue plus globale sur l'hydrodynamique de la cellule en rotation ou pas. En comparant la vitesse dans les régions proches des plaques supérieure et inférieure, la composante horizontale de la vitesse est en opposition de phase tandis la composante verticale de la vitesse est en phase. Ceci montre par observation expérimentale que les colonnes de vorticité verticales, par ailleurs typique de la convection de Rayleigh-Bénard en régime dominé par la rotation, changent de direction de vorticité lorsqu'elles traversent le plan médian de la cellule. Les fluctuations de vitesse sont anisotropes et suivent une loi d'échelle de type $Ro^{0.2}$ dans le régime affecté par la rotation.

## 0.2 Instabilités de la trajectoire des bulles en ascension

A partir d'une certaine taille, les bulles en ascension dans un liquide subissent une première instabilité de leur trajectoire suivie par d'autres. Les petites bulles s'élèvent en ligne droite. Au-delà d'une taille critique des bulles, elles montent en oscillant. Le nombre de Bond (rapport des forces gravitationnelles à la tension superficielle) et le nombre de Galileo (rapport de la force gravitationnelle à la force visqueuse) sont les paramètres permettant de définir les courbes de stabilité marginale et les différents domaines d'instabilités d'une bulle en ascension. Jusqu'à récemment, il était admis que les instabilités dans le sillage de la bulle étaient les seules responsables de l'instabilité de la trajectoire (Zenit et al., 2008). Mais une étude récente a montré que l'instabilité de la trajectoire ne résultait pas toujours d'une instabilité de sillage (Cano-Lozano et al., 2013). La déformation de la bulle joue également un rôle important dans la détermination du seuil de transition de la trajectoire rectiligne à la trajectoire oscillante (Zhou et al., 2017). La courbe de stabilité marginale n'est pas non plus très bien définie et la littérature existante montre des divergences importantes. Pour cette raison, une étude expérimentale est nécessaire pour acquérir de nouvelles données fiables.

Dans notre étude, l'instabilité de trajectoire d'une bulle est étudiée expérimentalement dans de l'eau déminéralisée ainsi que dans des huiles de silicone de différentes viscosités (5cst, 10cst, 500cst) dans un canal rectangulaire. Une électrovanne et un réservoir d'air sous pression sont utilisés pour injecter les bulles d'air de taille variable dépendant de la pression dans le réservoir. Dans notre étude, nous avons observé la transition d'une trajectoire rectiligne vers des trajectoires hélicoïdales et ou en zigzag. Nos résultats expérimentaux nous ont permis d'obtenir quatre points de la courbe de stabilité marginale. Dans le cas de l'eau et de l'huile de silicone 5cst, on obtient un très bon accord avec les résultats numériques de Zhou et Dusek 2017. Nos observations donnent un nombre Galileo critique inférieur pour l'huile de silicone de viscosité de 10cst. Les résultats de l'expérience montrent une augmentation parabolique de l'amplitude de l'oscillation en $\sqrt{Ga}$ ainsi qu'une bifurcation de Hopf super-critique La fréquence non dimensionnelle des oscillations est également en accord avec les simulations numérique de Zhou et Dusek 2017.

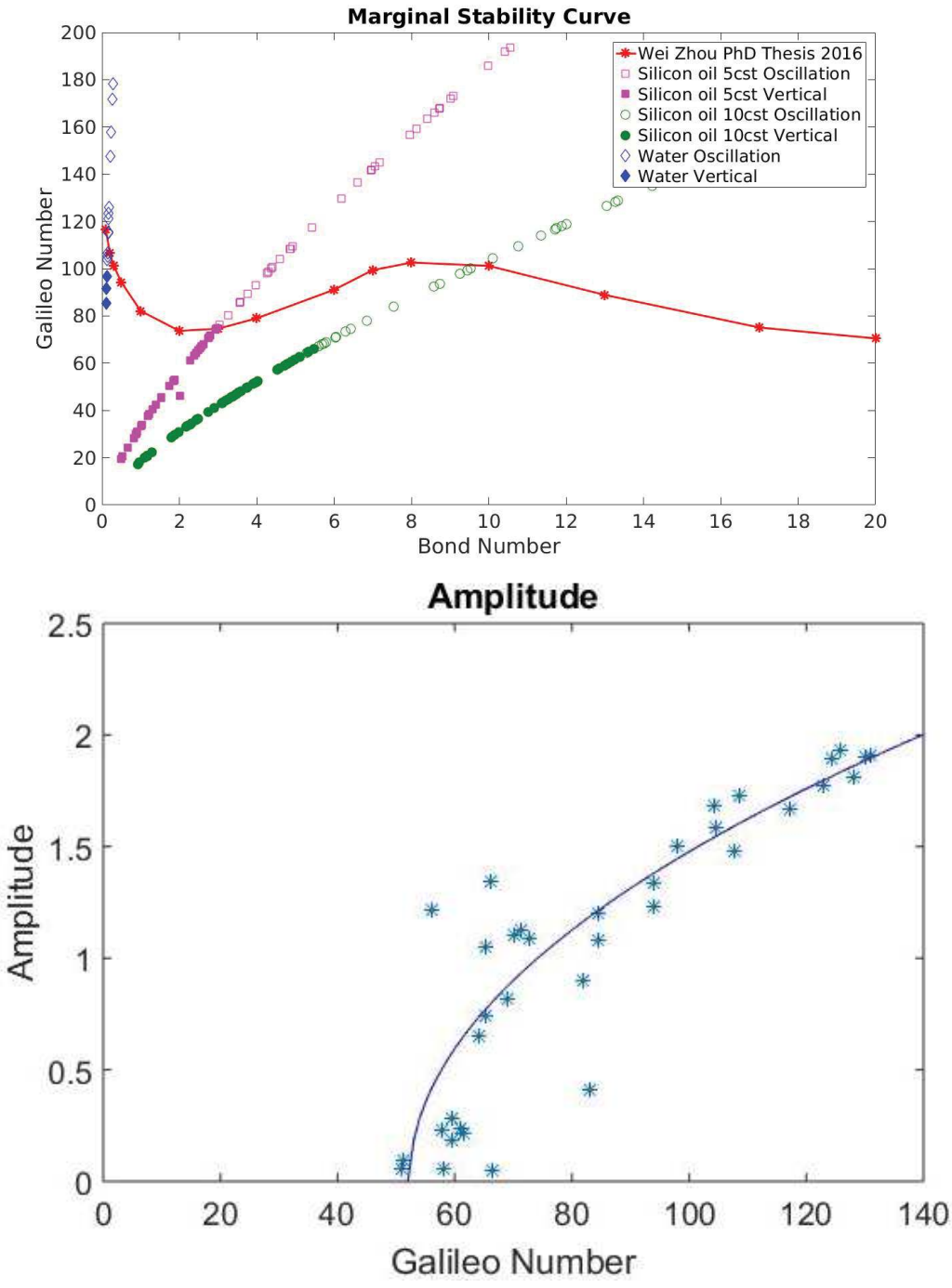


FIGURE 5: Courbe de stabilité marginale (haut) ; Amplitude des oscillations (bas).

# Contents

**Abstract** **v**

0.1 Structure des panaches dans la convection turbulente de Rayleigh-Bénard . . . . . v

Champ de vitesses . . . . . vii

Conclusion . . . . . xii

0.2 Instabilités de la trajectoire des bulles en ascension . . . . . xiii

**List of Figures** **xix**

**List of Tables** **xxv**

**List of Abbreviations** **xxvii**

**List of Symbols** **xxix**

**1 Introduction** **1**

1.1 Rayleigh Bénard Convection . . . . . 1

1.2 Rotating Rayleigh Bénard Convection . . . . . 7

1.3 Equations of Motion . . . . . 8

1.3.1 Oberbeck Boussinesq approximation . . . . . 9

1.3.2 Equations of Motion in rotating Rayleigh Bénard Convection . . . . . 11

1.3.3 Non Dimensional Parameters . . . . . 12

1.4 Boundary Layers . . . . . 14

1.4.1 Prandtl Boundary Layer . . . . . 15

1.4.2 Grossmann Lohse Theory . . . . . 16

1.4.3 Ekman Boundary Layer . . . . . 17

1.4.4 Ekman Suction and Ekman Pumping . . . . . 18

1.4.5 Stewartson Boundary Layer . . . . . 18

1.5 Flow Transition . . . . . 20

1.5.1 Non Rotating Rayleigh Bénard Convection . . . . . 20

Oscillations of LSC . . . . . 20

Reversals of LSC . . . . . 21
Single roll and Double roll LSC . . . . . 21
1.5.2 Rotating Rayleigh Bénard Convection . . . . . 21
Rotation unaffected regime (Ro > 2.5 ; Regime I) . . . . 22
Rotation affected regime (0.1 < Ro < 2.5 ; Regime II) . . 23
Rotation Dominated Regime (Ro < 0.1 ; Regime III) . . 24
Determination of Critical Rossby . . . . . 24

**2 Experimental Methods** **27**
2.1 Introduction . . . . . 27
2.2 Planar Laser Induced Fluorescence . . . . . 27
2.2.1 Principle of Fluorescence . . . . . 28
2.2.2 Measurement Principle . . . . . 30
2.2.3 Temperature Calibration . . . . . 31
1 Dye 2 Bands Fluorescence technique . . . . . 33
2 Dyes 2 Bands Fluorescence technique . . . . . 33
2.2.4 Fluorescent dye properties . . . . . 34
2.2.5 Fluorescence Spectrum . . . . . 35
2.3 Experiment Setup . . . . . 39
2.3.1 Convection Cell . . . . . 39
2.3.2 LIF Experiment Setup . . . . . 40
2.3.3 LIF experiment procedure . . . . . 41
2.4 Particle Image Velocimetry . . . . . 45
2.4.1 Measurement Principle . . . . . 45
2.5 PIV Experiment Setup . . . . . 46

**3 Velocity Statistics in Rotating Rayleigh Bénard Convection** **49**
3.1 Introduction . . . . . 49
3.2 Mean Velocity Flow Field . . . . . 49
3.3 Strength of LSC . . . . . 52
3.4 Velocity near the top and bottom plate . . . . . 56
3.5 Spatial Velocity Cross-correlation . . . . . 61
3.5.1 Cross-correlation of horizontal component of the velocity . . . . . 62
3.5.2 Cross-correlation of vertical component of the velocity 64
3.6 Spatial Velocity Auto-correlation . . . . . 69
3.7 Velocity Fluctuation Field . . . . . 73
3.8 Onset of convection . . . . . 79
3.9 Conclusion . . . . . 81

**4 Temperature field in Rayleigh Bénard convection** **83**
4.1 Introduction . . . 83
4.2 Temperature contours . . . 83
4.2.1 Without rotation . . . 83
4.2.2 With rotation . . . 86
4.3 Conclusion . . . 90

**5 Path instability of rising bubbles** **91**
5.1 Abstract . . . 91
5.2 Introduction . . . 92
5.2.1 Mathematical Formulation . . . 93
5.2.2 Non Dimensional Numbers . . . 94
5.2.3 Objective of present work . . . 95
5.3 Experimental Setup . . . 96
5.4 Bubble flow Regimes . . . 98
5.4.1 Rectilinear regime . . . 98
5.4.2 Planar Zigzag regime . . . 99
5.4.3 Helical regime . . . 101
5.5 Marginal Stability Curve . . . 101
5.6 Frequency and Amplitude of oscillation . . . 103
5.7 Conclusion and Perspective . . . 103

**6 Conclusion** **107**
6.1 Rayleigh Bénard Convection . . . 107
6.2 Instability of rising bubbles . . . 110
6.3 Perspectives . . . 111

**Bibliography** **113**

# List of Figures

1 Champ de vitesse moyenne (sur 67secondes) et contour de la norme des vecteurs vitesses à Ro = ∞ (haut à gauche, pas de rotation), Ro = 2 (haut à droite ), Ro = 1.2 (bas à gauche) et Ro = 0.1(bas à droite). . . . . viii
2 Cross corrélation des composantes horizontales et verticales des vecteurs vitesses entre le haut et le bas de la cellule respectivement à Ro = ∞ (haut) et Ro = 0,1 (bas). . . . . ix
3 Auto corrélation de la composante verticale du vecteur vitesse à divers nombres de Rossby (en haut) et localisation premier minimum de l'autocorrélation (en bas). . . . . x
4 Fluctuation normalisée de la vitesse en fonction du nombre de Rossby à différentes hauteurs dans la cellule RBC. . . . . xi
5 Courbe de stabilité marginale (haut) ; Amplitude des oscillations (bas). . . . . xiv

1.1 Whole mantle convection model ; Image source: Pearson Prentice Hall Inc, 2009. . . . . 1
1.2 The Solar interior of the Sun. Image source: NASA. . . . . 2
1.3 Bénard cells observed from top view, by Henri Bénard, 1900 in his convection experiment . . . . . 3
1.4 Shadowgraph technique. Plume visualized from the top view of RBC cell by Funfschilling et al., 2004 (left); Transient large scale flow from front view by Xi et al., 2004 (right). . . . . 5
1.5 Thermochromic liquid crystal microsphere image of sheet plumes 2mm (a) and 2cm (b) from the top plate of RBC cell by Zhou et al., 2010 . . . . . 5
1.6 Instantaneous temperature fields at $Ra = 10^8$ and $\Delta T = 40C$ for NOB studies. Pink represents temperature above mean temperature and blue represents temperature below mean temperature. Horn et al., 2014 . . . . . 10

1.7 Boundary layer and bulk partition given by Grossmann et al., 2000. Kinetic boundary layer (left) Thermal boundary layer (right) . . . 16
1.8 Ekman Transport Image source: David Beesley et al, Oceanography Vol 21 BEEsLEy et al., 2008. . . . 19
1.9 Normalized heat transfer as a function of Rossby number on logarithmic scale. (Taken from references Rajaei et al., 2016 Stevens et al., 2009 Zhong et al., 2010) . . . 22
1.10 A perspective sketch of path of a fluid particle in square cell under rotation by Veronis, 1959 . . . 23
1.11 Relative Nusselt variation with inverse Rossby observed by Wei et al., 2015 at Pr = 4.38 and Ra= 1.8 x $10^{10}$ . . . 24
1.12 Temperature field in horizontal mid plane of RBC cell of $\gamma$ = 2, by Stevens et al., 2010b at Pr = 4.38 and Ra= 2.91 x $10^{8}$ left $1/Ro = 0.046$ and right $1/Ro = 0.6$ . . . 25

2.1 Jablonski Diagram. . . . 28
2.2 FLuorescent Spectrum of Rhodamine560 and Kiton Red. . . . 36
2.3 Fluorescent Emission Spectrum. . . . 36
2.4 Fluorescent intensity of Rhodamine560 in function of the temperature. . . . 37
2.5 Fluorescent intensity of Kiton Red in function of the temperature. . . . 37
2.6 FLuorescent intensity ratio of Rhodamine560/ Kiton Red in function of the temperature. . . . 38
2.7 Rayleigh Bénard Convection Cell. . . . 40
2.8 Laser Induced Fluorescence experimental Setup. . . . 41
2.9 Images of both cameras before transformation. . . . 42
2.10 Location of centers of two images (left).Transformed Image 2 (right) . . . 42
2.11 Images division removes illumination defects . . . 43
2.12 Rotating experimental Setup. . . . 44
2.13 Particle Image Velocimetry experiment Setup. . . . 47

3.1 Mean Velocity Flow field averaged over 67 seconds with velocity magnitude represented in the contour at Ra = 2.7e+08, Pr = 5.6 and at various Rossby numbers . . . 50

3.2 (a,b) Top view of vorticity near the top and bottom boundary layers (c) Oscillatory vertical column Ribeiro et al Ribeiro et al., 2015 . . . . . 51
3.3 Calculation of strength of LSC in the plane of measurement (Schematic representation), R = 47mm . . . . . 52
3.4 Time averaged strength of large scale circulation in the plane of observation at various Rossby values. . . . . 53
3.5 Temporal evolution of the estimated strength of LSC in the plane of observation at Ro = ∞ (bottom), Ro = 2.7 (middle) Ro = 0.4 (top ). . . . . 54
3.6 Instantaneous horizontal velocity at Ro = 0.1 , Ra = 2.7e+08 . . 56
3.7 Instantaneous Vertical velocity at Ro = 0.1 , Ra = 2.7e+08 . . . 57
3.8 Vertical positions considered for velocity comparison ( The cell is 100mm in height and a diameter of 100mm ). . . . . 58
3.9 Horizontal velocity evolution in time at various heights for Ra = 2.7e+08, Pr = 5.6 and at Ro = 0.1 . . . . . 58
3.10 Horizontal velocity evolution in time at various heights for Ra = 2.7e+08, Pr = 5.6 and at Ro = 0.4. . . . . 59
3.11 Vertical velocity evolution in time at various heights for Ra = 2.7e+08, Pr = 5.6 and at Ro = 0.1. . . . . 59
3.12 Vertical velocity evolution in time at various heights for Ra = 2.7e+08, Pr = 5.6 and at Ro = 0.4 . . . . . 60
3.13 Cross correlation between the horizontal component of the velocity located near the top and bottom plates for rotation affected regime Ro < 1 (bottom) and rotation unaffected regime Ro > 1 (top). . . . . 62
3.14 Cross correlation between the horizontal component of the velocity located near the top and bottom plates for Ro = 0.1 at Ra = 5.3e+08, 2.7e+08, 1.4e+08. . . . . 63
3.15 Mean Cross correlation of horizontal velocity located near the top and bottom plates at Ra = 5.3e+08 and 2.7e+08. . . . . 64
3.16 Cross correlation between the vertical component of velocity located near the top and bottom plates for Ro > 1 (top) and Ro < 1 (bottom). . . . . 65
3.17 Mean cross correlation of the vertical component of the velocity located near top and bottom plates at Ra = 5.3e+08 and 2.7e+08 . . . . . 66

3.18 Horizontal and vertical component of the velocity cross correlation at $Ro = \infty$ (No rotation) and Ra = 5.3e+08 (top), 2.7e+08 (bottom) . . . . . 67
3.19 Horizontal and vertical component of the velocity cross correlation at Ro = 0.1 and Ra = 5.3e+08 (top), 2.7e+08 (bottom) . . 68
3.20 Auto correlation of vertical component of the velocity near bottom plate at Ra = 5.3e+08 (top) and 2.7e+08 (bottom) for different Rossby numbers . . . . . 70
3.21 Auto correlation of vertical component of the velocity near the top plate at Ra = 5.3e+08 (top) and 2.7e+08 (bottom) for different Rossby numbers . . . . . 71
3.22 First Minimum of auto correlation curves plot at the bottom 5% of the cell height for Ra = 5.3e+08 and 2.7e+08. . . . . 72
3.23 Vertical velocity fluctuation at Ro = 4.68 (top), Ro = 2 (middle) and Ro = 0.1 (bottom) for Ra = 2.7e+08. . . . . 74
3.24 Horizontal velocity fluctuation at Ro = 4.68 (top), Ro = 2 (middle) and Ro = 0.1 (bottom) for Ra = 2.7e+08.. . . . . 75
3.25 Mean horizontal velocity fluctuation at various heights for Ra = 5.3e+08 for different Rossby numbers. . . . . 76
3.26 Normalized horizontal fluctuation with Rossby at Ra = 5.3e+08 77
3.27 Ratio of horizontal and vertical fluctuation with Rossby at Ra = 5.3e+08. . . . . 78
3.28 Horizontal and vertical velocity fluctuations at mid height for Ra = 5.3e+08 and 2.7e+08 . . . . . 79
3.29 Mean velocity flow field at a rotation rate of 2.7 rad/s and for Ra = 8.2e+07, 9.84e+07, 1.15e+08 and 1.3e+08 . . . . . 80
3.30 Mean vertical velocity at various Rayleigh numbers and at a rotation rate of 2.7 rad/s . . . . . 80

4.1 Instantaneous temperature field without rotation at $\Delta T = 30°C$ and Ra = 8.6e+08. Images are 10s apart. . . . . 84
4.2 Instantaneous temperature field without rotation at $\Delta T = 10°C$ and Ra = 2.7e+08. Images are 10s apart. . . . . 85
4.3 Instantaneous temperature field at Ro = 1.9, $\Delta T = 30°c$ and Ra = 8.6e+08. Images are 10s apart. . . . . 87
4.4 Instantaneous temperature field at Ro = 0.15, $\Delta T = 30°c$ and Ra = 8.6e+08. Images are 10s apart. . . . . 88
4.5 Instantaneous temperature field at Ro = 0.08 $\Delta T = 10°c$ and Ra = 2.7e+08. Images are 10s apart. . . . . 89

5.1 Bubble oscillation sketch by Leonardo Da Vinci from his book The Codex Leicester . . . . . 92
5.2 Marginal Stability curve. Zhou et al., 2017 . . . . . 96
5.3 Experiment setup for 2D visualization of bubble (left) and Bubble image recorded simultaneously in two orthogonal planes.(right) 97
5.4 Experimental Setup . . . . . 97
5.5 Bubble rectilinear path in two orthogonal planes XZ (left) YZ(right) at Bo=5.5 and Ga = 60.4 in silicon oil 10cst . . . . . 98
5.6 Bubble planar zigzag trajectory in two orthogonal planes XZ (left) YZ(right) at Bo=6.1 and Ga = 64.6 in silicon oil 10cst. . . 99
5.7 Planar Zigzag path of bubble in side view of XZ,YZ plane (top) and top view of XY plane (bottom) . . . . . 100
5.8 Bubble helical path in two orthogonal planes XZ (left) YZ(right) at Bo=10 and Ga = 94 in silicon oil 10cst . . . . . 101
5.9 Helical path of bubble in side view of XZ,YZ plane (top),top view of XY plane (bottom left) and 3D view of path (bottom right) . . . . . 102
5.10 Marginal Stability curve of present work and Zhou et al., 2017 Open symbols : oscillating path and closed symbols : vertical path . . . . . 102
5.11 Non dimensional frequency of oscillation of the rising bubble in silicon oil of 10cst and 5cst. . . . . 104
5.12 Amplitude of oscillation of bubble in silicon oil of 10cst : parabolic fit indicates hopf bifurcation . . . . . 105

# List of Tables

3.1 Properties of Large scale circulation at various Rossby numbers in the rotation unaffected regime. . . . . 55

5.1 Threshold values of water, silicon oil of 5 cst and 10 cst observed experimentally. . . . . 103

5.2 Characteristics of bubble at the instability threshold. . . . . 103

# List of Abbreviations

| | |
|---|---|
| **LIF** | Laser Induced Fluorescence |
| **LSC** | Large Scale Circulation |
| **NOB** | Non Oberbeck Boussinesq |
| **PIV** | Particle Image Velocimetry |
| **RBC** | Rayleigh-Bénard Convection |
| **RRBC** | Rotating Rayleigh-Bénard Convection |

# List of Symbols

| | |
|---|---|
| $u$ | horizontal velocity |
| $v$ | vertical velocity |
| $P$ | pressure |
| $T$ | temperature |
| $T_o$ | reference temperature |
| $s$ | entropy |
| $g$ | gravitational acceleration |
| $R_o$ | rotation speed |
| $H$ | height of the cell |
| $D$ | diameter of the cell |
| $q$ | heat current density through conduction and convection |
| $V$ | bubble constant volume |
| $d$ | bubble equivalent diameter |
| $G_a$ | Galileo number |
| $B_o$ | Bond number |
| $w$ | transversal velocity |
| $\rho$ | density |
| $\mu$ | dynamic viscosity |
| $k$ | thermal conductivity of fluid |
| $\delta_{ij}$ | Kronecker delta |
| $\alpha$ | thermal expansion coefficient |
| $\zeta$ | bulk viscosity |
| $\nu$ | kinematic viscosity |
| $\kappa$ | thermal diffusivity |
| $\Omega$ | angular velocity |
| $\sigma$ | surface tension |
| $\sigma_{ij}$ | viscous stress tensor |
| $\Gamma$ | Aspect ratio |

# Chapter 1

# Introduction

## 1.1 Rayleigh Bénard Convection

Thermal convection takes place in a system where temperature gradient causes unstable density difference which results in fluid flow. The hot fluid expands and becomes lighter in density and rises above the surrounding fluid. Cold fluid which is denser, sinks down under the effect of gravity. The rising and sinking fluid organize themselves and form a large scale circulation. This physical process is ubiquitous in nature as well as in household and industrial appliances. This simple process produces complex fluid behavior under various circumstance. When the thermal convection occurs between a hot bottom plate and cold top plate, with vertical temperature gradient in the direction opposite to the gravity, it is called as Rayleigh Bénard Convection.

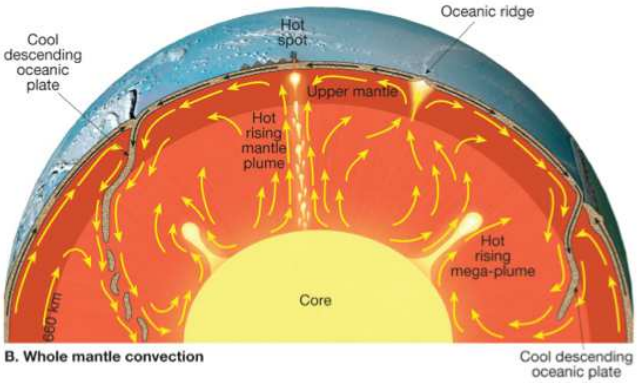


FIGURE 1.1: Whole mantle convection model ; Image source: Pearson Prentice Hall Inc, 2009.

It plays an important role in many geophysical and astrophysical flows Heimpel et al., 2007 Ingersoll, 1990, Marshall et al., 1999. Inside the earth's liquid outer core, convective motion of molten iron causes magnetic field under the

effect of earth's rotation. The convection inside earth's core also causes movement of tectonic plates. Convection inside the oceans produces mixing of water masses. In the outer convective zone of the sun, the convective motion between the radiative zone to the surface causes super-granular structures, which can be evidenced on the solar surface of the sun.

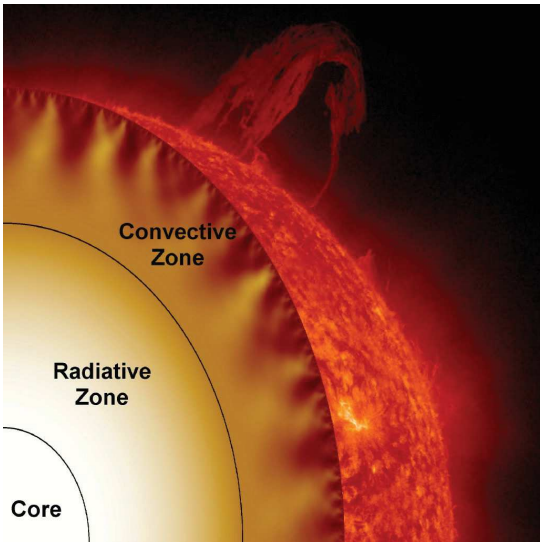


FIGURE 1.2: The Solar interior of the Sun. Image source: NASA.

Although, the examples mentioned above are affected by various parameters such as rotation of the earth, electro-magnetic field...etc, the convection between hot inner/bottom layer and cold outer/top layer is the underlying physical process. The applications of Rayleigh Bénard convection are not restricted to the natural phenomena. There are applications in industry such as, chemical process of crystallization, nuclear reactor core cooling system, heating/cooling of buildings, cooling system of electrical appliances...and many other. It can also be noticed in simple household applications such as water boiling inside a kettle. Hence it is important to comprehend this important physical process that governs various systems in everyday life.

Below the critical onset, the fluid transfers heat through conduction and the density is stratified with fluid at rest. The convection takes place when critical temperature difference is exceeded. Fluid motion forms regular patterns of convection cells during this process. These patterns which are called Bénard cells were initially reported in the experiments of Henri Bénard, 1900. This is considered as the first pioneering experimental study of Rayleigh Bénard convection. He studied the layer of fluid heated from below with a free

top layer. Ever since the discovery of patterns in thermal convection by Bénard, the research contributions to the Rayleigh Bénard convection are many, a few of them are mentioned here.

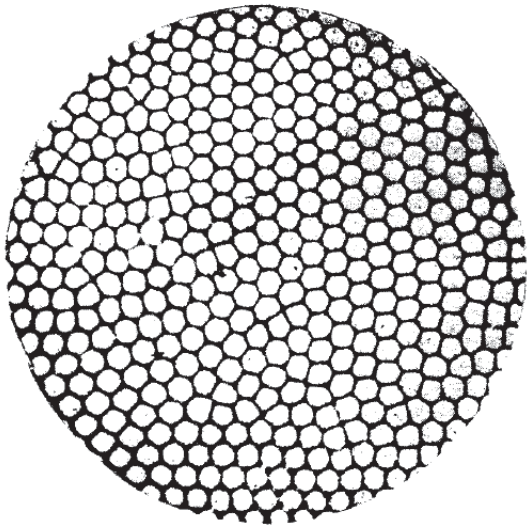

FIGURE 1.3: Bénard cells observed from top view, by Henri Bénard, 1900 in his convection experiment

Rayleigh, 1916 theoretically explained the underlying physics for convective onset in the idealised case of free (slip) boundaries. It has been extended to rigid (no-slip) boundaries by Jeffreys, 1926. Malkus, 1954 conducted numerical studies to predict the Nusselt scaling in turbulent convection at high Rayleigh number up to $10^{10}$. Chandrasekhar, 1961 studied the Rayleigh Bénard convection under the effect of rotation and magnetic field. Kraichnan, 1962 developed a theory to explain heat transport in turbulent convection as a function of Rayleigh and Prandtl number. Rossby, 1969 studied the increase in heat transfer in rotating Rayleigh Bénard convection. Busse in 1978 explored the non linear regime of Rayleigh Bénard convection with and without rotation, through analytical and numerical studies.

Many studies have been focused for the past decades on determining the Nusselt and Reynolds number variation with Prandtl and Rayleigh numbers. Castaing et al., 1989 studied the scaling of heat transport in Rayleigh Bénard convection in function of the Rayleigh number. Niemela et al., 2000 used cryogenic helium gas to study the convection at very high Rayleigh numbers. Chavanne et al., 2001 used thermocouples and helium gas at low temperature difference across the cell in a large range of Rayleigh numbers $(10^3 - 10^{12})$. Grossmann et al., 2000 developed the Nusselt scaling at different regimes depending on Rayleigh and Prandtl number. Weiss et al., 2011

studied the transition of single roll and double roll state of the large scale circulation at various aspect ratio using thermistors placed along the sidewalls in water. Shishkina et al., 2006, Stevens et al., 2013 conducted Direct Numerical Simulations (DNS) to study the heat transport and flow structure in Rayleigh Bénard convection at various aspect ratio, Rayleigh and Prandtl values . A review on the numerical and experimental studies on the predition of the scaling and the dynamics of the large scale circulation can be found in Ahlers et al., 2009.

While many experiments focused on scaling laws of the heat transport, some studies focused on the dynamics of plumes formation inside the Rayleigh Bénard cell under various circumstances. The temperature measurement along the side walls of Rayleigh Bénard cell can be achieved accurately using thermistors and thermocouples but, their measurements are local and intrusive and hence, they are not able to accurately measure the instantaneous temperature flow field inside the bulk. For studying the dynamics of plumes inside the bulk flow field experimentally, visualization techniques are necessary. The temperature difference in the rising hot plumes and sinking cold plumes causes changes in refractive index of light, and hence plumes can be visualized by shadowgraph experimental technique. Many researchers such as Jenkins, 1988, Zhong et al., 1991 used this technique to study the flow structure, velocity and orientation of flow field. Funfschilling et al., 2004 studied the oscillation of large scale circulation using shadowgraph technique. Xi et al., 2004 also used shadowgraph technique to study the onset of large scale circulation. Zhong et al., 1991 studied different regimes of flow in rotating Rayleigh Bénard using shadowgraph.

Geometric properties and density of thermal plumes were studied by Zhou et al., 2010 using thermochromic liquid crystal (TLC) technique at various Rayleigh. They concluded that density of plumes increases with increasing Rayleigh due to the increase in plume emission at high Rayleigh. Stasiek et al., 2002, Vorobieff et al also studied the plume evolution using thermochromic liquid crystals. The sensitivity of thermochromic liquid crystals is limited to small temperature range and hence can not be used to explore the flow dynamics at large temperature difference.

Thermal plumes can be observed by ombroscopy, but the information on the temperature flow field obtained by this technique remains qualitative. The temperature of plumes can be measured by small thermistors, but they provide only limited local information. While experiment techniques such as

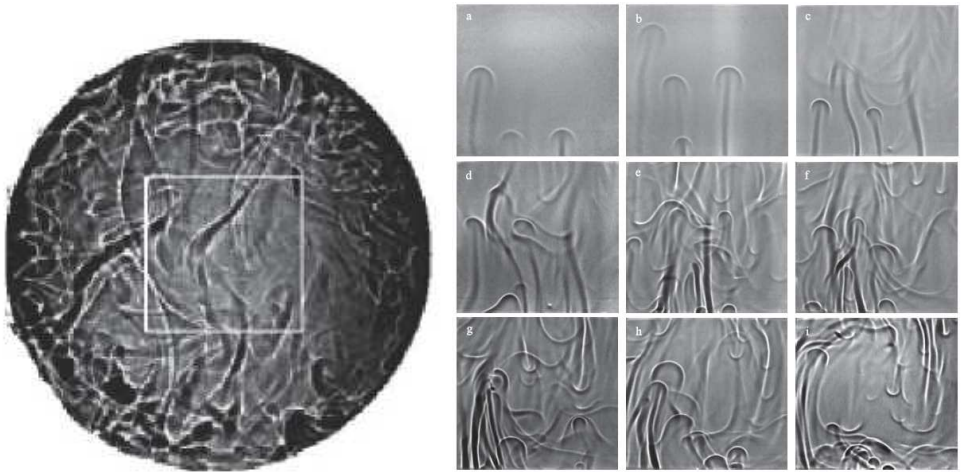

FIGURE 1.4: Shadowgraph technique. Plume visualized from the top view of RBC cell by Funfschilling et al., 2004 (left); Transient large scale flow from front view by Xi et al., 2004 (right).

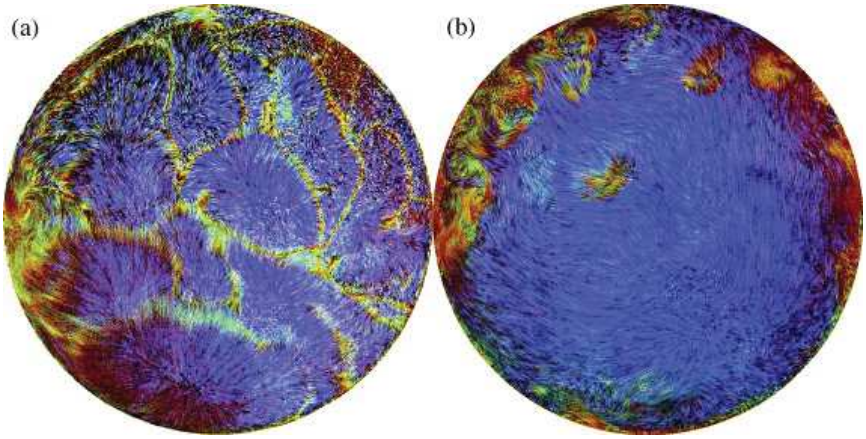


FIGURE 1.5: Thermochromic liquid crystal microsphere image of sheet plumes 2mm (a) and 2cm (b) from the top plate of RBC cell by Zhou et al., 2010

Particle Image Velocimetry (PIV) are developed for the visualization of velocity flow field, the experiment techniques for visualizing temperature flow field were relatively less developed. Sakakibara et al., 1999 introduced the two color laser induced fluorescence technique to calibrate the temperature flow field with a much higher accuracy and temperature range, than the thermochromic liquid crystals. This technique uses fluorescent light emmission to calibrate the temperature. The technique is described in detail in the chapter 2. Petracci et al., 2006 also used combined PIV and one tracer LIF experiment technique to study the temperature and velocity flow field simultaneously. In this thesis we use the two color Laser Induced Fluorescence (LIF) to calibrate temperature flow field in Rayleigh Bénard Convection with and without rotation. We also use PIV experiment to determine the velocity flow

field.

While knowledge on flow dynamics in Rayleigh Bénard convection has been increased in the past decades, it still poses various unsolved questions. Experimental robust visualization of flow field and calculation of temperature inside the flow field is yet to be resolved. Hence a reliable experiment setup to visualize the flow structure and define the velocity-temperature field simultaneously will assist the present understanding of Rayleigh Bénard convection.

## 1.2 Rotating Rayleigh Bénard Convection

When rotation is applied to convection, flow behavior changes drastically compared to non rotating convection due to the additional Coriolis force. As explained in the earlier chapter, rotating convection can be seen in many geophysical and astrophysical flows (Heimpel et al., 2007 Ingersoll, 1990 Marshall et al., 1999). Rotating Rayleigh Bénard convection is also present in industrial applications such as convection in turbo-machinery (Dunn, 2001 Johnston, 1998) and chemical vapor deposition process (Van Santen et al., 2000). Earlier studies on rotating Rayleigh Bénard convection were focused on the critical Rayleigh number defining the onset of convection. Rotation delays the onset of convection compared to the non rotating case. Chandrasekhar, 1961 by an analytical calculation, found the stabilizing effect of heat transfer measured at higher speeds of rotation. These early studies considered laterally infinite system in their observation of the flow patterns at the onset of convection. Using linear stability analysis, Chandrasekhar found a critical Rayleigh at the onset of convection as $Ra_c = 8.6956Ek^{4/3}$ ($Ra = g\alpha\Delta TH^3/(\nu\kappa)$ and $Ek = \nu/(2\Omega H^2)$ where $\alpha$ is the thermal expansion coefficient , $\nu$ is the kinematic viscosity, $\kappa$ is the thermal diffusivity and $\Omega$ is the angular velocity). Rossby, 1969 found that heat flux increases at moderate range of rotational speed. In a finite rotating system, boundary layers have more impact on the fluid flow compared to the non rotating systems. In rotating flows, Ekman pumping and Ekman suction occurs. Plumes emerging from boundary layer develop vorticity to conserve angular momentum.Vertical plumes loose their vorticity while reaching opposite vertical end and form columns at moderate rotational speeds. Enhancement in heat transfer observed by Rossby at moderate rotation rates can thus be an effect of Ekman vortices. The decrease in heat transfer observed by Chandrasekhar, 1961 is at higher rotation and corresponds to a transition from columns to fully turbulent state with no vertical coherence. Transitions at various rotational speed are usually defined using Rossby number(ratio of coriolis force to inertial force $Ro = U/(2\Omega H)$).

Visualisation of flow transitions near onset of convection has been studied by Zhong et al., 1991 ,Zhong et al., 1993 using shadowgraph technique and by Vorobieff et al., 1998, Vorobieff et al., 2002 using PIV technique. Julien et al., 1996a, Julien et al., 2012 studied numerically, the flow statistics at different regimes of rotating convection namely, cellular, convective taylor columns, plume and geostrophic turbulence. Zhong et al., 2010 and Weiss et al., 2010b

Weiss et al., 2016 measured experimentally, the Nusselt number at various Rossby. Multiple transitions were found based on Nusselt measurements by Wei et al., 2015. Another explanation of enhanced heat transfer is given as a consequence of the decrease of the thermal boundary layer thickness under rotation by Stevens et al., 2013. Kunnen et al., 2008 Kunnen et al., 2010 Rajaei et al., 2018 categorized the flow field at various rotation rate as rotation unaffected,rotation affected and rotation dominated geostrophic regime based on experimental characterization of flow field at various heights of RBC cell. It is interesting to note that these flow regimes based on Taylor columns are only noticed for Pr > 1. For Pr < 1, vortical columns are short and dissipate faster. Heat transfer enhancement is also absent in Pr < 1. For such rotating Rayleigh Bénard convection a different approach based on toroidal and poloidal energies is applied to classify the flow regimes Horn et al., 2015. Poloidal energy is the energy in the large scale flows like cells or rolls. Toroidal energy is the energy in vortical or swirling motions in the horizontal planes. The global flow is characterized by separating the energy contributions in large scale circulation and vertical vortices. Hence an unifying theory to explain the different transition regimes in rotating Rayleigh Bénard convection is still under development.

In this thesis the focus is on the flow field characterization of rotational Rayleigh Bénard convection in water, hence, in the Prandtl range 5.6 and 7. Vertical columns are well defined for Pr > 1 at moderate speeds unlike the case of Pr < 1 range. Hence in this work we define the flow regimes based on the transition from large scale circulation to the formation of vertical column.

## 1.3 Equations of Motion

Considering a Newtonian fluid of velocity **u** = (u, v, w) corresponding to directional vector (i, j, k), density $\rho$, pressure $P$, temperature $T$, entropy $s$ and gravitational accreleration $g$ the conservation of mass, momentum and energy equations can be written (Landau et al., 1959) as

$$\frac{\partial \rho}{\partial t} + \frac{\partial}{\partial x_i}(\rho u_i) = 0 \tag{1.1}$$

$$\rho \left[ \frac{\partial u_i}{\partial t} + u_j \frac{\partial u_i}{\partial x_j} \right] = -\frac{\partial P}{\partial x_i} + \frac{\partial \sigma_{ij}}{\partial x_j} - \rho g_k \tag{1.2}$$

$$\rho T \left[ \frac{\partial s}{\partial t} + u_i \frac{\partial s}{\partial x_i} \right] = \frac{\partial}{\partial x_i} \left( k \frac{\partial T}{\partial x_i} \right) + \sigma_{ij} \frac{\partial u_i}{\partial x_j} \tag{1.3}$$

where $\sigma_{ij}$ is the viscous stress tensor expressed as

$$\sigma_{ij} = \mu \left( \frac{\partial u_i}{\partial x_j} + \frac{\partial u_j}{\partial x_i} \right) - \frac{2}{3} \mu \frac{\partial u_k}{\partial x_k} \delta_{ij} + \zeta \frac{\partial u_k}{\partial x_k} \delta_{ij} \tag{1.4}$$

where the material properties are represented as $\mu$ dynamic viscosity, $\zeta$ bulk viscosity, $k$ thermal conductivity of fluid and $\delta_{ij}$ is Kronecker delta.

### 1.3.1 Oberbeck Boussinesq approximation

Boussinesq, 1903, Oberbeck, 1879 suggested that all fluid properties except the density of fluid, can be considered constant and independent of temperature. In this approximation, only the density depends on temperature. This is important for the gravitational term which drives the convection. Material properties such as thermal expansion coefficient $\alpha$, thermal conductivity $k$, viscosity $\nu$ are considered as independent of temperature. In the case of linear approximation, the variation of density with temperature can be written as

$$\rho(T) = \rho(T_o)[1 - \alpha(T - T_o)] \tag{1.5}$$

where $\alpha$ is thermal expansion coefficient of the fluid. $T_o$ is the reference temperature.

Considering this linear relation of density and constant fluid properties, the equations 1.1 ,1.2 and 1.3 can be represented in vector notation as

$$\nabla \cdot \mathbf{u} = 0 \tag{1.6}$$

$$\frac{\partial \mathbf{u}}{\partial t} + (\mathbf{u} \cdot \nabla)\mathbf{u} = -\frac{1}{\rho_o} \nabla P + \nu \nabla^2 \mathbf{u} + \alpha g T \hat{\mathbf{y}} \tag{1.7}$$

$$\frac{\partial \mathbf{T}}{\partial t} + (\mathbf{u} \cdot \nabla)\mathbf{T} = \kappa \nabla^2 \mathbf{T} \tag{1.8}$$

where $\kappa$ is thermal diffusivity, $\nu$ is kinematic viscosity and $\hat{\mathbf{y}}$ unit vector in vertical direction. Viscous dissipation of heat is negligible in the above equation 1.8.

Rayleigh Bénard convection is studied mostly under Oberbeck Boussinesq approximation and this approximation is valid for small temperature difference where $\alpha\Delta T < 0.2$. $\Delta T$ represents the maximum temperature variation in the system (Chavanne et al., 2001 Niemela et al., 2000). This is equal to the temperature difference between the hot bottom plate and cold top plate in Rayleigh Bénard convection.

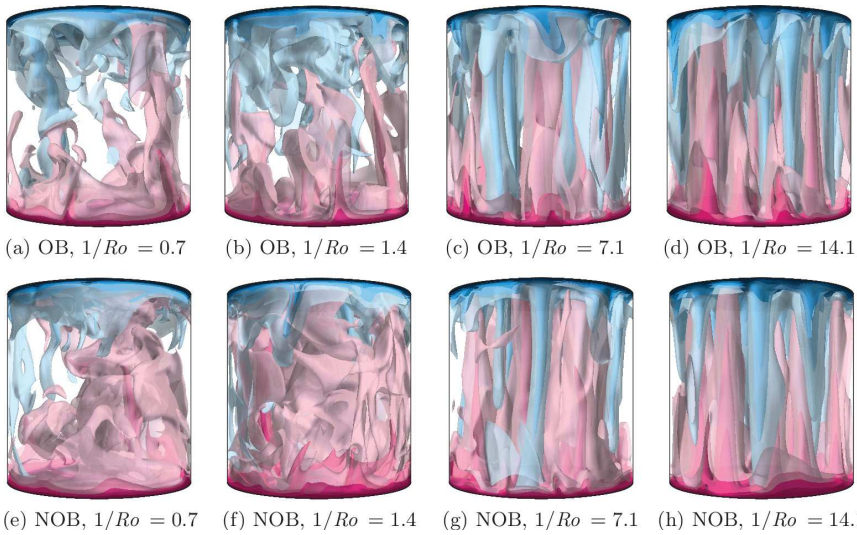

(a) OB, $1/Ro = 0.7$ (b) OB, $1/Ro = 1.4$ (c) OB, $1/Ro = 7.1$ (d) OB, $1/Ro = 14.1$

(e) NOB, $1/Ro = 0.7$ (f) NOB, $1/Ro = 1.4$ (g) NOB, $1/Ro = 7.1$ (h) NOB, $1/Ro = 14.1$

FIGURE 1.6: Instantaneous temperature fields at $Ra = 10^8$ and $\Delta T = 40C$ for NOB studies. Pink represents temperature above mean temperature and blue represents temperature below mean temperature. Horn et al., 2014

In a non Bousinesq condition all the above equations must include the variations of fluid properties. The extension of Prandtl Blasius theory to the non Oberbeck Boussinesq Rayleigh Bénard convection has been studied by Ahlers et al., 2006. In a Non Oberbeck Boussinesq (NOB) flow, the symmetry about mid plane is lost. The boundary layer thickness of the bottom and top plates is unequal. In the case of liquids, the viscous boundary layer close to the top plate (cold plate) is larger than the viscous boundary later close to the bottom plate (hot plate). The temperature in the "bulk" of the cell is not anymore the arithmetic mean of the top and bottom temperature but higher than this arithmetic mean (Horn et al., 2015). Hence thermal resistance on top and bottom is different.

### 1.3.2 Equations of Motion in rotating Rayleigh Bénard Convection

Under rotation,forces such as Coriolis and centripetal forces act on the system (Greenspan, 1968 Kundu et al., 2008). This creates additional acceleration compared to the non rotating inertial system. Considering the unit base vectors $(\hat{\mathbf{x}}, \hat{\mathbf{y}}, \hat{\mathbf{z}})$ rotating with an angular velocity $\hat{\Omega}$ with respect to vertical direction pointing against gravity (i.e. $\hat{\Omega} = \Omega\hat{\mathbf{y}}$) . The total acceleration equation can be written as

$$a_I = a_R + 2\Omega \times \mathbf{u_R} + \Omega \times (\Omega \times r) \tag{1.9}$$

Subscripts I and R represent inertial and rotation frame respectively. The terms $2\Omega \times \mathbf{u_R}$ and $\Omega \times (\Omega \times r)$ represents the acceleration contribution from the Coriolis force and centripetal force respectively.

Considering $r_\perp$ projection of r on perpendicular plane to $\Omega$ the centripetal acceleration can be further written as $\Omega \times (\Omega \times r) = -\frac{1}{2}\Omega^2 r_\perp^2$. This term is usually inserted in the pressure term to form reduced pressure $\nabla p = \nabla(\frac{\mathbf{P}}{\rho_o} - \frac{1}{2}\Omega^2 r_\perp^2)$.

With the above modifications the conservation of momentum in rotational frame can be rewritten as

$$\frac{\partial \mathbf{u}}{\partial t} + (\mathbf{u} \cdot \nabla)\mathbf{u} + 2\Omega \times \mathbf{u} = -\nabla p + \nu \nabla^2 \mathbf{u} + \alpha g T \hat{\mathbf{y}} \tag{1.10}$$

If we consider the flow inside RBC cell at moderate rotation speed $(Ro << 1)$, inside the bulk flow, away from the boundaries, the flow can be assumed to be quasi steady and independent of viscosity. Then, the momentum equation can be written as

$$2\Omega \times \mathbf{u} = -\nabla p + \alpha g T \tag{1.11}$$

Separating the respective directional components in the above equation, the momentum equations can be written as

$$2\Omega w = -\frac{\partial p}{\partial x}; \qquad 2\Omega u = -\frac{\partial p}{\partial z}; \qquad 0 = -\frac{\partial p}{\partial y} + \alpha g T \tag{1.12}$$

Considering the horizontal and transversal(z direction) momentum we can observe that the velocities in these planes are directed in the direction of isobars. Adding these equations and using the continuity equation one can obtain that $\partial v/\partial y = 0$ indicating the vertical velocity is constant and invariant in the vertical direction. Observing the vertical momentum equation, under Boussinesq approximation where density is taken into temperature terms, hydrostatic balance can be recognized.

Taking the vertical derivatives of the horizontal and transversal momentum equations and substituting the vertical pressure gradient, one can obtain

$$\frac{\partial \mathbf{u}}{\partial y} = \frac{g\alpha}{2\Omega} \times \nabla T \tag{1.13}$$

This equation indicates that the variation of horizontal velocity in the vertical direction, is a direct consequence of horizontal temperature variations. This is called Thermal Wind Balance.

### 1.3.3 Non Dimensional Parameters

To understand the effect of various forces affecting the flow field, it is important to define non dimensional numbers. Non dimensional numbers compare different forces acting on the system and they can be used to define the flow field variations at various conditions. Non dimensional numbers are obtained by introducing following dimensionless parameters into Navier Stokes equations

Position $\overline{x} = x/H$ ,velocity $\overline{\mathbf{u}} = \mathbf{u}/U$, time $\overline{t} = tU/H$, temperature $\overline{T} = T/\Delta T$, pressure $\overline{p} = p/U^2$

The substitution of above parameters in Boussinesq approximated conservation equations result in

$$\overline{\nabla} \cdot \overline{\mathbf{u}} = 0 \tag{1.14}$$

$$\frac{\partial \overline{\mathbf{u}}}{\partial t} + (\overline{\mathbf{u}} \cdot \overline{\nabla})\overline{\mathbf{u}} + \frac{2\Omega H}{U}\hat{\mathbf{y}} \times \mathbf{u} = -\overline{\nabla}\,\overline{p} + \frac{\nu}{UH}\overline{\nabla^2}\overline{\mathbf{u}} + \frac{\alpha g \Delta T H}{U^2}\overline{T}\hat{\mathbf{y}} \tag{1.15}$$

$$\frac{\partial \overline{\mathbf{T}}}{\partial \overline{t}} + (\overline{\mathbf{u}} \cdot \overline{\nabla})\overline{\mathbf{T}} = \frac{\kappa}{UH}\overline{\nabla}^2\overline{\mathbf{T}} \tag{1.16}$$

By approximating the buoyancy term $(\frac{\alpha g \Delta T H}{U^2})\overline{T}$ to be of O(1) we can define the free fall velocity as $U = \sqrt{g\alpha\Delta T H}$ (Prandtl, 1932). This is considered as the maximum limit of velocity generated by the buoyancy force.

The following non dimensional numbers can be defined from the eq 1.14 1.15 and 1.16

Rayleigh Number : Ratio of viscous dissipation and thermal dissipation.

$$Ra = \frac{g\alpha\Delta T H^3}{\nu\kappa} \tag{1.17}$$

Prandtl Number : Ratio of kinematic viscosity and thermal diffusivity.

$$Pr = \frac{\nu}{\kappa} \tag{1.18}$$

Rossby Number : Ratio of inertial force and Coriolis force.

$$Ro = \frac{U}{2\Omega H} \tag{1.19}$$

Ekman Number : Ratio of viscous force and Coriolis force.

$$Ek = \frac{\nu}{2\Omega H^2} \tag{1.20}$$

Nusselt Number : Ratio of total heat transfer (conduction + convection) and conductive heat transfer alone

$$Nu = \frac{qH}{k\Delta T} \tag{1.21}$$

where $q$ represents the heat current density through conduction and convection.

In a closed Rayleigh Bénard system, aspect ratio is defined as the ratio of diameter $D$ to the height $H$ of RBC cell.

$$\Gamma = \frac{D}{H} \tag{1.22}$$

In this work the aspect ratio of cell equals to 1 with $D = H = 10$cm. From above equations it can be deduced that

$$\frac{\nu}{UH} = \sqrt{\frac{Pr}{Ra}} \qquad and \qquad \frac{\kappa}{UH} = \frac{1}{\sqrt{PrRa}} \tag{1.23}$$

Substituting eq 1.20 in the non dimensional Boussinesq approximated mass, momentum and energy conservation equations under rotation eq 1.14,1.15 and 1.16, we obtain

$$\overline{\nabla} \cdot \overline{\mathbf{u}} = 0 \tag{1.24}$$

$$\frac{\partial \overline{\mathbf{u}}}{\partial t} + (\overline{\mathbf{u}} \cdot \overline{\nabla})\overline{\mathbf{u}} + \frac{1}{Ro}\hat{\mathbf{z}} \times \mathbf{u} = -\overline{\nabla}\, \overline{p} + \sqrt{\frac{Pr}{Ra}}\overline{\nabla^2}\overline{\mathbf{u}} + \overline{T}\hat{\mathbf{y}} \tag{1.25}$$

$$\frac{\partial \overline{\mathbf{T}}}{\partial \overline{t}} + (\overline{\mathbf{u}} \cdot \overline{\nabla})\overline{\mathbf{T}} = \frac{1}{\sqrt{PrRa}}\overline{\nabla}^2\overline{\mathbf{T}} \tag{1.26}$$

## 1.4 Boundary Layers

Eventhough the flow is turbulent in the bulk of Rayleigh Bénard convection, it has been proven that the flow inside the boundary layers near to the top and bottom plates of the RBC cells behaves laminar (Ahlers et al., 2009 Stevens et al., 2010a) until the ultimate regime. Ultimate regime occurs only in the range of Rayleigh number of $10^{11} - 10^{14}$. This range of Rayleigh numbers are only achieved in very large experiments or in special fluids such as liquid helium. Hence the boundary layers in RBC cell can be defined using Prandtl Blasius theory of laminar flow over flat plate (Schlichting, 1974). Prandtl Boundary layer theory is valid for Rayleigh Bénard convection as long as the shear Reynolds number inside the boundary layer is not too high.(approximately 420)(Landau et al., 1959). In rotating Rayleigh Bénard convection, the Prandtl Blasius boundary layer theory is also valid in the initial slow rotation range, where LSC is still the predominant flow structure. The Prandtl Blasius boundary layer transforms itself into Ekman boundary layer at the critical Rossby where flow changes from LSC to vertical columns at moderate speed of rotation.Rajaei et al., 2016

### 1.4.1 Prandtl Boundary Layer

The Prandtl Blasius boundary layer equation over a semi infinite horizontal plate for kinetic boundary layer is written as

$$u_i \frac{\partial u_i}{\partial x_i} + u_j \frac{\partial u_i}{\partial x_j} = \nu \frac{\partial}{\partial x_j}(\frac{\partial u_i}{\partial x_j}) \tag{1.27}$$

with boundary conditions of no slip at the wall $u_i(i,0) = 0, u_j(i,0) = 0$ and $u_i(i,\infty) = U$. Considering $u_i$ as the horizontal component of velocity and $u_j$ as vertical component of velocity, $U$ represents the bulk fluid velocity in Rayleigh Bénard convection. Solving the above equation with the boundary conditions results in the kinetic boundary layer thickness as below

$$\delta_u \approx \frac{1}{\sqrt{Re}} \tag{1.28}$$

where Re is the Reynolds number given by $Re = UH/\nu$.

Similarly the thermal boundary layer equation according to Prandtl Blasius theory can be written as

$$u_i \frac{\partial T}{\partial x_i} + u_j \frac{\partial T}{\partial x_j} = \kappa \frac{\partial}{\partial x_j}(\frac{\partial T}{\partial x_j}) \tag{1.29}$$

with boundary conditions $T(i,0) = T_{bottomplate}, T(i,\infty) = T_{bulk}$. Using Oberbeck Boussinesq approximation the bulk temperature can be considered as constant and equal to the mean temperature of top and bottom plates in RBC cell. The temperature gradient in the fluid is concentrated in the top and bottom boundary layers of thickness $\delta$ with temperature difference of $\Delta T/2$. In these boundary layers, the heat transfer is mainly diffusive and can be expressed as

$$q = \frac{l\,\Delta T/2}{\delta} \tag{1.30}$$

Therfore,

$$Nu = \frac{q}{l\Delta T/H} \approx \frac{L\,\Delta T}{2} \frac{1}{l\,\Delta T/H} \approx \frac{H}{2\delta} \tag{1.31}$$

The thermal boundary layer thickness can be written as

$$\delta_T \approx \frac{H}{2Nu} \tag{1.32}$$

Thermal and kinetic boundary layer thickness can also be calculated from the maximum root mean square values of temperature and horizontal velocity respectively. An alternative method of calculation of boundary layer thickness depends on the maximum energy dissipation.

### 1.4.2 Grossmann Lohse Theory

Grossmann Lohse theory Grossmann et al., 2000 Grossmann et al., 2004 describes various turbulent regimes in non rotating Rayleigh Bénard convection based on the dissipation rate of energy. Based on Prandtl Blasius laminar theory the kinetic and thermal dissipation rates can be defined as

$$\varepsilon_u = \frac{\nu^3}{H^4}(Nu-1)RaPr^{-2} \tag{1.33}$$

$$\varepsilon_T = \kappa(\frac{\Delta T}{H})^2 Nu \tag{1.34}$$

The volume averaged contributions of kinetic and thermal dissipation in the bulk and boundary layers are calculated individually and total dissipation is represented as the sum of individual bulk and boundary layer dissipation.

$$\varepsilon_u = \varepsilon_{u,BL} + \varepsilon_{u,bulk} \qquad \varepsilon_T = \varepsilon_{T,BL} + \varepsilon_{T,bulk} \tag{1.35}$$

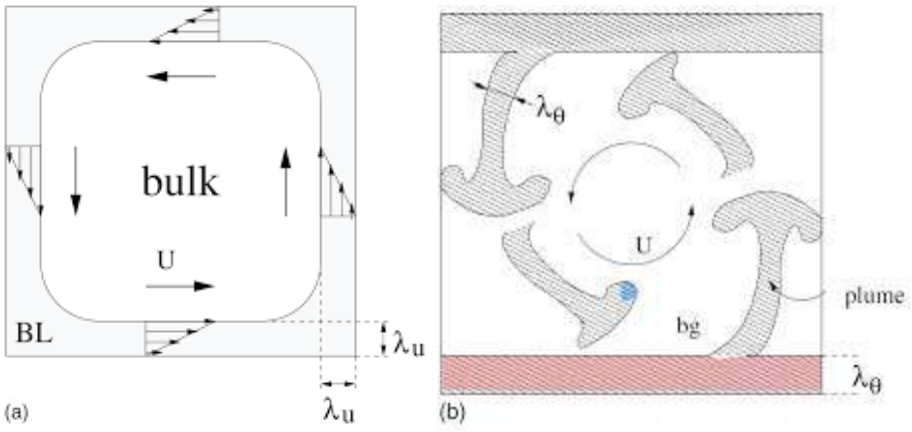


FIGURE 1.7: Boundary layer and bulk partition given by Grossmann et al., 2000. Kinetic boundary layer (left) Thermal boundary layer (right)

This separation now facilitates the description of flow regimes in non rotating convection into four regimes -

- The contribution of the kinetic and thermal dissipation in the boundary layers are the main contributions.
- The main contribution of the kinetic dissipation is located in the bulk while the main contribution of thermal dissipation is located in the boundary layer.
- The main contribution of the kinetic dissipation is located in the boundary layer while the main contribution of thermal dissipation is located in the bulk.
- The contribution of the kinetic and thermal dissipation in the bulk are the main contributions.

For low $Pr$ the viscous boundary layers thickness is thinner than the thermal boundary layers. Whereas, for high $Pr$ the thermal boundary layers thickness is thinner than the viscous boundary layers. Based on this, Grossmann Lohse theory defined $Nu$ and $Re$ power law scaling as a function of $Ra$ and $Pr$ at different regimes (Ahlers et al., 2009).

### 1.4.3 Ekman Boundary Layer

Equations of momentum under rotation for the fluid bulk are given in the equations 1.11 and 1.12. Unlike the bulk flow, the flow inside the boundary layers is largely affected by the viscosity. Hence the equations of momentum for the flow inside the boundary layers under rotation can be written (Ekman, 1905) as

$$-2\Omega w_e = -\frac{\partial p}{\partial x} + \nu \frac{\partial^2 u_e}{\partial y^2}; \qquad 2\Omega u_e = -\frac{\partial p}{\partial y} + \nu \frac{\partial^2 w_e}{\partial y^2}; \qquad 0 = -\frac{\partial p}{\partial y} + \nu \frac{\partial^2 v_e}{\partial y^2} \tag{1.36}$$

The pressure remains invariant in the vertical direction and hence is same in bulk and the boundary layers. Comparing the equations in the bulk and the boundary layers the following relation can be drawn.

$$-2\Omega w_e = 2\Omega w_b + \nu \frac{\partial^2 u_e}{\partial y^2}; \qquad 2\Omega u_e = 2\Omega u_b + \nu \frac{\partial^2 w_e}{\partial y^2}; \tag{1.37}$$

Velocity near the walls should be zero to maintain no slip condition. This velocity near to the wall should gradually increase and match the bulk velocity after crossing certain boundary layer thickness. Hence boundary conditions for the flow inside the boundary layer can be written as $\mathbf{u_e} = \mathbf{u_b}$ at $y \to \infty$ and $\mathbf{u_e} = 0$ at $y = 0$. Using these limits the equations in 1.37 can be solved to obtain

$$u_e = u_b - (u_b cos(y/\delta_e) + w_b sin(z/\delta_E))\, exp(-y/\delta_E) \tag{1.38}$$

$$w_e = w_b - (u_b cos(y/\delta_e) - w_b sin(z/\delta_E))\, exp(-y/\delta_E) \tag{1.39}$$

$$v_e = \frac{\omega_b \delta_E}{2} - \{1 - exp(-y/\delta_E)[sin(y/\delta_e) + cos(y/\delta_E]\} \tag{1.40}$$

where the suffixes $e$ and $b$ represent the values corresponding to boundary layer and bulk respectively. $\delta_E$ represents the Ekman boundary layer thickness near the top and bottom plates which is defined as $\delta_E = \sqrt{\nu/\Omega}$ and $\omega_b$ is the vorticity generated due to the Coriolis force. It is also interesting to note that $\delta_E$ scales as $Ek^{1/2}$ and thus the Ekman boundary layer thickness is unaffected by the bulk flow variations.

### 1.4.4 Ekman Suction and Ekman Pumping

Plume forming inside boundary layer develops vorticity within the boundary layer in order to conserve angular momentum created by the rotation (Grooms et al., 2010 Kunnen et al., 2011 ). The plume develops initially a cyclonic vorticity. As the plume with vorticity travels in the vertical direction, it looses the vorticity gradually and can also spin in opposite direction causing anti cyclonic vorticity while approaching the opposite plate. This flow from the boundary layers into the bulk is called Ekman pumping. In case of negative vorticity, the fluid flow is from the bulk into the boundary layers. This is called Ekman suction.

### 1.4.5 Stewartson Boundary Layer

The outward flux from the top and bottom boundary layers into the bulk needs to be conserved inside a closed RBC cell. The negative vorticity generated inside the bulk causes radially outward flow in the Ekman boundary layers at the top and bottom plates. This flow enters the side wall boundary

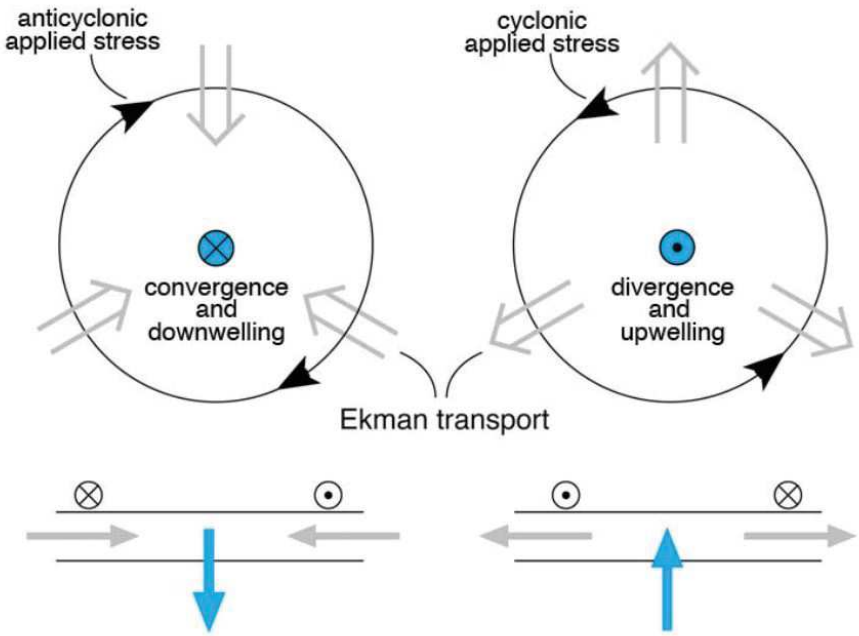


FIGURE 1.8: Ekman Transport Image source: David Beesley et al, Oceanography Vol 21 BEEsLEy et al., 2008.

layers. Also the sidewall boundary should posses no slip zero velocity at the wall and a velocity equals to bulk at certain radial thickness. Hence sidewall boundary layer features two sandwiched layers of $Ek^{1/3}$ and $Ek^{1/4}$ scaling (Kunnen et al., 2013). The sidewall boundary layer formed in RBC cell is called Stewartson Boundary Layer (Stewartson, 1957 Stewartson, 1966). These layers and different regions of boundary layers in rotating convection are well explained by Kunnen et al., 2013. It is also known that the sidewall boundary layers thickness decreases with an increase in speed of rotation (Kunnen et al., 2014) . Sidewall boundary layer may also affect the distribution of vortex columns inside RBC cell. Unlike the Grossmann Lohse theory in non rotating convection where the bulk and boundary layer contributions to the energy dissipation rates is quite well defined, a unifying theory for bulk and boundary layer contributions is yet to be made in the rotating convection. For the rotation unaffected regime of rotating convection where Prandtl Blasius theory is valid, a boundary layer theory for rotating convection based on Grossmann Lohse theory is presented by Stevens et al., 2010a
.

## 1.5 Flow Transition

Present study focuses on the flow transitions inside a RBC cell of aspect ratio 1 unless explicitly specified.

### 1.5.1 Non Rotating Rayleigh Bénard Convection

In a closed RBC cell the fluid which is heated at the bottom becomes lighter and moves upward. The hot fluid blob which comes out of the boundary layer pushes it's surrounding fluid and due to this, it becomes deflected like a cap. The rising fluid from the bottom forms a stalk like structure under the cap. Hence the fluid structure finally looks like a mushroom and is usually called a *plume*.(Kadanoff, 2001) The hot plumes rise and move upward along the side walls of the cell. The rising (falling) hot(cold) plume travels across the side wall and splashes into the top(bottom) cold (hot) layer. The rising and falling plumes drive a mean wind or *large scale circulation* (LSC). This mean wind sweeps the upcoming hot plumes from the bottom layer from one side to the other. Similarly cold plumes are swept by the large scale circulation in an opposite direction compared to the hot plumes. Some plumes may not get caught in the large scale circulation. Such plumes rise or fall, entering the central region which contains fewer hot and cold plumes. The thin boundary layers on the bottom and top plates contain the maximum temperature drop. The orientation of large scale circulation can be in any direction in a cylindrical cell, with meandering orientation and events such as reversal and cessation which are explained in the following.

#### Oscillations of LSC

Large scale circulation undergoes various interesting flow dynamics. The large scale circulation exhibits azimuthal oscillations in its circulation plane (Castaing et al., 1989, Niemela et al., 2001, Sreenivasan et al., 2002). These azimuthal oscillations are caused by the out of phase *torsional mode* oscillations of the upper half with the bottom half of LSC.This has been studied by Funfschilling et al., 2004 Funfschilling et al., 2008. The vertical symmetry plane of LSC is also found to oscillate periodically about the vertical axis of RBC cell. This in phase horizontal displacement of the LSC is called *sloshing mode* (Xi et al., 2009, Zhou et al., 2009) .

#### Reversals of LSC

Apart from the oscillatory behaviour of the LSC, it is also known to undergo azimuthal rotations (Brown et al., 2006) and *cessations* (Xi et al., 2007 Brown et al., 2005). This indicates that once in a while the LSC stops and re-orients itself in random direction independent of the previous dynamics. Cessations are caused by the momentary decoherence of the LSC. During a cessation the flow momentarily vanishes before it reorients itself. Both azimuthal LSC plane rotation and cessations cause *reversal* in the LSC direction. These reversals are explained as the imbalance between buoyancy and friction forces (Sreenivasan et al., 2002). It is also found that frequency of cessations increases with decrease in aspect ratio ($\gamma = D/H$) of the RBC cell (Xi et al., 2008a).

#### Single roll and Double roll LSC

Another interesting flow mode transition occuring in LSC is the break down of *single roll* LSC into vertically stacked *double roll* LSC which eventually comes back to single roll LSC (Xi et al., 2008b). It is also noticed that the frequency of double roll transition increases as the aspect ratio decreases. In a square or rectangular cell the LSC is found to prefer the diagonal orientation. Different flow modes in a square and rectangular cell have been studied by Zhou et al., 2007, Castillo-Castellanos et al., 2016.

It is now evident from the above studies that LSC variations are highly dependent on the aspect ratio of RBC cell. However in this study RBC cell of aspect ratio unity is only considered in all our experiments.

### 1.5.2 Rotating Rayleigh Bénard Convection

In rotating Rayleigh Bénard convection,the flow dynamics is completely different from the non rotating case (Boubnov et al., 1990 Kunnen et al., 2010) . Under slow rotation, LSC exists as the dominant flow structure. At moderate rotational speed, the plumes emerging from the boundary layers evolve into cyclonic and anticyclonic vortices to conserve the angular momentum induced by the rotation. These vertical columns are not formed immediately. Only after crossing the critical rotation rate, the columns begin to appear. This transitional rotation rate is defined using the non dimensional parameter Rossby (ratio of inertial force to the Coriolis force $Ro = U/2\Omega H$).

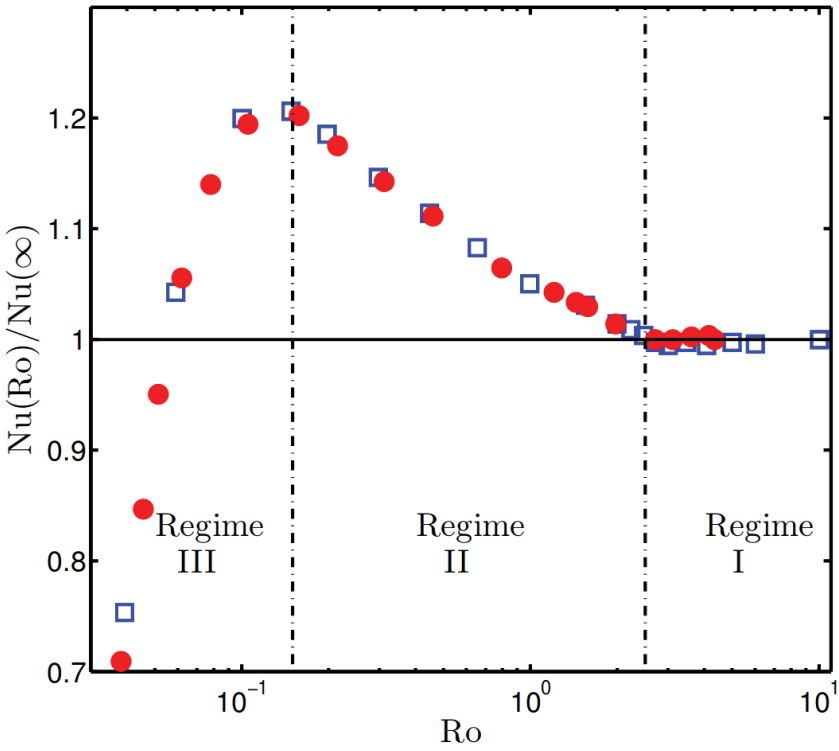


FIGURE 1.9: Normalized heat transfer as a function of Rossby number on logarithmic scale. (Taken from references Rajaei et al., 2016 Stevens et al., 2009 Zhong et al., 2010)

**Rotation unaffected regime (Ro > 2.5 ; Regime I)**

The flow field is a little affected by the Coriolis force at slow rotation but the buoyancy forces are strong enough to sustain the large scale flow. (Kunnen et al., 2008 Weiss et al., 2011)

Relative Nusselt is almost constant. Weiss et al., 2010b Weiss et al., 2016, expressed the sub transitions present in Nusselt measurement. Initially Nusselt increases by 10% and then decreases a little before the actual increase in the rotation affected regime. The dynamics of flow during these sub transitions are not completely understood. The velocity visualizations might help in understanding these transitions. It is known that cessation frequency increases in large scale circulation under rotation Zhong et al., 2010. It is also known that LSC undergoes precession. The loss of symmetry about the horizontal mid plane may explain the initial increase and decrease of Nusselt observed in this regime.

**Rotation affected regime (0.1 < Ro < 2.5 ; Regime II)**

The Coriolis forces dominate the buoyancy force. The plumes formed in boundary layer, develop cyclonic vorticity (in the direction of rotation of system). The Ekman pumping developed in the boundary layer restricts the plumes from separating from the boundary layer. Hence the large scale circulation ceases to exist (Kunnen et al., 2008, Stevens et al., 2013). The vertical columns extend into the bulk and gradually reach the opposite end in the vertical direction to conserve the angular momentum (Stevens et al., 2009). As the plumes extend from one end to the other, they loose their vorticity and may cause the vorticity to change sign in the mid vertical direction(Grooms et al., 2010, Portegies et al., 2008 Veronis, 1959 , Pedlosky et al., 1988).

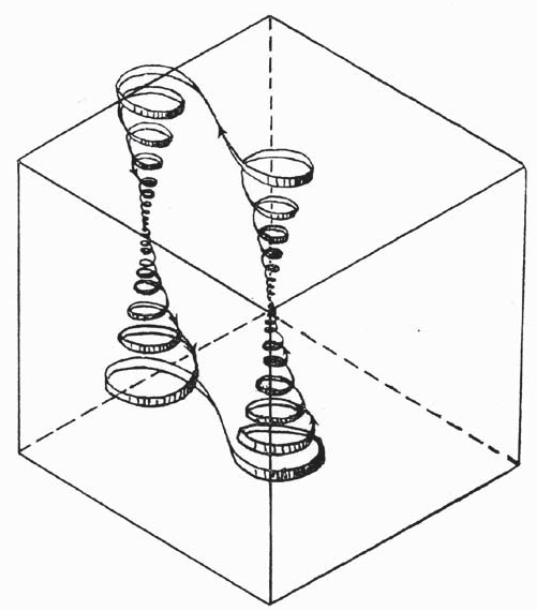

FIGURE 1.10: A perspective sketch of path of a fluid particle in square cell under rotation by Veronis, 1959

This needs to be further verified by studying velocity variations at different vertical height in the cell. In this regime, Nusselt numbers increase due to enhanced transport of fluid from the boundary layers into the bulk by the vertical columns. Although vortices begin to develop soon after the critical Rossby number in the boundary layer near the top and bottom plates, it is only for higher rotation rates that the Taylor columns completely reach other end. At the position of maximum heat transfer it can be assumed that the columns have extended in the complete vertical extent.

### Rotation Dominated Regime (Ro < 0.1 ; Regime III)

The vertical motion of the columns is suppressed by the Taylor Proudman effect. Hence the heat transfer enhancement decreases.(Nieves et al., 2014 Stevens et al., 2009 Stellmach et al., 2014) It reaches eventually, a regime where pressure gradient balances the coriolis force. This regime can be explained as the geostrophic turbulence. Further increase in the rotation causes pure conduction state where relative Nusselt number is less than 1. Geostrophic regime consists of all the above mentioned flow structures i.e cellular onset of convection,taylor columns,plumes and the geostrophic turbulence (Rajaei et al., 2017).

### Determination of Critical Rossby

Although the transition between the regime LSC and rotation affected regime have been studied numerically by Julien et al., 2012 Julien et al., 1996a, Julien et al., 1996b, Alards et al., 2018, Stevens et al., 2013 and experimentally by Weiss et al., 2016, Weiss et al., 2010b, Kunnen et al., 2008, Kunnen et al., 2010,Zhong et al., 2010, Rajaei et al., 2016, Rajaei et al., 2018, the dynamics of flow near the transition is still not completely understood. The works of Weiss et al., 2010b, Wei et al., 2015, Weiss et al., 2016 suggest multiple intermediate transitions based on Nusselt measurements.

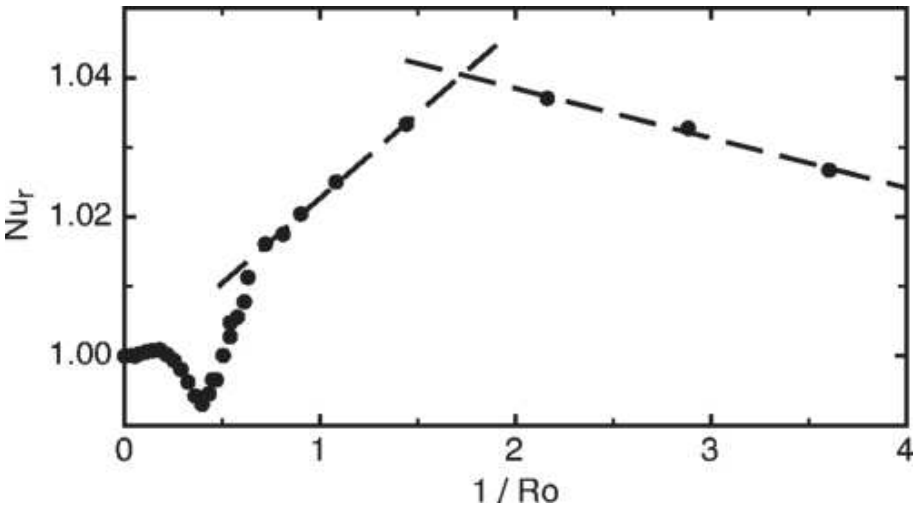


FIGURE 1.11: Relative Nusselt variation with inverse Rossby observed by Wei et al., 2015 at Pr = 4.38 and Ra= 1.8 x $10^{10}$

These transitions are yet to be explained. The works of Weiss et al at $Pr = 4.38$ and Stevens et al., 2009 at $Pr = 6.2$ suggest the critical $Ro \approx 2.5$ for aspect ratio unity. The initial works of Kunnen et al., 2008 Kunnen et al., 2010 at $Pr = 6.4$ suggest that LSC still exists until $Ro < 1.2$. The Critical Rossby

is known to be independent of Ra and mildly dependent on Pr (Zhong et al., 2010). Critical Rossby also varies for varing aspect ratio. (Stevens et al., 2010b1.12 Weiss et al., 2015)

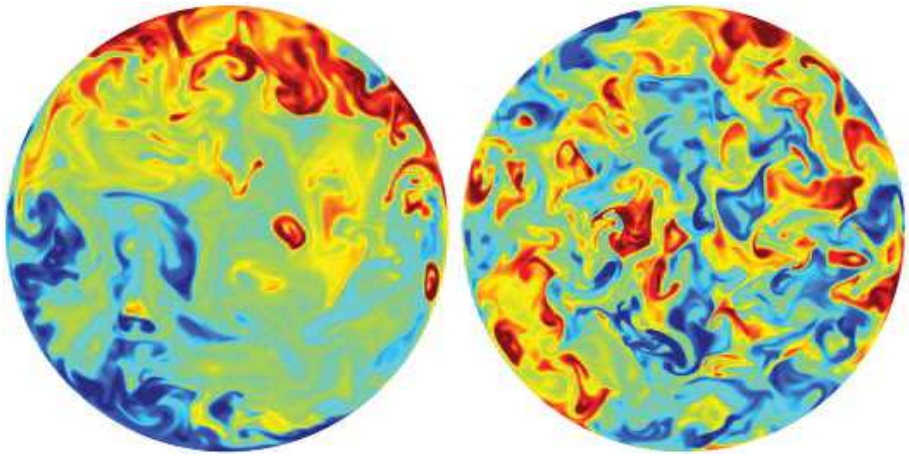

FIGURE 1.12: Temperature field in horizontal mid plane of RBC cell of $\gamma$ = 2, by Stevens et al., 2010b at Pr = 4.38 and Ra= 2.91 x $10^8$ left $1/Ro = 0.046$ and right $1/Ro = 0.6$

Although the transitions are expected to be a single sudden change or multiple sudden changes occuring continuously, due to the finite size effect in Ginzburg Landau effect (Weiss et al., 2010a), the transition affects heat transfer statistics and velocity statistics differently at different rotation rates. A unified theory to define the flow near transition point is yet to be developed. Visualization of temperature flow field in rotating RBC has been achieved numerically by Stevens et al., 2010b (see figure 1.12) and Horn et al., 2014 (see figure 1.6). However, experimentally the temperature flow field has not been visualized completely in rotating RBC.

In this thesis we conduct experiments in all three regimes, to visualize flow in the full vertical extent of the mid vertical plane. We compare the flow statistics at various vertical heights to understand the flow field that can cause various transitions. The study of velocity at various vertical locations can explain the difference in the critical Rossby calculations and also in the multiple transitions observed. We use Laser Induced Fluorescence technique to visualize temperature flow field in rotating RBC.

# Chapter 2

# Experimental Methods

## 2.1 Introduction

In a convection system, momentum and energy transfer occurs. These transfer mechanisms can be made visible with the help of flow visualization techniques. In this chapter, the experiment techniques used to visualize and characterize flow inside Rayleigh Bénard cell are presented. Two experiment techniques such as Laser Induced fluorescence (LIF) and Particle Image Velocimetry (PIV) are used in this thesis. First, the LIF measurement technique is explained in detail. The tracers properties are presented. Experimental setup and convection cell used in this thesis are presented. Lastly, a brief explanation of PIV experiment procedure is given.

## 2.2 Planar Laser Induced Fluorescence

Soluble dyes have been mixed in liquid to visualize the flow since the 18th century. However this technique only produced qualitative results (Reynolds, 1883). The intent is to obtain quantitative results from visualization techniques. Fluid temperature and changes in the concentration, can be determined globally using Laser Induced Fluorescence (LIF) technique, unlike the local measurements of the thermocouples. The most widely used LIF technique is the two dimensional Planar Laser Induced Fluorescence (PLIF) Crimaldi, 2008. LIF technique is based on laser excitation of fluorescent dye. Upon the excitation of laser, the dye emits fluorescence. The emitted fluorescence is optically measured to determine concentration or temperature.

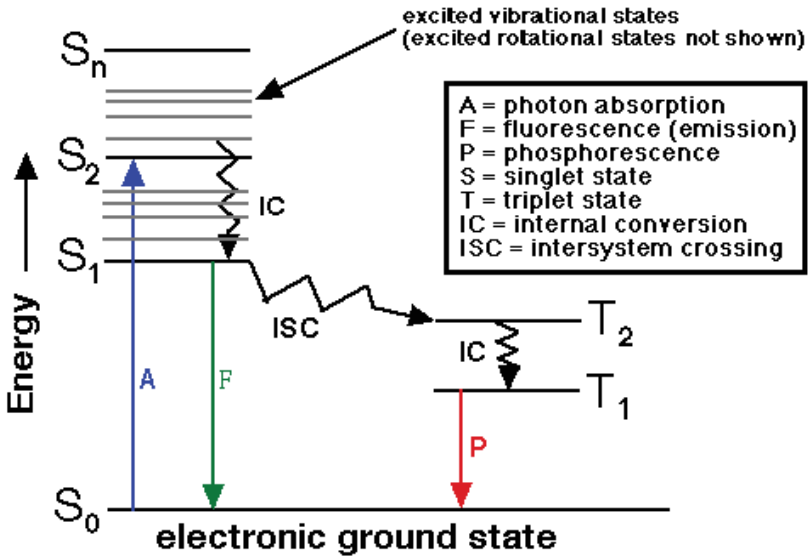


FIGURE 2.1: Jablonski Diagram.

### 2.2.1 Principle of Fluorescence

Initially the molecule is in stable state. Upon the excitation by a laser, the molecule absorbs the radiative energy and reaches an excited unstable state. It is important to choose the laser wavelength according to the absorption spectrum of the corresponding dye. The dye molecules cannot stay for long duration in the unstable excited state and return to the stable energy level while releasing fluorescence. This released fluorescence can be captured by using an optical setup with camera, optical filters and lenses. The optical filters (usually a band pass filter) should have a wavelength band which includes atleast part of the emission spectrum of the dye.

Jablonski, 1933 proposed energy level diagram as shown in fig 2.1 to explain various luminescence phenomena. Each energy level consists of sub rotational and vibrational energy levels. In the figure 2.1 there are two types of excited levels or states. In a singlet excited state $(S_1)$ the electron spin remains the same as in the ground state $(S_0)$. In a triplet state $(T)$ the electron spin matches with the other unpaired electron in the triplet state. Various phenomena that can occur in the electronic energy level spectrum can be defined as below.

- Molecules are excited from the ground singlet state by the incident light energy. They absorb and reach a higher energy singlet state from the ground singlet state. This is called *absorption*.

- Molecules relax to intermediate vibrational states of the excited energy singlet state. This phenomena of internal conversion is called *vibrational relaxation*. This is a non radiative transition.
- Molecules finally reach their ground energy singlet state by releasing photons. This process of de-excitation from excited singlet state to the ground singlet state is called as *fluorescence*.
- Sometimes molecules reach the ground state due to molecular collisions or internal heat transfer. This process is called non radiative *quenching*.
- Occasionally molecules do not directly reach the ground singlet state from the excited singlet state. They relax to inter system meta-stable triplet state. From the triplet state they reach to the ground singlet state due to molecular collisions. The energy released during this phenomena is called *phosphorescence*.
- Molecule may also return from the triplet state to the first excited singlet state. From the excited singlet state the molecule reaches again the ground singlet state. This process is called *delayed fluorescence* .

### 2.2.2 Measurement Principle

The ratio of total energy emitted per quantum energy absorbed is called the quantum efficiency. Now considering only the energy utilized in the fluorescence, one can define the quantum efficiency of fluorescence as, the ratio of fluorescence transmission from higher energy state 2 to lower energy state 1, to the total de-excitation transmission. The total de-excitation transmission includes the de-excitation by the fluorescence and quenching due to internal collisions (coll), internal energy conversions (IC) and the inter system crossing (ISC) to the triplet state.

$$\eta = \frac{A_{21}}{A_{21} + Q_{coll} + Q_{triplet} + Q_{IC}} \tag{2.1}$$

$A_{21}$ is the Einstein coefficient of spontaneous emission.

If quenching due to internal conversion of energy and inter system transfer to triplet state are neglected, the quantum efficiency of fluorescence is written as

$$\eta = \frac{A_{21}}{A_{21} + Q_{coll}} \tag{2.2}$$

If we consider a volume $V_c$ of fluid seeded with fluorescent tracer of concentration 'C' and subjected to incident laser excitation $I_o$, according to Beer Lambert law, a part of the incident laser intensity is lost due to absorption by the medium while traveling length L. Hence, if the laser light travels a distance L before reaching the measurement volume $V_c$, the intensity which reaches the volume can be written as

$$I_{V_c}(L,0) = I_0 \; e^{-\int_0^L C(x)\varepsilon\left(\lambda_{laser}\right)dx} \tag{2.3}$$

Where $\varepsilon$ indicates coefficient of absoption. High value of coefficient of absorption indicates that the laser intensity is lost quickly as it travels through the medium. If the laser dye is uniformly distributed (homogeneous seeding) in the measurement volume then the laser intensity reaching the measurement volume is written as

$$I_{V_c}(L,0) = I_0 \; e^{-CL\varepsilon\left(\lambda_{laser}\right)} \tag{2.4}$$

In a linear domain, fluorescent intensity is proportional to the excited laser intensity. Assuming negligible fluorescence re-absorption in the optical path, for a wavelength '$\lambda$', the fluorescent intensity is expressed as

$$I_f = K_{opt}(\lambda) I_0 \, \eta \, C \, V_c \, \varepsilon(\lambda) \, e^{-CL\varepsilon\left(\lambda_{laser}\right)} \tag{2.5}$$

where, $K_{opt}$ is the optical constant.

Generally, re-absorption occurs as the absorption and emission spectrum overlap. In such cases, if '$e$' is the distance between the measurement volume and the optical collector, the fluorescence intensity reaching the measurement volume is re-written as

$$I_f = K_{opt}(\lambda) I_0 \, \eta \, C \, V_c \, \varepsilon(\lambda) \, e^{-CL\varepsilon\left(\lambda_{laser}\right)} e^{-Ce\varepsilon\left(\lambda\right)} \tag{2.6}$$

By maintaining shorter optical path and lower concentrations of the dye, the absorption in the optical path can be neglected. In such a case, the fluorescence intensity depends only on the incident laser intensity $I_o$, optical constant $K_{opt}$, measurement volume and properties of the dye (concentration of the dye, absorption coefficient, quantum yield). Hence the fluorescence intensity equation is simplified to

$$I_f = K_{opt}(\lambda) I_0 \, \eta \, C \, V_c \, \varepsilon(\lambda_{laser}) \tag{2.7}$$

### 2.2.3 Temperature Calibration

Temperature sensitive fluorescent dyes such as Rhodamine B, Rhodamine 110, Fluoroscein , KitonRed can be used to measure temperature from the fluorescent intensity. Fluorescence is used to measure temperature since the $20^{th}$ century (Bruchhausen et al., 2005 Lemoine et al., 1999 Nakajima et al., 1991 Sakakibara et al., 1999). In order to measure temperature from the output fluorescent intensity, the concentration, measurement volume and the incident intensity are maintained constant. The only parameters that depend on temperature are the quantum efficiency and the absorption coefficient. The de-excitation rate due to collisions is directly proportional to the solvent concentration $C_s$ and can be expressed as

$$Q_{coll} = K_q C_s \tag{2.8}$$

$K_q$ is the de-excitation constant which is expressed from the Glovacki law as

$$K_q = K_{q_0}\, e^{\left(-\frac{Ea}{kT}\right)} \tag{2.9}$$

Where 'Ea' is the activation energy required for collision. $K_{q_o}$ is a constant depending on tracer and solvent properties. If the de-activations due to collisions are higher than the radiative de-activation, the quantum efficiency in eq 2.2 can be simplified using eq 2.8 and eq 2.9 as

$$\eta \approx \frac{A_{21}}{Q_{coll}} = \frac{A_{21}}{C_s K_{q_0}} e^{\left(\frac{Ea}{kT}\right)} \tag{2.10}$$

Substituting above equation in the eq 2.7 we obtain the fluorescent intensity as

$$I_f = K_{opt}(\lambda) I_0\ C\, V_c\, \varepsilon(\lambda_{laser}) \frac{A_{21}}{C_s K_{q_0}} e^{\left(\frac{Ea}{kT}\right)} \tag{2.11}$$

To consider the temperature dependence of the absorption coefficient $\varepsilon$, we are assuming that the absorption coefficient is proportional to the fraction of molecules involved in vibrational losses of excited sub energy levels. From the Boltzmann law , the fraction of molecules is expressed as

$$g = f_{B,0}\ e^{\left(\frac{\Delta E}{kT}\right)} \tag{2.12}$$

g is Boltzmann fraction, ΔE is energy difference between the states 1 and 2 and 'T' is the temperature. Replacing '$\varepsilon$' in eq 2.11 with the above expression results in

$$I_f \propto K_{opt}(\lambda) I_0\ C\, V_c\, f_{B,0} \frac{A_{21}}{C_s K_{q_0}} e^{\left(\frac{Ea-\Delta E}{kT}\right)} \tag{2.13}$$

Merging the effects of fluorescent spectrum into a single constant $K_{spec}$, the fluorescent intensity is further simplified as

$$I_f = K_{opt}\, K_{spec}(\lambda, \lambda_{laser}) I_0\ C\, V_c\, e^{\left(\frac{\beta(\lambda)}{T}\right)} \tag{2.14}$$

where $\beta = \frac{Ea-\Delta E}{k}$ *and* $K_{spec} = f_{B,0}\, \frac{A_{21}}{C_s K_{q_0}}$. Integrating the above equation for the entire spectral band 'i' of fluorescent intensity $I_f$, we obtain

$$\int_{\lambda 1}^{\lambda 2} I_f = K_{opt}\, K_{spec} I_0\ C\, V_c\, e^{\left(\frac{A_i}{T^2} + \frac{B_i}{T}\right)} \tag{2.15}$$

$A_i$ and $B_i$ are temperature sensitivity coefficients for the band 'i'. If the temperature difference is not too high, the second order term can be neglected (Maqua et al., 2008. Generally the light intensity may vary due to various parameters such as refraction of light caused by the variation of density, laser illumination in the plane of observation. In order to remove these effects of optical and spectral non-homogeneity, ratio of fluorescence is considered. The ratio of the fluorescent dye intensity is independent of the incident light intensity. Two major techniques are used to obtain intensity ratio namely, 1 dye 2-bands method and 2 dye 2 bands method.

**1 Dye 2 Bands Fluorescence technique**

This technique uses a single dye. Two spectral bands of the same dye are selected to detect the fluorescent intensity. The ratio of the fluorescent intensity collected at these two bands, eliminates the effects of non uniformity of concentration and incident laser intensity. Bruchhausen et al., 2005 used this technique to obtain $0.8\%/^oC$ sensitivity. This method is efficient to eliminate the effects of illumination defects and spurious reflection due to the local temperature changes including the difference in density and index of refraction. But, the signal to noise ratio is deteriorated. This is primarily caused by the lack of equal fluorescent intensity from the two spectral bands. Hence, the weaker band reduces the effective signal.

**2 Dyes 2 Bands Fluorescence technique**

This technique uses two fluorescent dyes dissolved in the solvent. Two bands specific to each dye are chosen. Rhodamine B and Rhodamine 110 were used by Sakakibara et al., 1999 to measure the temperature field in Rayleigh Bénard convection with sensitivity of $1.7\%/^oC$. To achieve higher sensitivity to temperature, the two dyes must have opposite dependence on temperature. This method ensures optimum sensitivity of fluorescent intensity on the temperature. This method is employed in the present work to measure instantaneous temperature field in Rayleigh Bénard Convection.

Due to the concentration or density variations in solution, the laser light can be defracted. These errors caused by spectral and optical non homogeneity

are removed by dividing each tracer fluorescent intensity with a reference fluorescence intensity '$I_{f_o}$'measured at a known uniform temperature '$T_o$'. From eq.2.14 the ratio of fluorescent intensity for tracer 1 is written as

$$\frac{I_{f_1}}{I_{Ref_1}} = \frac{I_0}{I_{0_{Ref}}} e^{\beta_1(\lambda_1)(\frac{1}{T}-\frac{1}{T_o})} \tag{2.16}$$

Similarly for the tracer 2 the resultant fluorescent ratio can be written as

$$\frac{I_{f_2}}{I_{Ref_2}} = \frac{I_0}{I_{0_{Ref}}} e^{\beta_2(\lambda_2)(\frac{1}{T}-\frac{1}{T_o})} \tag{2.17}$$

Dividing the eq 2.16 and 2.17 results in

$$\frac{I_{f_1}}{I_{f_2}} = \frac{I_{Ref_1}}{I_{Ref_2}} e^{(\beta_1(\lambda_1)-\beta_2(\lambda_2))(\frac{1}{T}-\frac{1}{T_o})} \tag{2.18}$$

From the above equation it is possible to calculate instantaneous temperature in the flow field from the captured fluorescent intensity ratio of tracers.

### 2.2.4 Fluorescent dye properties

To employ 2 dyes 2 bands technique, both fluorescent dyes must be absorbed in the same region, so that one laser can be used for both dyes but, they must have different emission spectra. In choosing the fluorescent dyes, we must verify that there is no loss of fluorescence due to continuous exposure to the laser light (photo bleaching). This causes losses in the fluorescence ratio. Separated emission spectrum facilitates collection of excited light separately for both dyes. In the optimal choice of the dyes, one dye must be highly sensitive to temperature whereas the other dye is non sensitive or less sensitive to the temperature, or, both dyes must have opposite behavior (i.e. if one increases, the other decreases the fluorescence with the temperature). Such an optimal choice of dyes, ensures a maximum sensitivity of the intensity ratio with the temperature. Selected dyes should not be sensitive to pH. We did preliminary experiment with fluoroscein. The sensitivity of dye is very high with the temperature but we had problems in reproducing the same result due to the high pH sensitivity of the fluoroscein. The $CO_2$ in the air slowly dissolved in the distilled water used in dye solution and turned the pH to

acidic. This could not be completely prevented by the use of a buffer solution.

Various errors that can occur in the ratio-metric temperature measurement using LIF are discussed in detail by Coppeta et al., 1998. One of the main reasons for errors to occur is caused by the overlap of emission and absorption spectra of the both dyes. The error caused by fluorescent emission spectrum overlap, between the two dyes, is reduced by proper selection of the band pass filters. The error caused by the overlap of emission spectra of dye 1 and absorption spectra of dye 2 is removed by using lower concentrations of dye and shorter optical path.

The following points are taken into consideration while selecting dye.

- One dye should be passive or less sensitive to the temperature and the other dye should be highly sensitive to temperature.
- Dyes must be completely soluble in the solvent.
- Dyes should not have overlap of fluorescent spectrum.
- Dyes should not be sensitive to pH. Buffer solutions must be used to stabilize pH if required.
- Dyes should be stable in time. Photo bleaching must be avoided.
- Concentration of dyes should be maintained low and it should not vary with temperature.
- Dyes should have high quantum yield.
- Dyes should have a fluorescence spectrum which is not predominant in the laser excitation wavelength to avoid fluorescence distortion in the optical path.

### 2.2.5 Fluorescence Spectrum

Different solution of dyes such as Fluoroscein disodium and Sulphorodamine solution, Rhodamine560 and Kiton Red solution are tested at different concentrations in the present study. Upon examination, we found from our experiments that the combination of Rhodamine 560 and Kiton Red with concentration of $10^{-5} mol/l$ and $10^{-6} mol/l$ respectively, has higher sensitivity

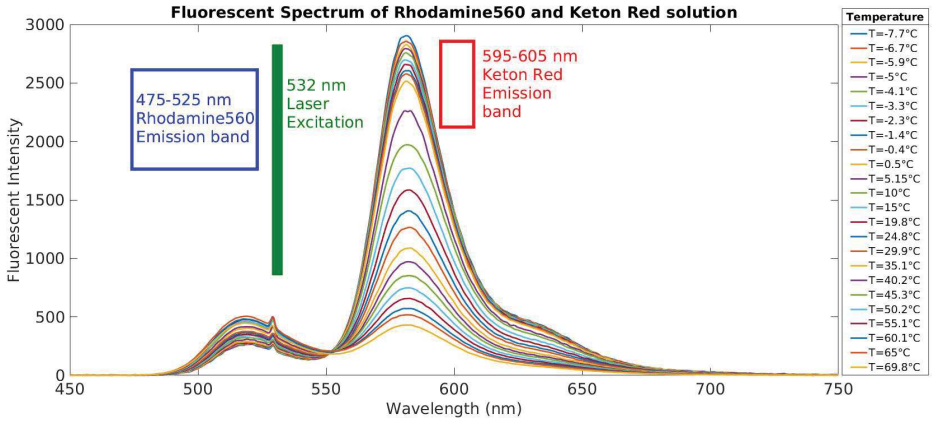


FIGURE 2.2: FLuorescent Spectrum of Rhodamine560 and Kiton Red.

to temperature. The two spectral bands chosen are 475-525 nm for Rhodamine560 and 595-605 nm for Kiton Red. The fluorescent emission spectra of Rhodamine 560 and Kiton Red solution are shown figure 2.2. The field is excited with laser at 532 nm. From the fluorescent spectra, it is evident that Rhodamine560 is less sensitive to temperature, whereas the fluorescent dye Kiton Red is highly sensitive to temperature. The emission spectral bands are widely seperated as shown in figure 2.3. Hence, there is no possibility of overlap in the captured fluorescent intensity for the two tracers by the filters.

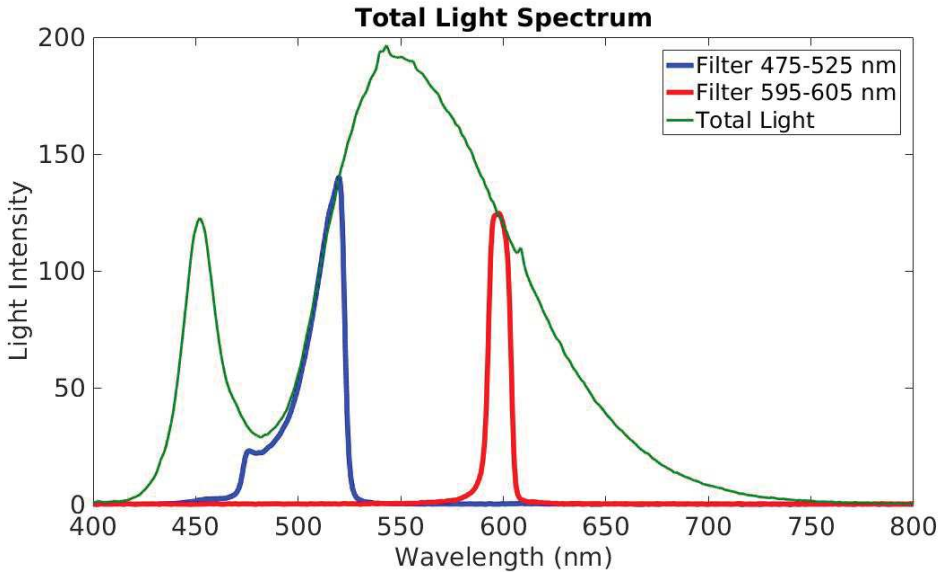


FIGURE 2.3: Fluorescent Emission Spectrum.

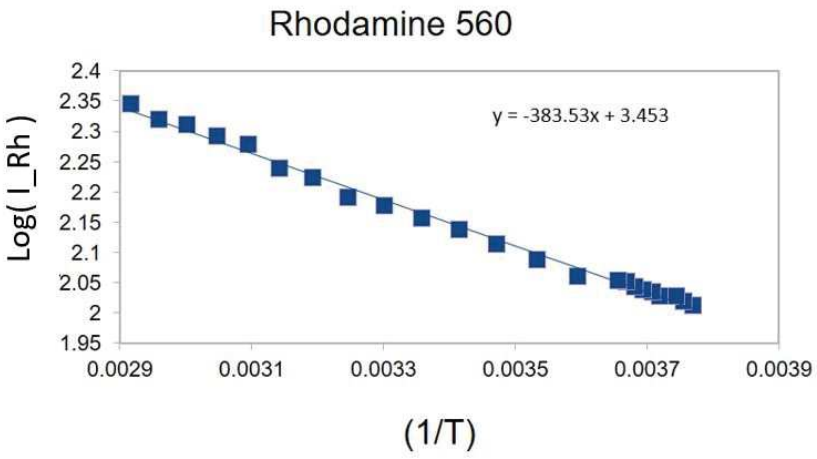


FIGURE 2.4: Fluorescent intensity of Rhodamine560 in function of the temperature.

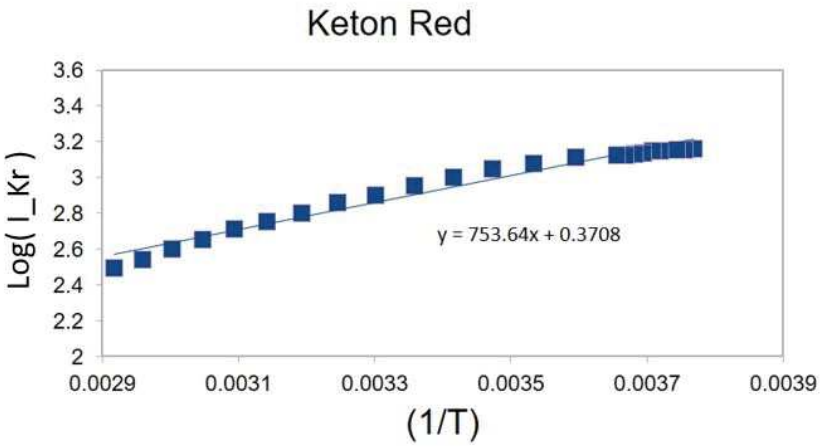


FIGURE 2.5: Fluorescent intensity of Kiton Red in function of the temperature.

From the figures 2.4 and 2.5, where the variation of fluorescent intensity is represented in the function of the temperature , we can see that the two fluorescent dyes behave in an opposite way with temperature. The decrease in Kiton Red fluorescent intensity is higher than the slight increase of Rhodamine 560 with increasing temperature. Hence, this combination of fluorescent dyes results in a fluorescent ratio which is highly sensitive to temperature. The resultant fluorescent ratio of Kiton Red and Rhodamine 560 solution represented in figure 2.6 decreases almost linearly with increasing temperature.

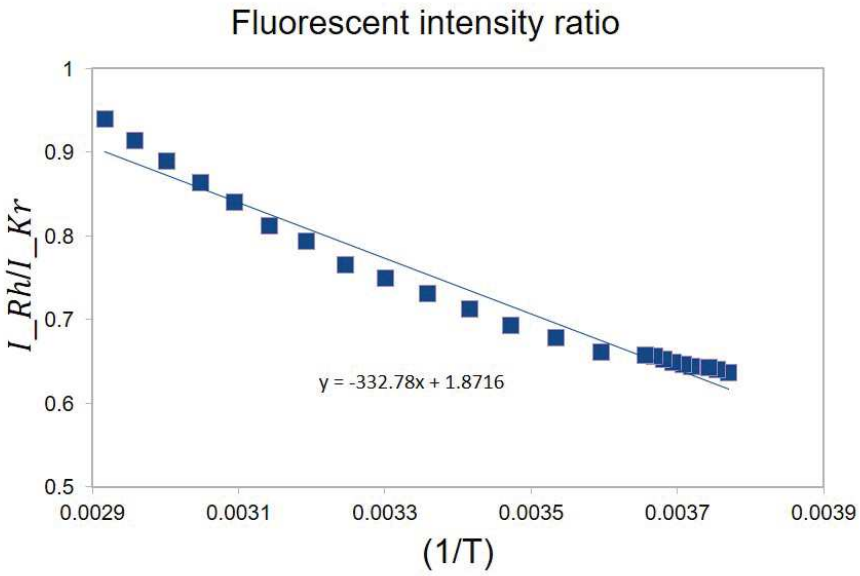


FIGURE 2.6: FLuorescent intensity ratio of Rhodamine560/ Kiton Red in function of the temperature.

## 2.3 Experiment Setup

### 2.3.1 Convection Cell

The Rayleigh Bénard convection cell used in this thesis is of aspect ratio 1. The cell shown in the figure 2.7 is a cylindrical cell of 10 cm height and 10 cm diameter, carved into a polymethylmetacrylate cube of 20 x 20 x 20 cm. The external flat surfaces of the cube ensure a good optical access to the interior of Rayleigh Bénard cell. A cooling chamber with continuous water circulation is placed above the cylindrical part of the cell. The water circulation chamber and the cylindrical inner cell are separated using a conductive circular sapphire plate. An O ring seal is wrapped around sapphire plate to ensure no liquid leakage between the cooling chamber and the inner cylindrical cell. Water is pumped to the cooling chamber using an external heat bath (RTE 7, ThermoFisher Scientific). Thermocouples are placed inside the circulating water tube to determine the temperature of the cooling chamber. The bottom plate of the inner cylindrical cell is made of oxygen free copper. A groove is carved on the lower face of the copper plate, into which a resistive wire is glued using conductive epoxy. The groove sweeps the entire bottom surface ensuring uniform heating to the bottom plate. A power supply (Agilent Technologies E3634A) is giving current to the resistive wire to generate heat by Joule law. Thermocouples are placed inside the copper plate to determine the temperature. With this setup, it is possible to change the temperatures of the bottom hot copper plate and the top cold saphire plate separately.

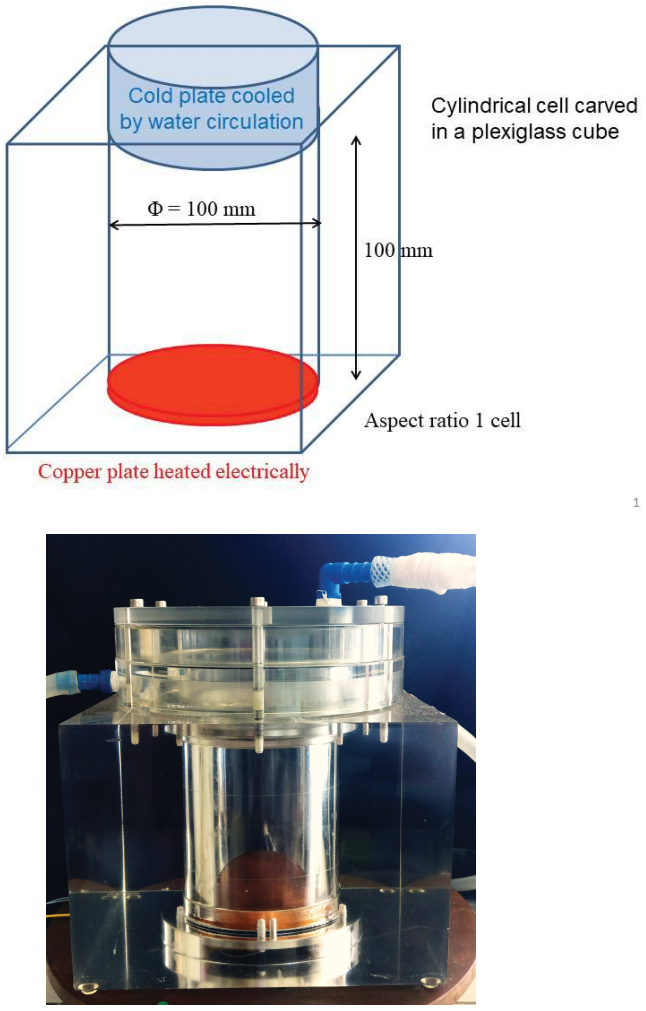


FIGURE 2.7: Rayleigh Bénard Convection Cell.

### 2.3.2 LIF Experiment Setup

A laser of 532nm is used to illuminate the cell. An optical setup containing a cylindrical lens is attached to the laser to form a laser sheet. The laser sheet passes through the mid vertical plane of the RBC cell. An optical setup containing two cameras is placed in an orthogonal direction to visualize plumes. This optical setup consists of an objective, a beam splitter and two band pass filters attached each to the two PCO scientific CMOS cameras. The objective focuses on the mid vertical plane of the RBC cell. The fluorescent emission light passing through the objective, is split into two beams by the beam splitter. Band pass filters filter the fluorescent emission to select the intensities in specific wavelength band. The scientific CMOS cameras record the emission fluorescent intensity corresponding to each fluorescent dye. Band pass

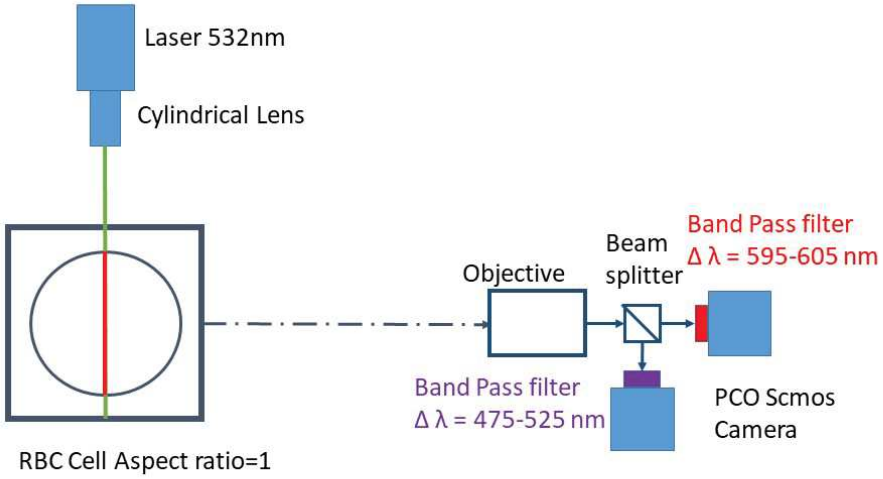


FIGURE 2.8: Laser Induced Fluorescence experimental Setup.

filters are selected based on the fluorescent spectra of the dyes. For example, the band pass filter for Kiton Red selects the fluorescent intensity of the solution in the range of 595-605 nm only. Similarly, the band pass filter for Rhodamine 560 selects the light intensity in the range of 475-525 nm only. Hence, this setup can record the light intensity at two different wavelengths simultaneously.

### 2.3.3 LIF experiment procedure

- After setting the optical setup and filling the cell with the working fluid, a grid pattern consisting of lattice of points is inserted in the mid vertical height of the cell. This grid helps us to divide the intensity of the Rhodamine emission image by the intensity of the Kiton Red image point by point. Images of the grid are recorded by the two cameras.
- Equal mean temperature at top and bottom of the cell is maintained. Images are recorded at this reference temperature for two different wavelengths. Also, black images without any illumination are recorded. These reference images are used to remove the background illumination defects in the image.

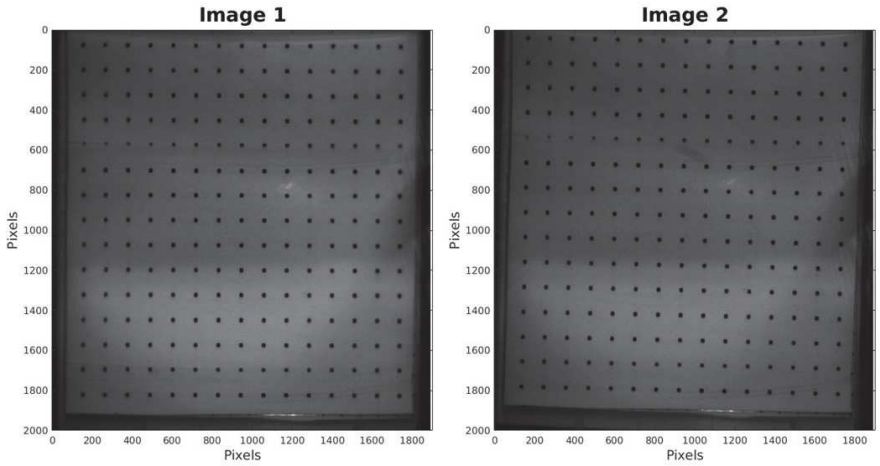


FIGURE 2.9: Images of both cameras before transformation.

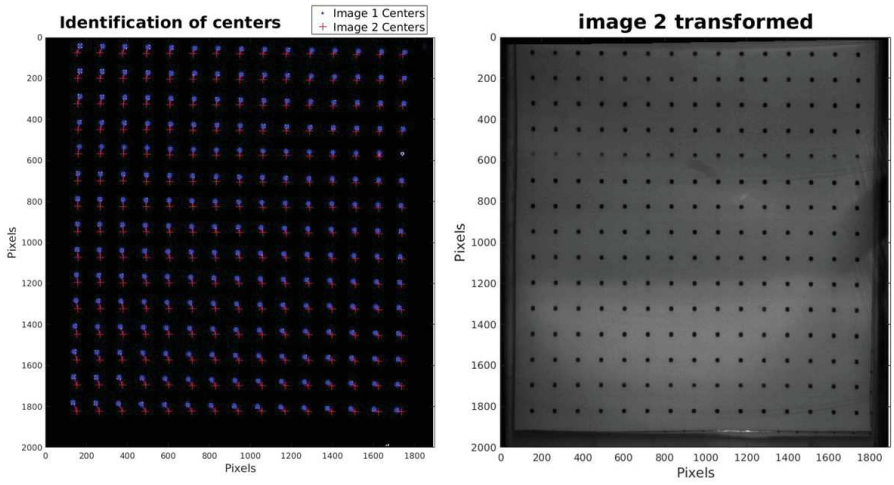


FIGURE 2.10: Location of centers of two images (left).Transformed Image 2 (right)

- The top plate is cooled at specific temperature using a thermostatic bath. The bottom plate is heated at the required temperature using resistive power heating. The flow is stabilized with the temperature difference for half an hour before beginning the experiment.
- The mid plane is illuminated with the laser sheet. The flow field is recorded at two different wavelengths simultaneously using pco scmos camera optical setup.

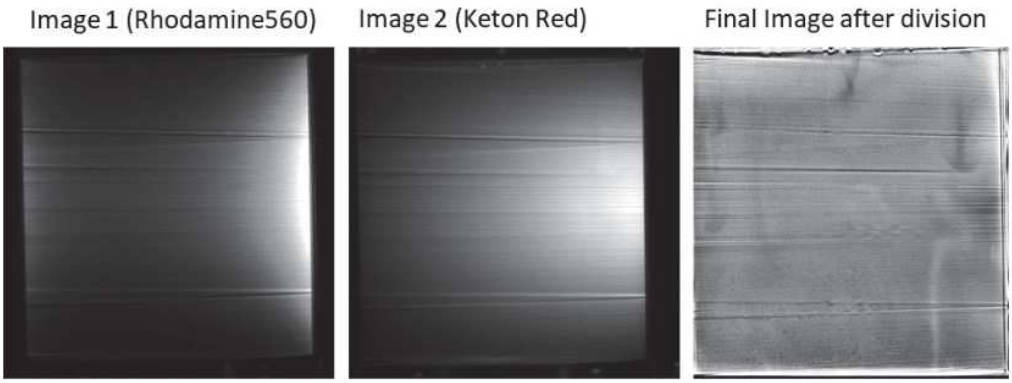


FIGURE 2.11: Images division removes illumination defects

- Post Processing: Each image is subtracted from black image and divided by the reference image taken at the mean uniform temperature. A program is written in MATLAB to calibrate the transformation of images for proper overlap of the images using the grid pattern. This transformation is applied to the recorded images. Finally images of Kiton Red are divided by the respective Rhodamine560 images to obtain image consisting of fluorescent intensity ratio. Division of image removes the incident light non homogeneity as shown in figure 2.11. The temperature is calibrated globally in the flow field from the fluorescent intensity ratio using equation 2.18 .

For the rotating experimental setup, the same procedure is applied. The entire system is mounted on the rotating table. RBC cell is placed in the center of the rotating table. The optical setup is mounted on the vertical bars as shown in figure 2.12. Mirrors are used additionally to illuminate the flow field and to record the output fluorescent intensity. Images are recorded after the flow is stabilized at specified temperature differences under specific speed of rotation.

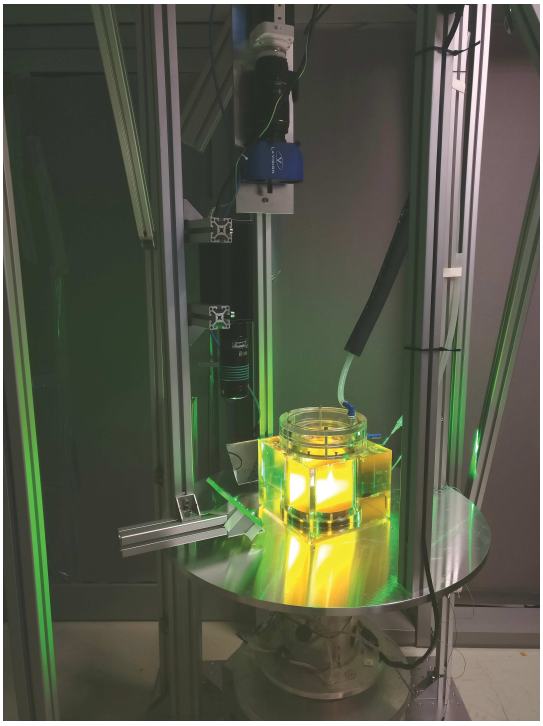

FIGURE 2.12: Rotating experimental Setup.

## 2.4 Particle Image Velocimetry

In the early $18^{th}$ century, pitot tubes and hot wire anemometers were used to measure velocity. These involve probes which are intrusive in the fluid flow. Hence in quest for non intrusive velocity measurement techniques, researchers developed Laser Doppler Anemometers (LDA) and Laser Two point Anemometry (LTA). Although these methods use non intrusive laser probe, the technique is a local point wise measurement. To make non intrusive global flow velocity measurements, Particle Image Velocimetry (PIV) has been developed.

PIV is also developed as a result of the development of flow visualization techniques. Initially, the complex dynamics in turbulence are visualized by using smoke or by mixing dyes into the liquids. These earlier visualization techniques helped in creating a visual picture of invisible phenomena. Optical systems aided to study fast changing flows to be recorded and played at a comprehensible speed. To test experimentally various turbulence theories, the earlier visualisation techniques could not provide quantitative flow measurements. With the advancement of image processing and digitization techniques, quantitative data can be retrieved from the visualized flow. Thus PIV experiment technique is developed as an advanced flow visualization technique.

### 2.4.1 Measurement Principle

Particle Image Velocimetry is described in detail by Raffel et al., 2018. The step by step procedure is as below

- The initial step is to introduce particles into the fluid. The tracer particles must have same density as the fluid. Higher density makes the particles to settle down in the system. Particles should not dissolve or chemically react with the fluid. Also the size of the particle should be optimum. If the particle size is very large, they create velocity lag and do not follow the flow accurately. If the particle size is too small, they do not have high light scattering efficiency. Particles must be seeded moderately. Too many particles would lead to a long absorption of the laser light and therefore to a non uniform laser sheet intensity.

- The particles in the plane or volume of interest are illuminated by a light source. Usually lasers are used in PIV because they emit monochromatic light. An optical setup with a cylindrical lens arrangement can be used to change the high energy density laser light to a thin sheet. Laser sheet can be projected onto the plane of interest.
- The light scattered by the tracer particles is recorded by a camera. Instantaneous measurements are recorded in sequence of frames. With the advancement in digital image recording techniques, a charge coupled device (CMOS high speed camera) is the most commonly used device for recording in the PIV technique.
- After recording sequence of images, the displacement of particle in between the images has to be converted in terms of the displacement of particle in the actual flow field. The distance traveled by each particle in the flow field is calculated from the recorded images using image evaluation algorithms such as correlation and Fourier transformation.
- If the initial frame is recorded at time 't' and next frame is recorded at time $'t + \Delta t'$ then, the velocity of each particle is calculated based on the time difference between the frames and the distance traveled. The time duration between successive images should be optimum. It should be large enough to determine the displacement in between the images. It should also be short enough so that the particle positions can be correlated.
- The resultant data may involve certain errors due to illumination and other defects. These invalid readings are removed and the final collected data are analyzed statistically to derive various flow characteristics.

## 2.5 PIV Experiment Setup

A two dimensional Particle Image Velocimetry is used to visualize flow and measure velocity in the mid vertical plane of RBC cell. Experiment setup includes a laser and RBC cell equipment similar to the LIF experiment setup described previously in chapter 2.3. The fluid (water) is seeded with silver coated particles of diameter $10\mu m$ and density equal to the water density $(1g/cm^3)$. The inner cylinder of RBC cell is filled with the seeded water. The required temperature difference is stabilized between the bottom hot plate

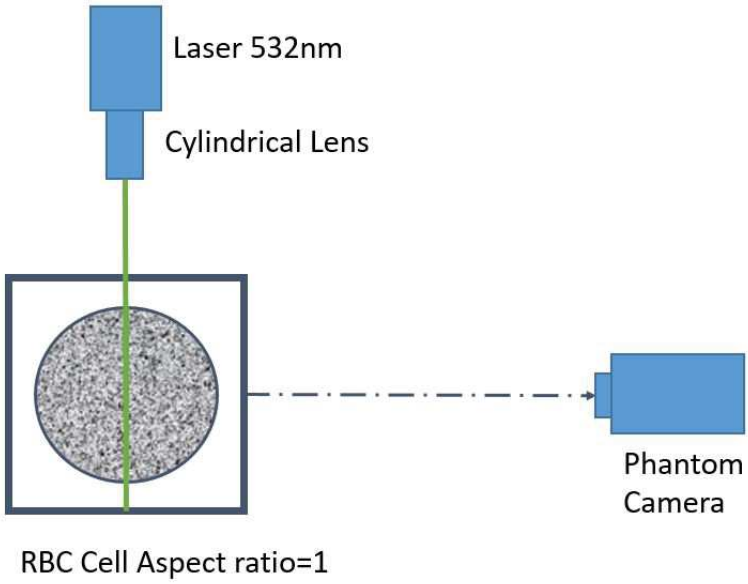


FIGURE 2.13: Particle Image Velocimetry experiment Setup.

and top cold plate of the inner cylinder of the RBC cell. In case of rotating experiment, the temperature is stabilized at the required rotation rate.The laser sheet is used to illuminate the particles in the mid vertical plane of the cell. A Phantom micro 110 CMOS camera of 12 bits is used to record the instantaneous flow field from the front side of the cell. The recorded sequence of images are post processed using PIVLab tool in MATLAB software developed by Thielicke et al., 2014.

# Chapter 3

# Velocity Statistics in Rotating Rayleigh Bénard Convection

## 3.1 Introduction

By increasing the rotation rate, the flow regime changes from LSC (or rotation unaffected regime) at low rotation rates to vortical columns after critical rotation rate (for more information see section 1.5.2). In this chapter we investigate this transition based on the velocity flow field characteristics obtained from the PIV measurements. First, the mean flow is studied near transition to determine the effect of the Rossby number on the general flow field and to observe the transitions. Flow statistics such as auto-correlation and cross-correlation of velocity are used to define the flow near the transition. The experiments are conducted at three different Rayleigh numbers (5.3e+8, 2.7e+8, 1.4e+8), Prandtl value 5.6 and at various rotation rates $(0.1 < Ro < \infty)$. Flow behavior is analyzed by comparing velocity at mid height to the velocity near top and bottom plates.

## 3.2 Mean Velocity Flow Field

The mean velocity flow field is represented in the figure 3.1. The figures show a clear transition in the mean flow structure from LSC to vertical columns. LSC is the predominant flow structure for non rotating RBC and for rotating RBC at low rotation rate i.e. in the rotation unaffected regime $(i.e. Ro = \sqrt{g\alpha\Delta T/H}/2\Omega > 2.5)$. In the rotation affected regime, at moderate rotational speed, $0.15 < Ro < 2.5$ the mean velocity flow structure begins to change from the large scale circulation. At fast rotation rate, below $Ro < 0.15$

the regime is dominated by rotation (Stevens et al., 2009, Zhong et al., 2010) and the mean velocity indicates the presence of vertical columns.

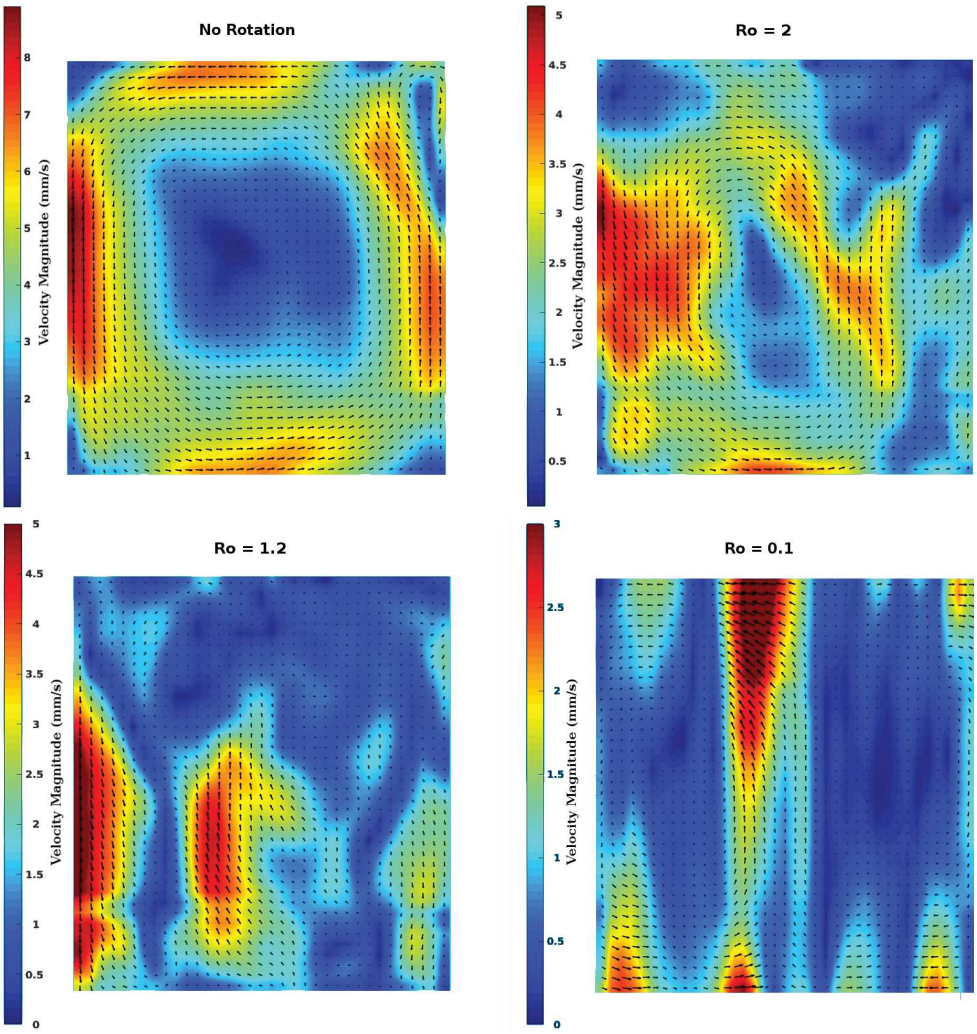


FIGURE 3.1: Mean Velocity Flow field averaged over 67 seconds with velocity magnitude represented in the contour at Ra = 2.7e+08, Pr = 5.6 and at various Rossby numbers

Ekman pumping causes vorticity to develop inside the boundary layer after a critical speed of rotation. The vorticity developed inside the boundary layers, decreases as one moves away from the boundary layers to the bulk and takes the shape of vertical columns. From the theoretical predictions of Veronis, 1959 and numerical simulations of Ribeiro et al., 2015, we understand that, to conserve the angular momentum, the vertical columns taper from the boundary layers till the mid height of the cell and then spin in opposite direction as they approach the other end of the cell. Hence, cyclonic/anticyclonic vortices developed near the top plate change into anticyclonic/cyclonic vortices respectively, as they approach the bottom plate of the cell. To describe

this phenomena quantitatively from our 2D flow visualization, we correlate the horizontal velocity near the top and bottom plates (see chapter 3.4).

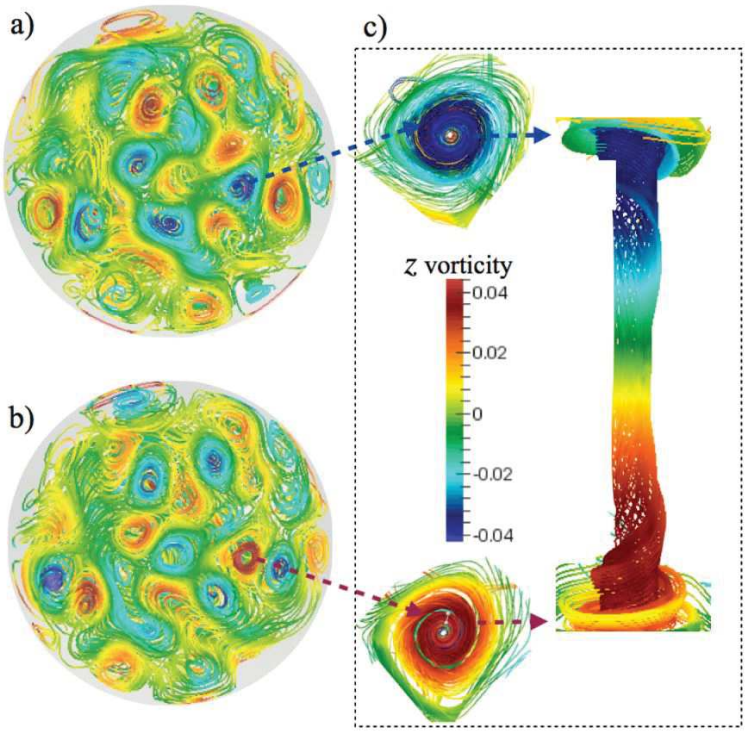


FIGURE 3.2: (a,b) Top view of vorticity near the top and bottom boundary layers (c) Oscillatory vertical column Ribeiro et al Ribeiro et al., 2015

## 3.3 Strength of LSC

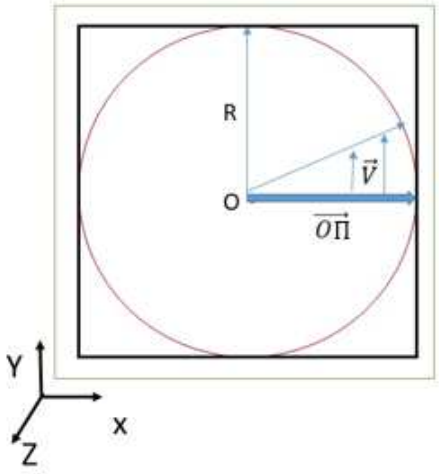


FIGURE 3.3: Calculation of strength of LSC in the plane of measurement (Schematic representation), R = 47mm

In the rotating Rayleigh Bénard convection the LSC is the predominant flow structure in the rotation unaffected regime. The strength of Large Scale Circulation is estimated by considering that the flow in the bulk of the cell and in the plane of the LSC is a "$flywheel$". The PIV analysis gives a square lattice of about 35 to 40 vectors in each direction. The PIV velocity vectors are equally spaced of about 2.5 mm apart in each direction. By considering the velocity vectors present in a circle, whose center is the geometric center of the cell, with radius approximately equal to the width of the cell, the strength of the LSC in the plane of observation can be calculated. In the present work, we loose information from the boundary layers of thickness less than 1mm. Hence the radius of circle is approximately 47mm where as the half width of the RBC cell is 50mm. For each point $\Pi_i$ on the square lattice formed by the velocity vectors obtained by PIV, there is an associated velocity vector $\overrightarrow{V_i}$. In considering only the points inside the previously defined circle, the cross product $(\overrightarrow{S_t} = \Sigma_i(\overrightarrow{O\Pi_i} \text{ x } \overrightarrow{V_i}))$ gives the estimate of the LSC strength in the plane of observation at time t. The LSC strength is in the z direction, so it can also be written as $\overrightarrow{S_t} = S(t)\overrightarrow{z}$.

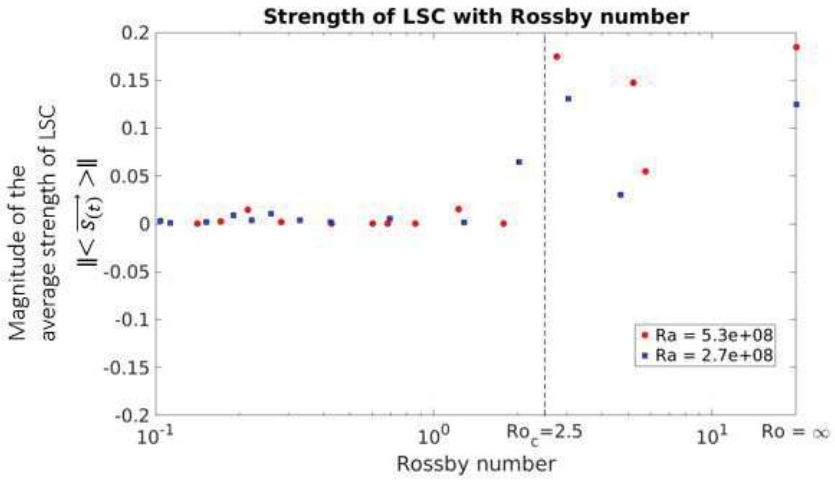


FIGURE 3.4: Time averaged strength of large scale circulation in the plane of observation at various Rossby values.

Figure 3.4 shows the variation of the absolute value of the time averaged LSC strength *i.e.* $\| \langle \overrightarrow{S_t} \rangle \|$ with rotation at different Rossby numbers. From the figure 3.4, we can observe that the strength of large scale circulation increases near the critical Rossby = 2.5. In the rotation affected regime, beyond the critcal rotation rate, the LSC is not the predominant flow structure. Hence, the strength of LSC decreases and becomes approximately zero.

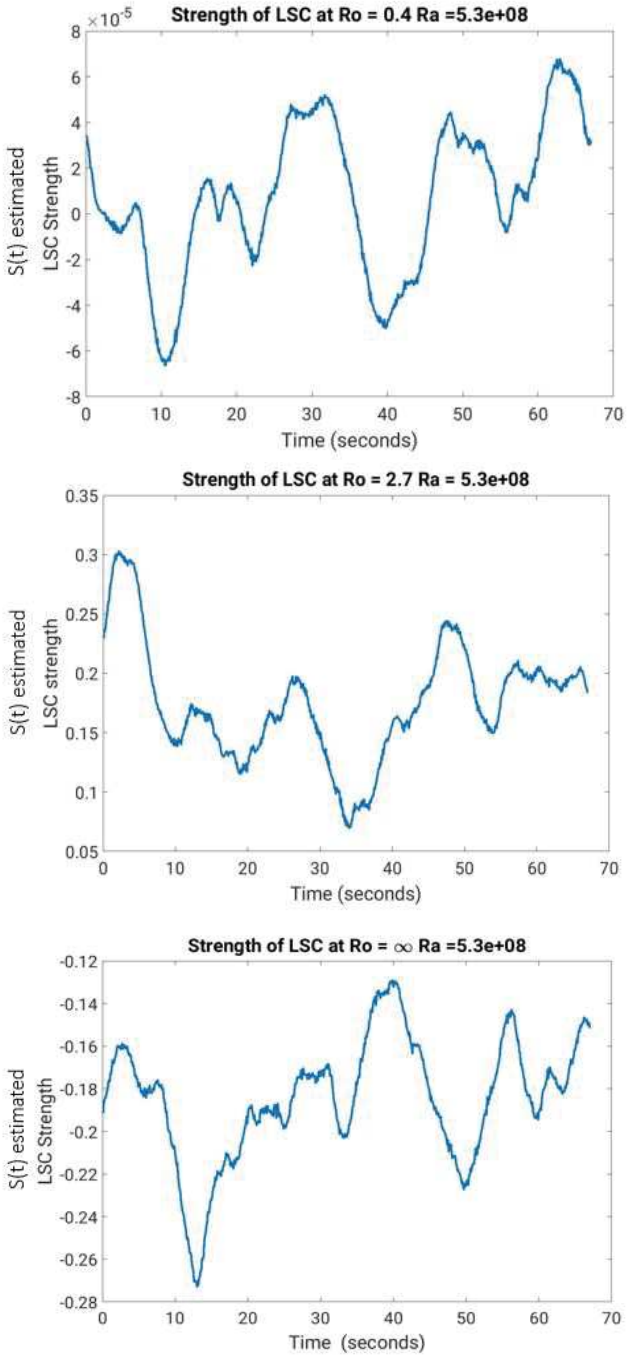


FIGURE 3.5: Temporal evolution of the estimated strength of LSC in the plane of observation at Ro = ∞ (bottom), Ro = 2.7 (middle) Ro = 0.4 (top ).

From figure 3.5 we can notice that, in rotation affected regime, at Ro=0.4, (i) the strength of LSC is several orders of magnitude smaller than in the rotation unaffected regime and (ii) the variation of strength of LSC in time, is changing the sign from positive to negative. Strength of LSC varies around a mean value of zero in the rotation affected regime. When LSC is the predominant

flow structure *i.e.*$(Ro > 2.5)$, the temporal evolution of the strength of LSC remains either positive or negative depending on the direction of the rotation. The velocity, frequency and turn over time of the large scale circulation in rotation unaffected regime at various Rossby numbers are given in table 3.1. Velocity of large scale circulation is measured by considering average velocity in a rectangular region, extending from $1/4$ th distance from the center of the cell to the side wall. The LSC frequency is defined as $Frequency = LSCvelocity/2 * \pi$ and $Turnovertime = 1/Frequency$.

| Ra = 5.3e+08 Pr = 5.6 | | | | |
|---|---|---|---|---|
| Rossby number | 2.76 | 5.21 | 5.76 | $\infty$ |
| LSC velocity (m/s) | 0.32 | 0.2 | 0.13 | 0.24 |
| Frequency ($s^{-1}$) | 0.05 | 0.03 | 0.02 | 0.04 |
| Turn over time (s) | 19.6 | 30.3 | 46.2 | 25.6 |

| Ra = 2.7e+08 Pr = 5.6 | | | | |
|---|---|---|---|---|
| Rossby number | 2.02 | 3.04 | 4.68 | $\infty$ |
| LSC velocity (m/s) | 0.15 | 0.17 | 0.14 | 0.14 |
| Frequency ($s^{-1}$) | 0.02 | 0.03 | 0.02 | 0.02 |
| Turn over time (s) | 41.7 | 35.3 | 45.5 | 43.4 |

TABLE 3.1: Properties of Large scale circulation at various Rossby numbers in the rotation unaffected regime.

## 3.4 Velocity near the top and bottom plate

From figure 3.6 of horizontal velocity contour, we can notice that the horizontal component of the instantaneous velocity is in opposite direction near the top and bottom plates on a given vertical line. This phase opposition indicates that the columns are rotating in opposite directions near top and bottom plates as observed by Ribeiro et al., 2015.

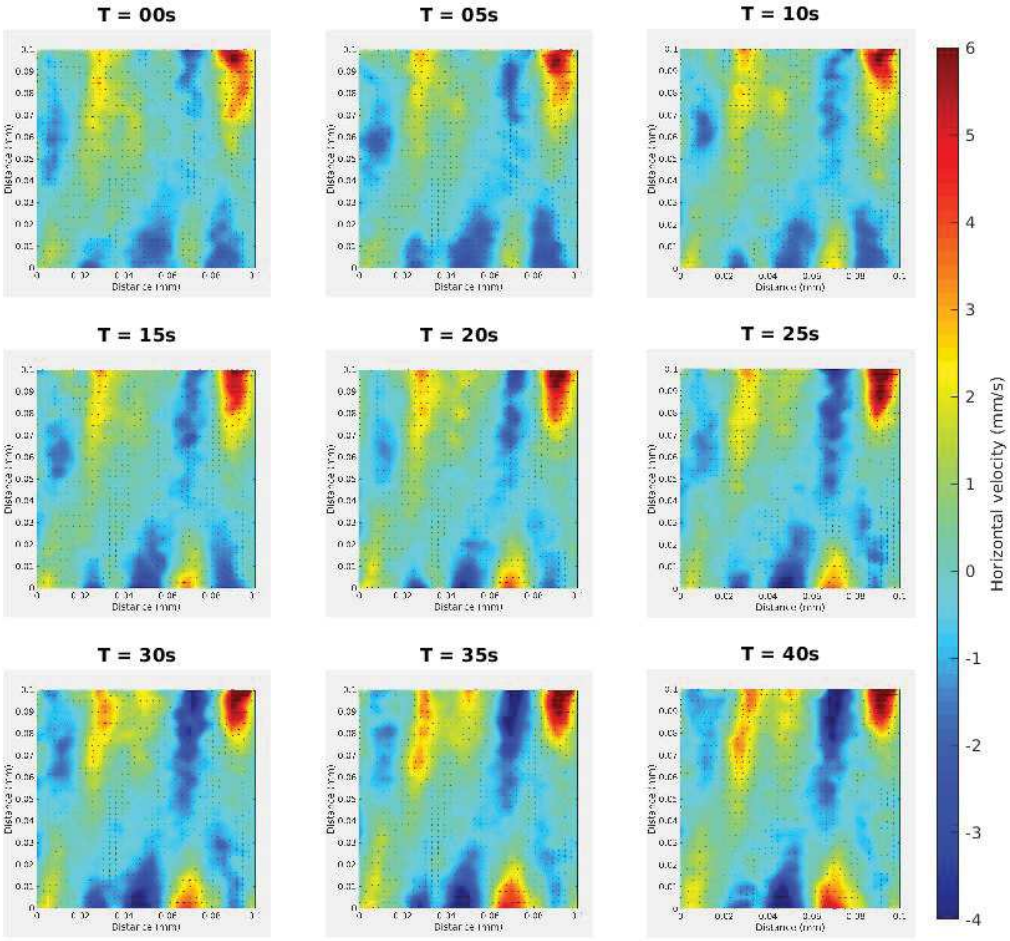


FIGURE 3.6: Instantaneous horizontal velocity at Ro = 0.1 , Ra = 2.7e+08

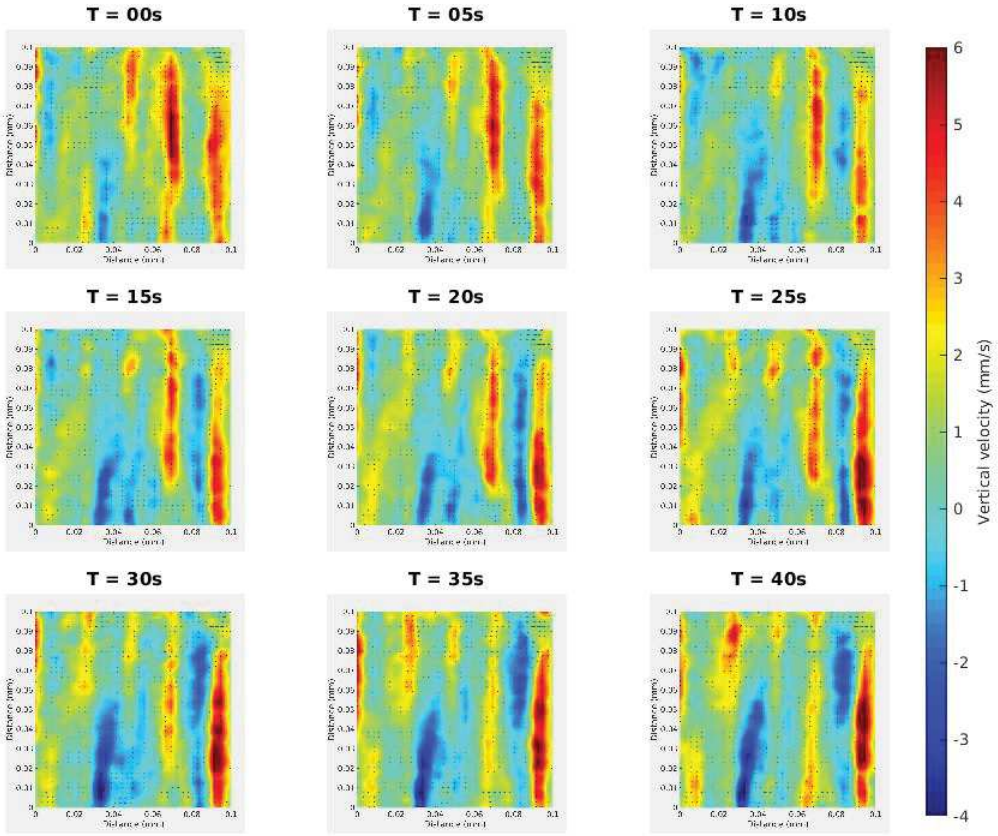


FIGURE 3.7: Instantaneous Vertical velocity at Ro = 0.1 , Ra = 2.7e+08

To study this phase opposition of the horizontal component of the velocity near the top and bottom plates, we plot the temporal evolution of horizontal velocity at three different vertical positions inside the cell, at 5 mm above the bottom plate, 5 mm below the top plate and at 50 mm mid height of the cell as shown in figure 3.8.

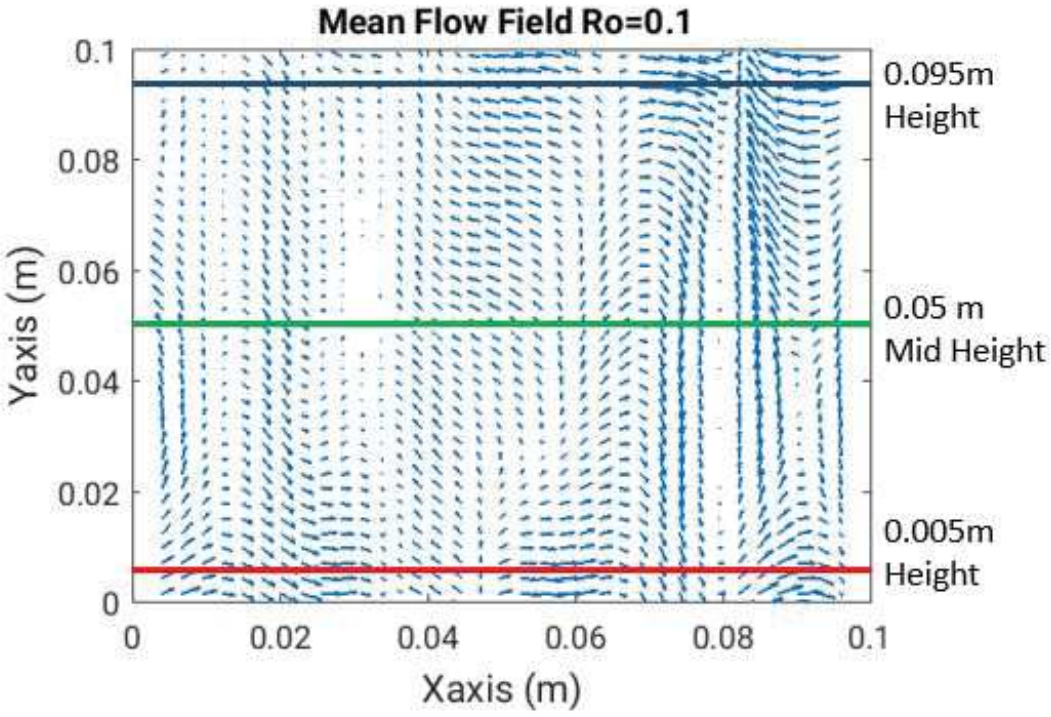


FIGURE 3.8: Vertical positions considered for velocity comparison ( The cell is 100mm in height and a diameter of 100mm ).

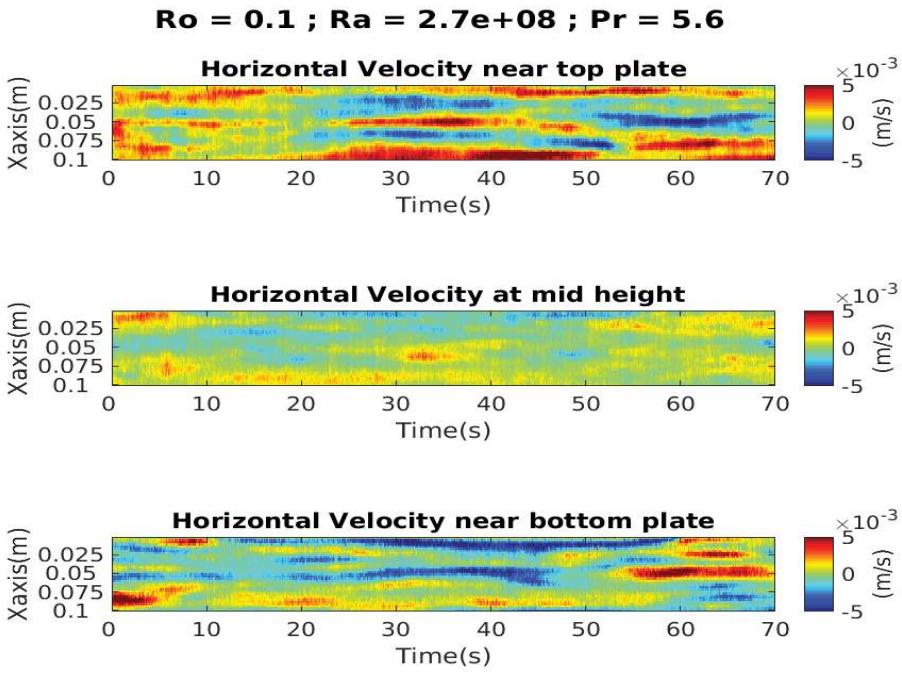


FIGURE 3.9: Horizontal velocity evolution in time at various heights for Ra = 2.7e+08, Pr = 5.6 and at Ro = 0.1

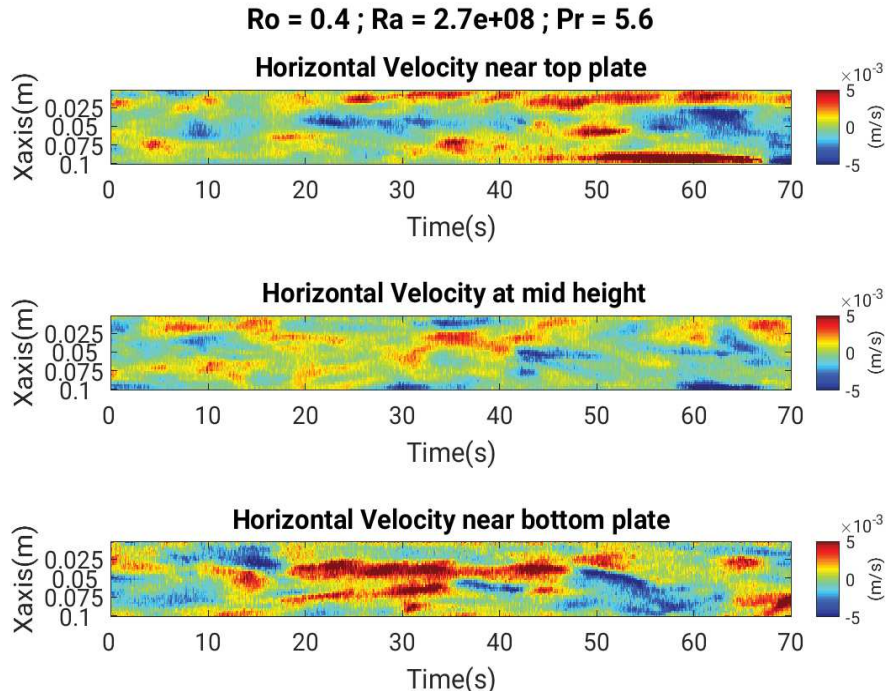


FIGURE 3.10: Horizontal velocity evolution in time at various heights for Ra = 2.7e+08, Pr = 5.6 and at Ro = 0.4.

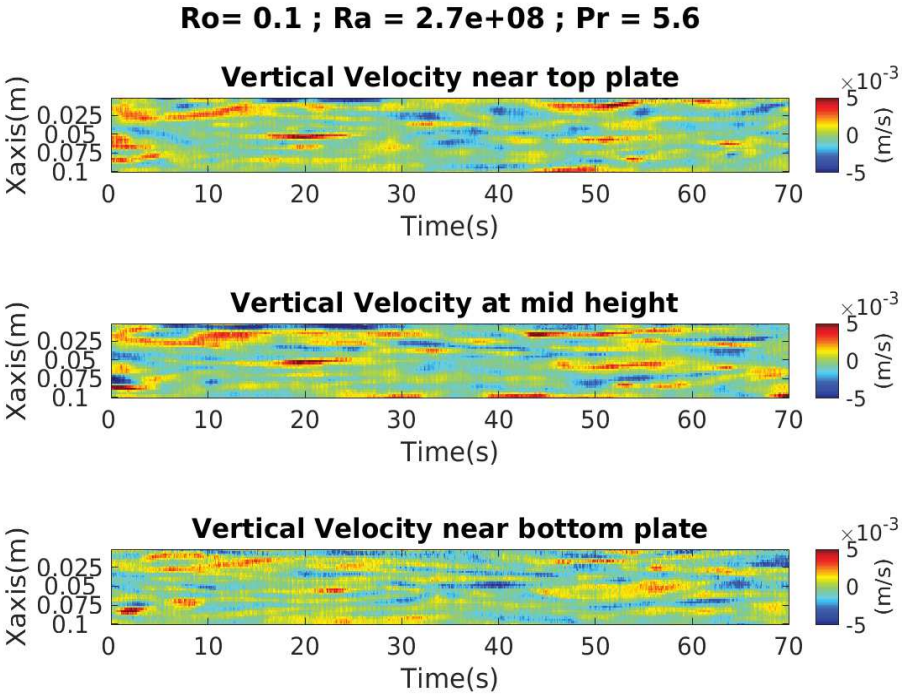


FIGURE 3.11: Vertical velocity evolution in time at various heights for Ra = 2.7e+08, Pr = 5.6 and at Ro = 0.1.

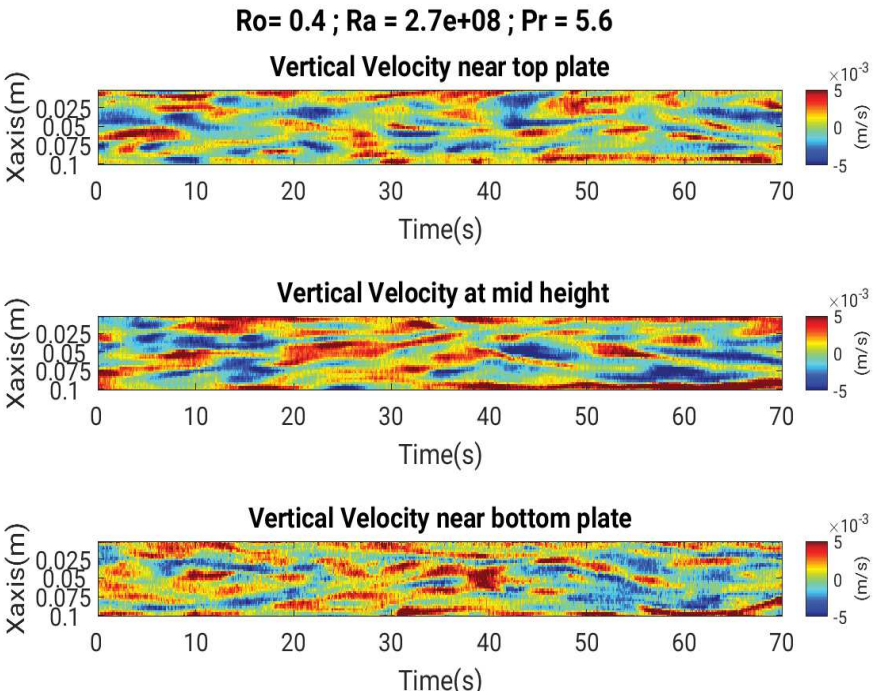


FIGURE 3.12: Vertical velocity evolution in time at various heights for Ra = 2.7e+08, Pr = 5.6 and at Ro = 0.4

The temporal evolution of horizontal velocity contour at various horizontal location is shown in figure 3.6, 3.10 . From the images we can observe that for a given horizontal location (x), the horizontal velocity which is positive near the bottom plate represented by red color, is negative near the top plate represented by blue color. This means that the direction of rotation near the top and bottom plates is opposite at a given horizontal location inside RBC cell. Where as, on average, the vertical velocity at a given horizontal location, near the top and bottom plates seems to be always in same direction from the bottom to the top plate as shown in figure 3.7 3.12. This explains that the fluid flow inside the columns moving upward/downward from the bottom plate move in the same direction until they reach the top plate and vice versa. To further quantify the above observations, spatial velocity cross correlation is calculated near the top and bottom plates.

## 3.5 Spatial Velocity Cross-correlation

Spatial velocity cross-correlation evaluates the spatial length until which the velocities at two different locations remain correlated. Spatial cross correlation of velocity at two different heights $(V_1, V_2)$ with a spatial lag $'d'$ can be defined as

$$R(d) = \frac{\frac{1}{N}\sum_{i=1}^{N}(V_{1_i} - \overline{V_1})(V_{2_{i+d}} - \overline{V_2})}{\sqrt{\frac{1}{N}\sum_{i=1}^{N}(V_{1_i} - \overline{V_1})^2}\sqrt{\frac{1}{N}\sum_{i=1}^{N}(V_{2_{i+d}} - \overline{V_2})^2}} \tag{3.1}$$

where N represents the number of velocity values measured experimentally by PIV (35 values in the case of our experiment) and $\overline{V}$ represents the mean of velocities over N values. The cross correlation is calculated for horizontal and vertical velocities near the top and bottom plates. The instantaneous spatial cross correlation is calculated at each time and then it is averaged in time for each Rossby value. The time averaged spatial cross correlation curves at various Rossby is represented in the figure 3.13.

### 3.5.1 Cross-correlation of horizontal component of the velocity

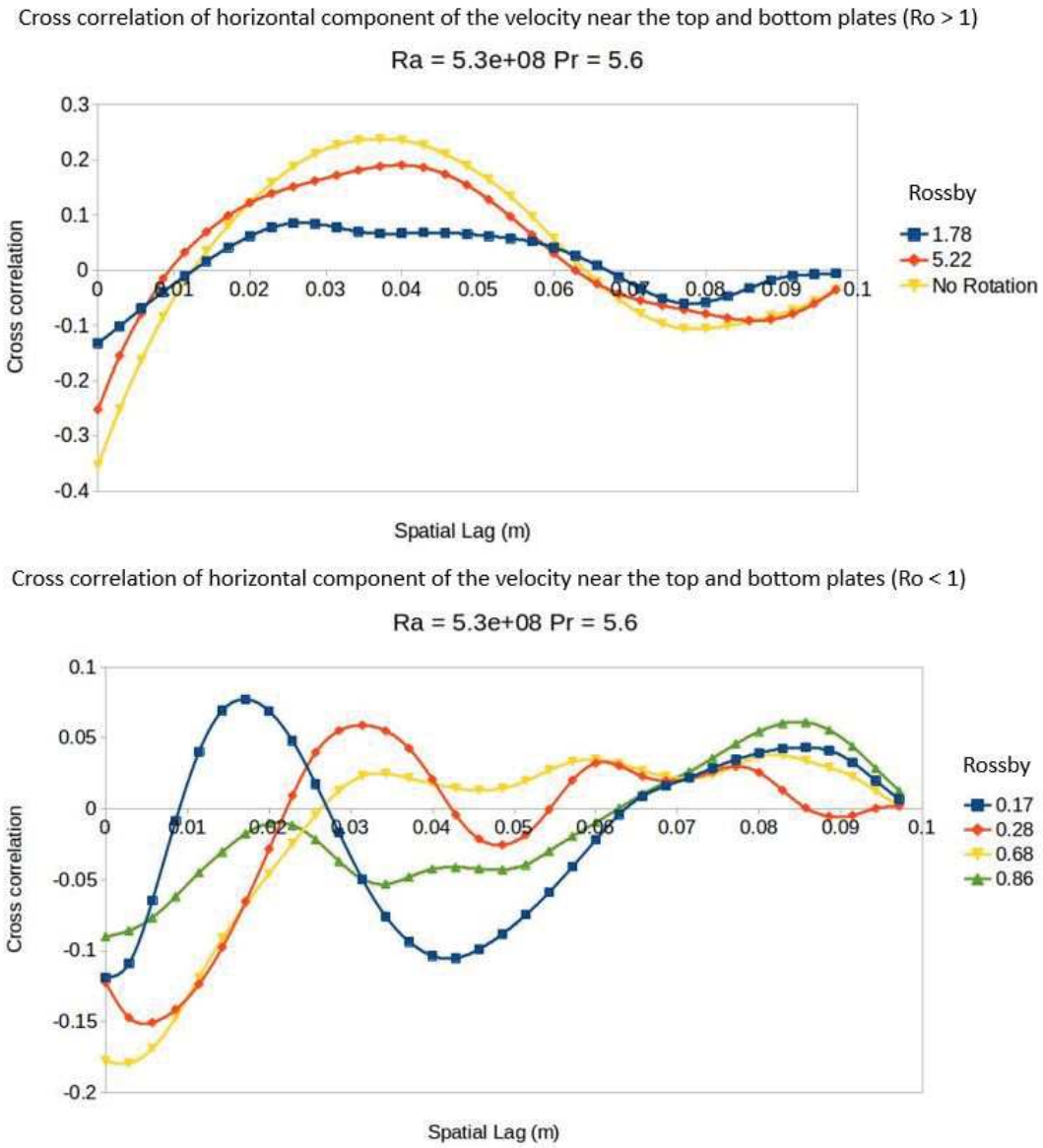


FIGURE 3.13: Cross correlation between the horizontal component of the velocity located near the top and bottom plates for rotation affected regime Ro < 1 (bottom) and rotation unaffected regime Ro > 1 (top).

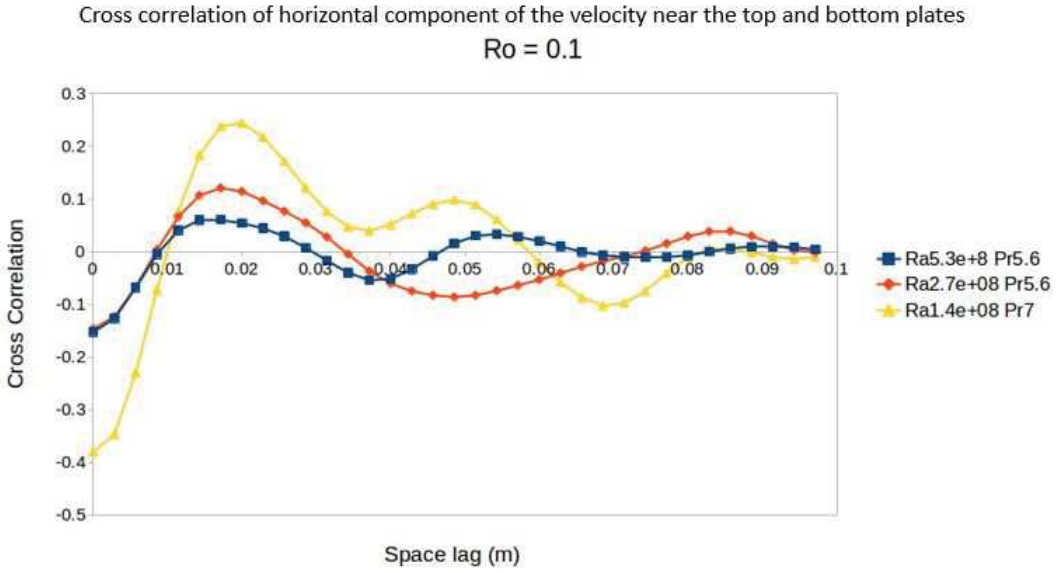


FIGURE 3.14: Cross correlation between the horizontal component of the velocity located near the top and bottom plates for Ro = 0.1 at Ra = 5.3e+08, 2.7e+08, 1.4e+08.

Figure 3.13 shows the time averaged spatial cross correlation of horizontal velocity for various Rossby at Ra = 5.3e+8 and Pr = 5.6 between the velocity at 5% height from the bottom plate and 95% height of the top plate. (i) In the rotation unaffected regime (high Rossby numbers), the negative correlation of horizontal velocity is stronger for large scale circulation since the flow is in opposite direction at all locations near the top and bottom plates. For all Rossby values the flow is negatively correlated near the top and bottom plates. (ii) In the rotation dominated regime ( $Ro < 1$ ) the cross correlation of horizontal velocity has wave form reflecting the spatial periodicity between the upward and downward going columns. With no spatial lag, the cross correlation shows that the horizontal velocity is out of phase near the top and bottom plates. This indicates that the vorticity of columns which are vertical, changes sign approximately in the horizontal plane cutting the cell in two halves.

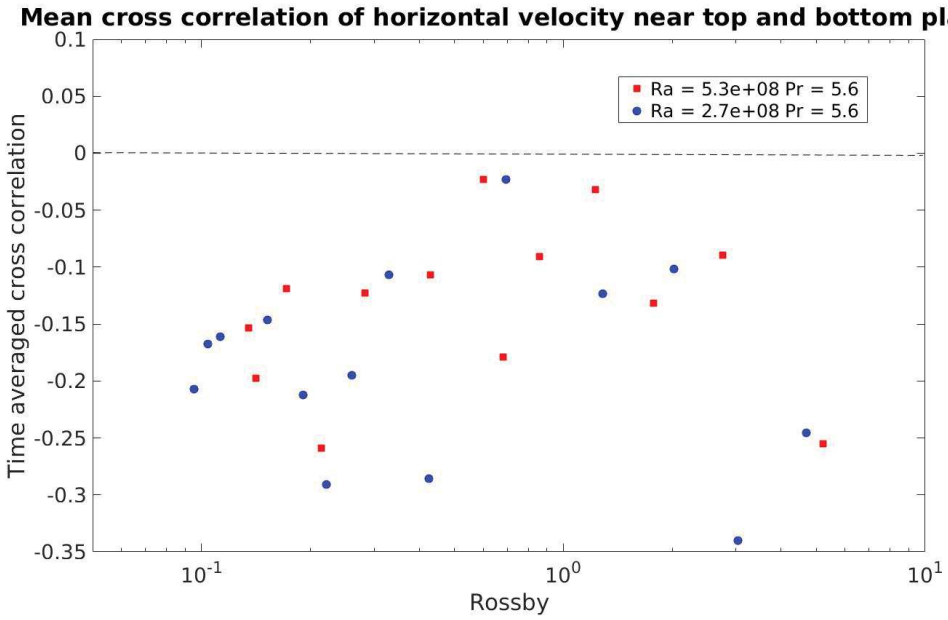


FIGURE 3.15: Mean Cross correlation of horizontal velocity located near the top and bottom plates at Ra = 5.3e+08 and 2.7e+08.

Figure 3.14 shows the cross correlation of the near top and bottom horizontal velocities at $Ro = 0.1$ for various Rayleigh values. For all Rayleigh values it is found that the cross correlation of horizontal velocity located 5mm away respectively from the top and bottom plate, are in phase opposition. We can estimate the strength of this out of phase correlation by considering the cross correlation between horizontal velocities at corresponding locations without spatial delay. The largest out of phase correlation is found at the largest rotation rate ( smallest Rossby = 0.1 ). For all Rayleigh and at all Rossby values considered in this work, at a given horizontal location, the time averaged cross correlation of the top and bottom horizontal velocities is negative as shown in figure 3.15. The out of phase cross correlation is maximum near the fastest rotation rates. It approaches the zero value near the critical Rossby number and again decreases for the LSC regime.

### 3.5.2 Cross-correlation of vertical component of the velocity

Vertical velocity is cross correlated near top and bottom plates, more precisely at 5% and 95% of the cell height for various Rossby and Rayleigh numbers. At all Rayleigh and Rossby values, the vertical velocity is positively correlated. No periodicity is observed in the rotation unaffected regime.

Whereas, periodicity appears clearly in the rotation affected regime. (see figure 3.16).

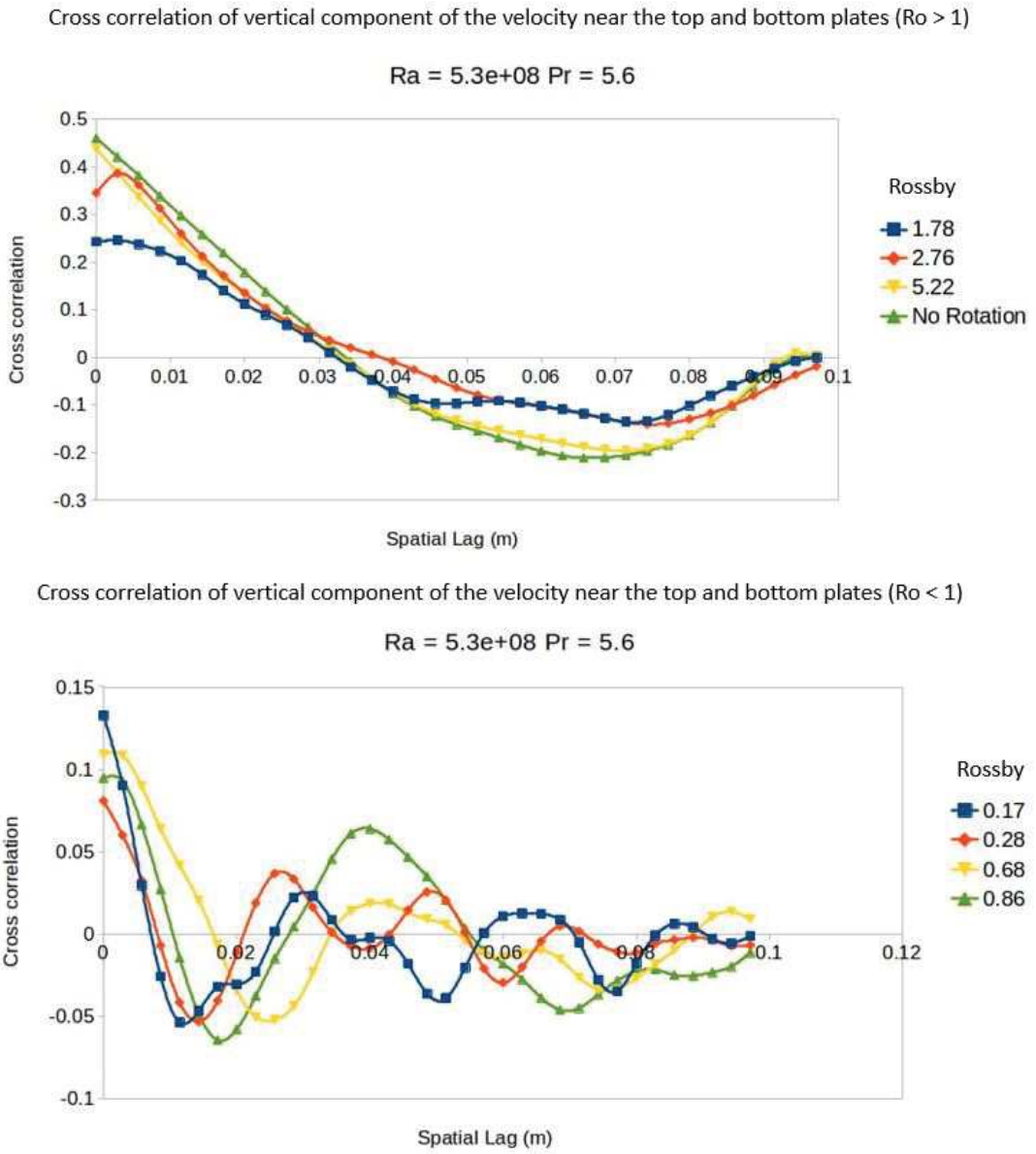


FIGURE 3.16: Cross correlation between the vertical component of velocity located near the top and bottom plates for Ro > 1 (top) and Ro < 1 (bottom).

Hence, vertical component of the velocity near the bottom and top plates is in the same direction for a given horizontal location. This may suggest that the hot/cold plumes traveling upward/downward close to the plate are traveling upward/downward until they reach the opposite plate and do not change direction in between meaning , the plumes travel vertically(see figure 3.7). In the horizontal direction, the columns are alternatively hot and cold

plumes extending vertically from one end of the plate to the other end of plate.

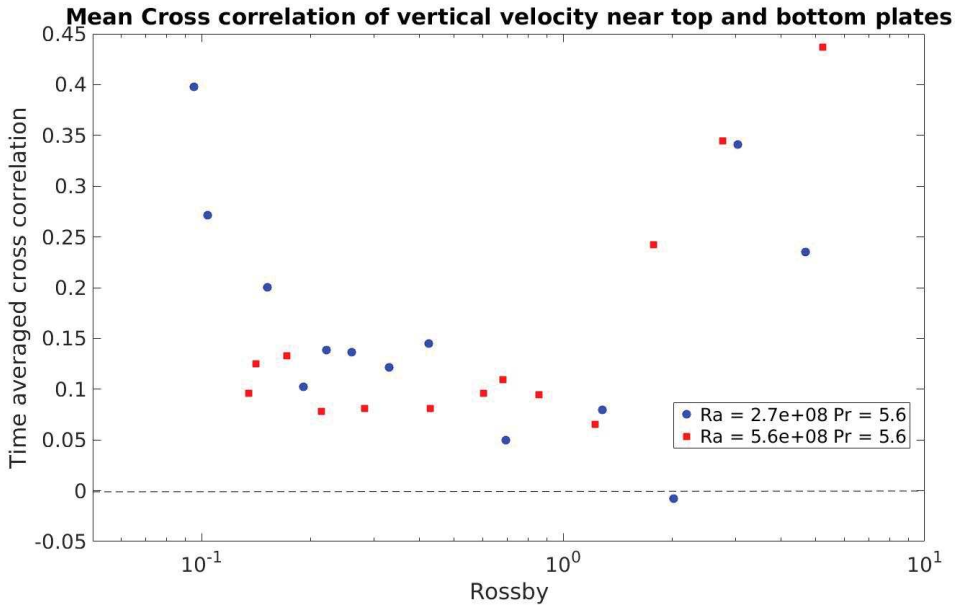


FIGURE 3.17: Mean cross correlation of the vertical component of the velocity located near top and bottom plates at Ra = 5.3e+08 and 2.7e+08

The spatial cross correlation of vertical component of the velocity near the top and bottom plate with zero lag is averaged in time for each Rossby and Rayleigh values (see figure3.17). The correlation between vertical component of the velocities near the top and bottom plates is high at the lowest Rossby number (fast rotation). This may indicate that the columns are well established at the fast rotation $(Ro = 0.1)$. This cross correlation approaches zero value near the critical Rossby number. Cross correlation of vertical velocities increases again for the rotation unaffected regime. This is similar but with opposite sign to the behavior of cross correlation of horizontal component of the velocities near the top and bottom plates.

The comparison between the horizontal and vertical velocity component cross correlations are represented in figures 3.18 and 3.19 . We know that the vertical columns that develop in the rotating Rayleigh Benard due to the Ekman pumping, grow with the Rossby number, all the way from top to the bottom plates. They are respectively in phase/out of phase cross correlation between the top and bottom vertical and horizontal component of the velocities. Hence, we can state that the columns near the bottom plate and the columns near the top plate are rotating in opposite directions. This has

been observed numerically (Ribeiro et al., 2015) and predicted theoretically (Veronis, 1959) but to our knowledge it is the first time that this is evidenced experimentally.

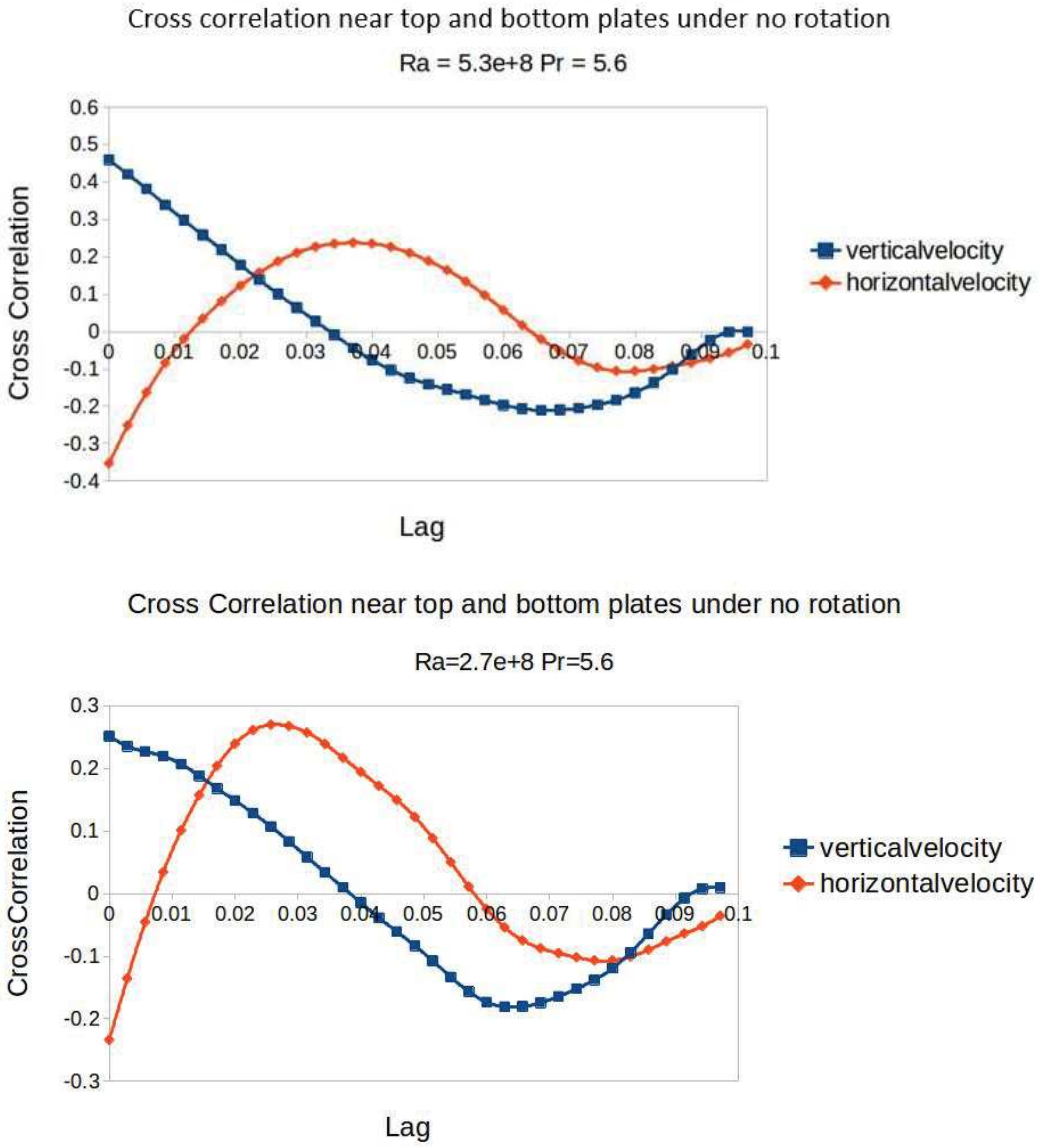


FIGURE 3.18: Horizontal and vertical component of the velocity cross correlation at $Ro = \infty$ (No rotation) and Ra = 5.3e+08 (top), 2.7e+08 (bottom)

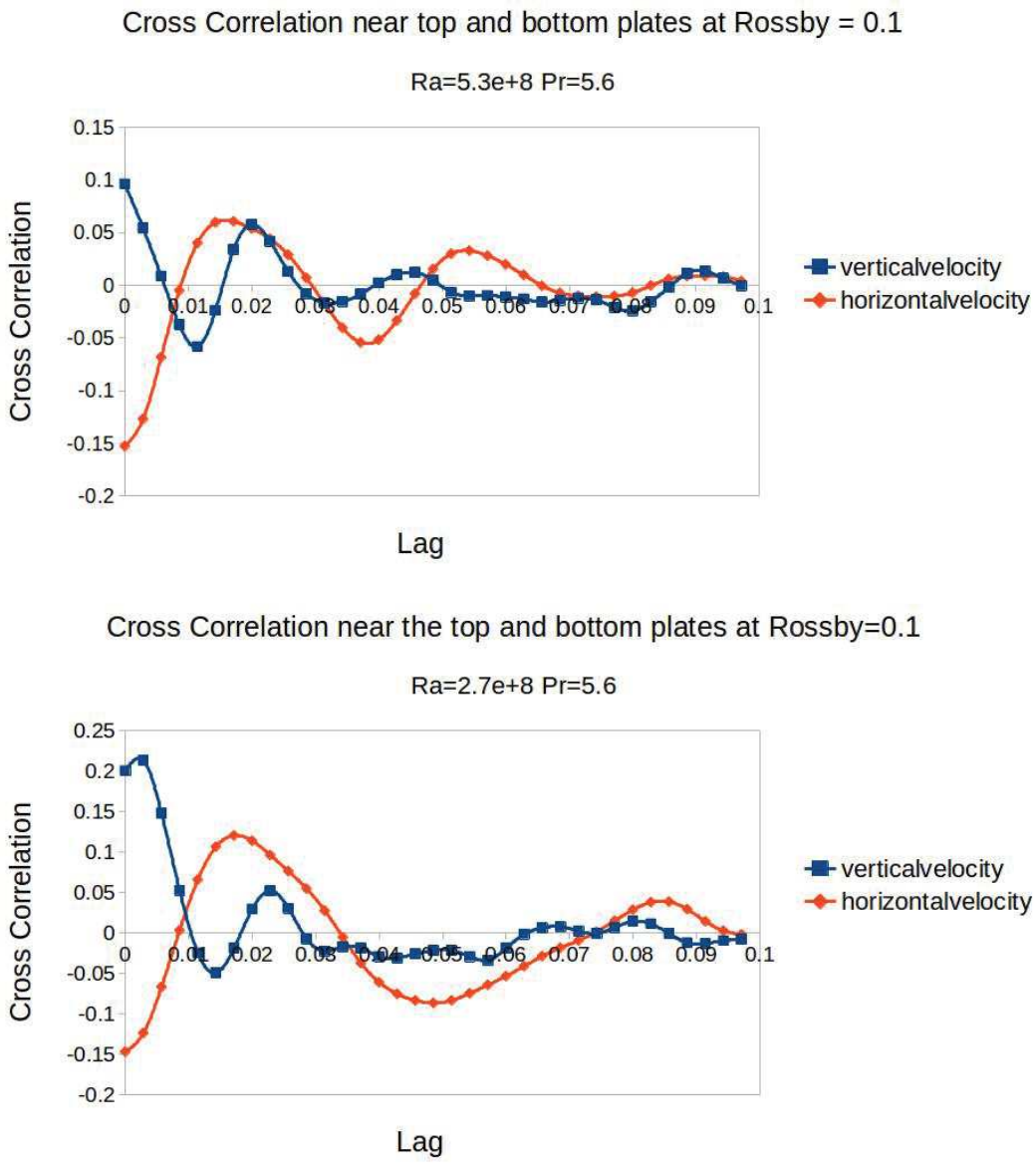


FIGURE 3.19: Horizontal and vertical component of the velocity cross correlation at Ro = 0.1 and Ra = 5.3e+08 (top), 2.7e+08 (bottom)

## 3.6 Spatial Velocity Auto-correlation

Our measurements show the complete vertical span of the columns formed at faster rotation rate. As already described in the literature and also in the velocity field representation in figure 3.1, it is to be observed that the number of columns increases with decreasing Rossby number. The width of columns also decreases with decreasing Rossby number. In order to be more quantitative, the spatial velocity auto-correlation is studied for various Rossby numbers.

The auto-correlation is the correlation of a signal with itself with a lag. The spatial auto-correlation of vertical component of the velocity on a horizontal line spanning the cell in its width, in a vertical plane going through the axis of symmetry of the cell, is used to define the approximate width of the columns. Spatial auto-correlation of velocity is defined as

$$R(d) = \frac{\sum_{i=1}^{N}(V_{1_i} - \overline{V_1})(V_{1_{i+d}} - \overline{V_1})}{\sum_{i=1}^{N}(V_{1_i} - \overline{V_1})^2} \tag{3.2}$$

where N represents the number of velocity values measured experimentally by PIV (35 values in the case of our experiment) and $\overline{V}$ represents the mean of velocities over N values. The spatial velocity auto correlation is calculated at various heights in the RBC cell, at each time and at each Rossby. The auto correlation of the vertical component of the velocity is averaged in time and then plot at various Rossby values.

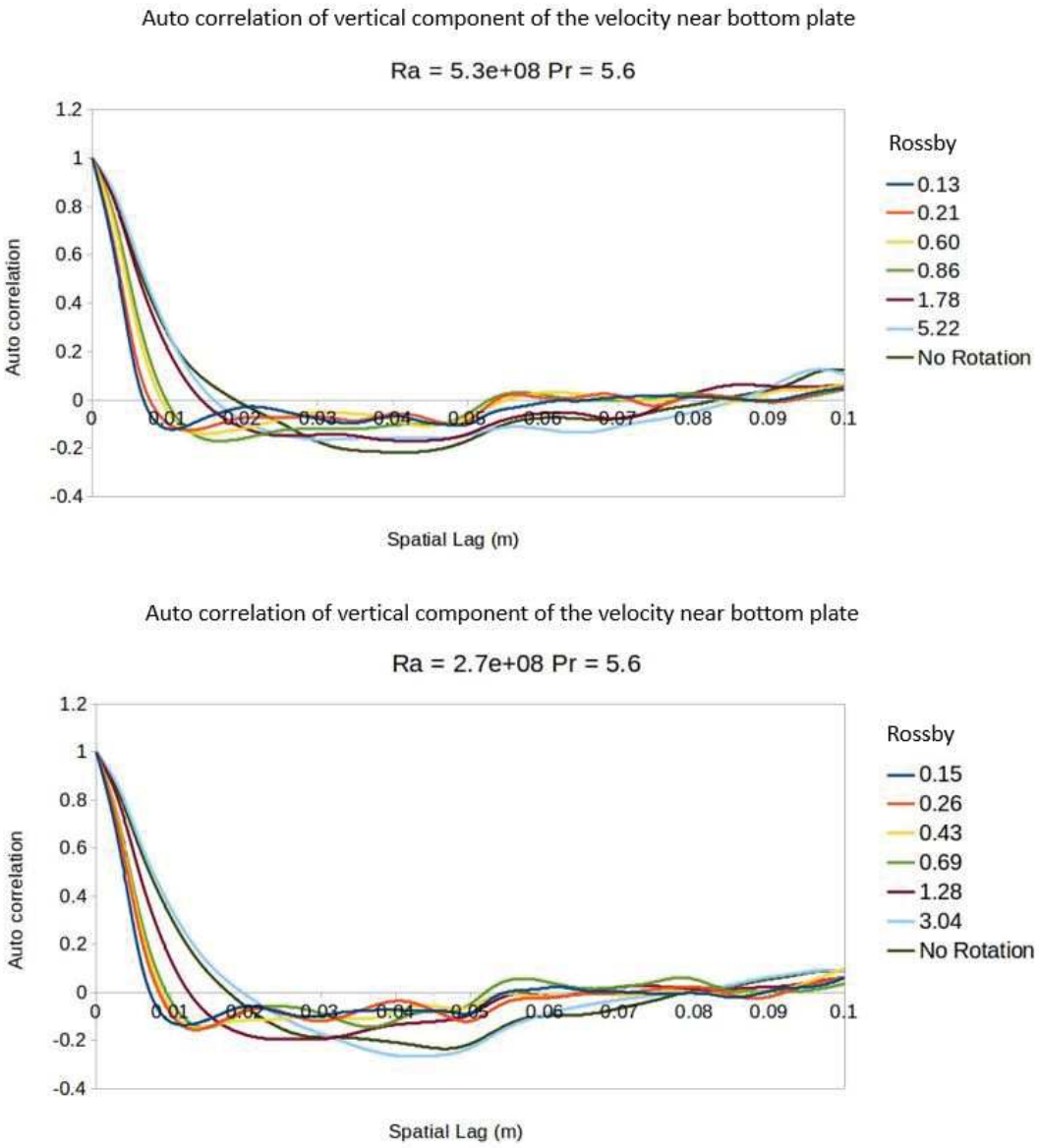


FIGURE 3.20: Auto correlation of vertical component of the velocity near bottom plate at Ra = 5.3e+08 (top) and 2.7e+08 (bottom) for different Rossby numbers

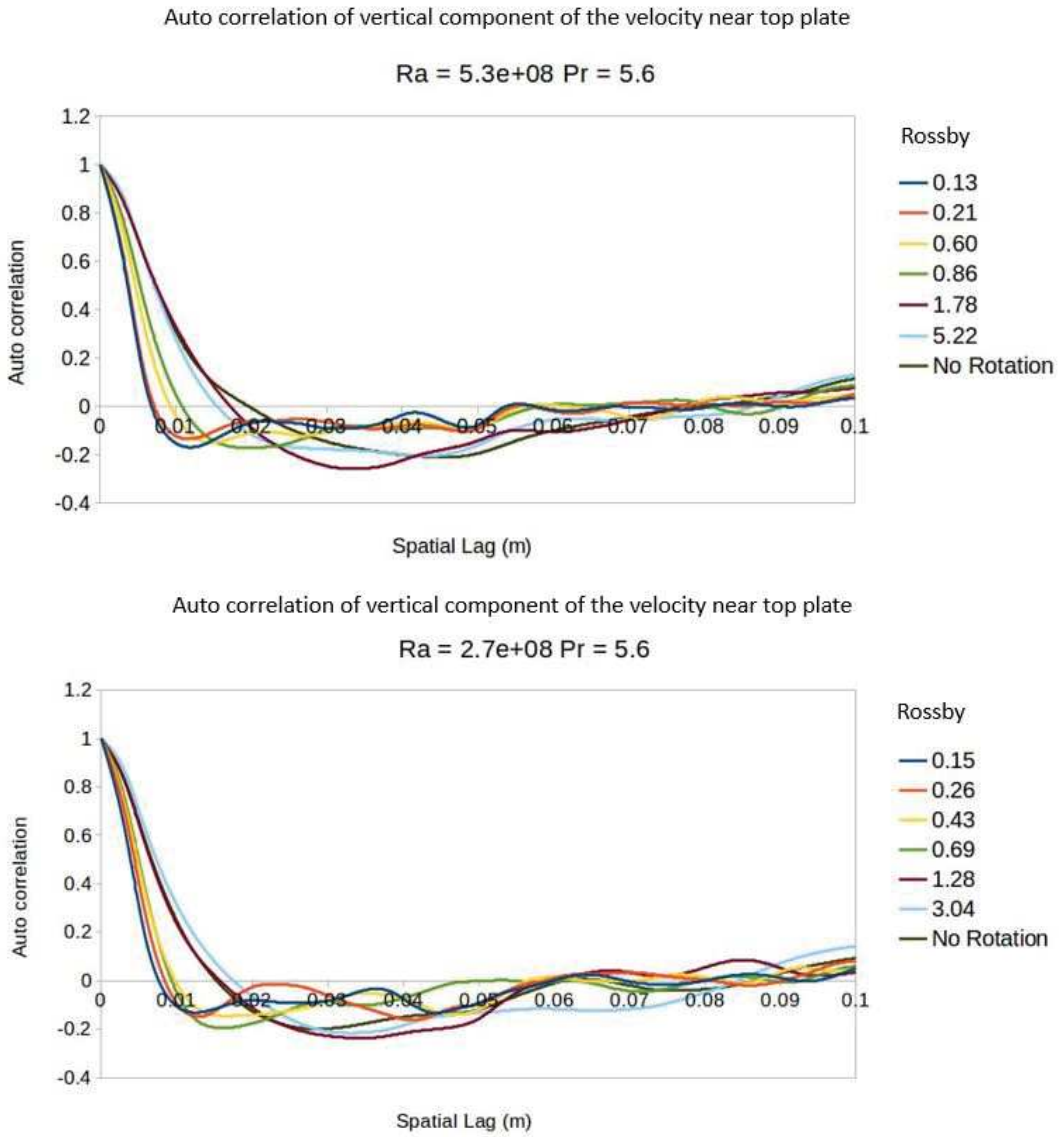


FIGURE 3.21: Auto correlation of vertical component of the velocity near the top plate at Ra = 5.3e+08 (top) and 2.7e+08 (bottom) for different Rossby numbers

When vertical component of the velocity is correlated along the horizontal direction, the maximum negative correlation occurs when upward rising vortex column encounters a downward falling vortex column and viceversa. If we consider that, in the vertical plane containing the axis of symmetry of the cell, columns are alternatively going upward or downward, the location of first minimum can define the width of the columns. Figure 3.20, 3.21 show spatial auto-correlation of vertical component of the velocity near the top plate at various Rossby numbers for a given Rayleigh value 5.3e+08 and 2.7e+08. From the images, it can be noticed that the auto-correlation curve has the periodicity equal to the cell width for Rossby number > 1 . There is

a significant change in the slope of the negatively correlating curve near the transition. The vertical component of the velocity is negatively correlated with a steeper slope for Rossby number < 1. The maximum negative correlation occurs at larger spacial lag for the rotation unaffected regime compared to rotation affected regime. Also the auto correlation curves look similar near the bottom and top plates.

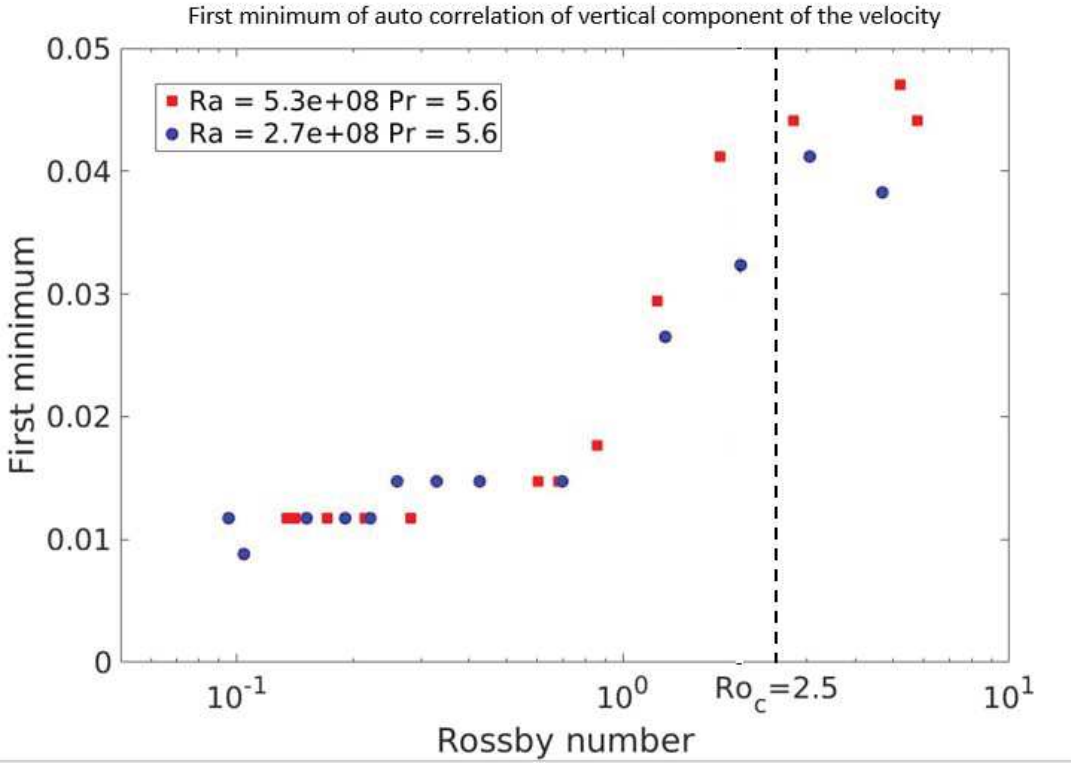


FIGURE 3.22: First Minimum of auto correlation curves plot at the bottom 5% of the cell height for Ra = 5.3e+08 and 2.7e+08.

In the rotation dominated regime, vertical columns are present (Rossby number < 1) , the vertical component of the velocity spatial auto-correlation plots indicate periodicity. The maximum negative correlation occurs at smaller space lag as rotation rate increases (Rossby number decreases). This is due to the fact that at faster rotation, more columns are forming and the width of the columns decreases. This can be verified by plotting first minimum of the auto-correlation curve. Figure 3.22 shows the variation of first minimum with Rossby number. The first minimum is taken as the correlation parameter that defines the width of columns. It can be noticed that the first minimum decreases with decreasing Rossby number. Hence,the width of columns decrease with increasing rotation.

The value of the first minimum at the lowest Rossby number is approximately equal for all Rayleigh. This suggest that below a specific rotational speed, the width of columns does not change. There may be a limit on the minimum size of vertical columns that can be formed inside RBC cell depending on the size of the cell. For a fixed cell size, there seems to be a limit on the maximum number of vortices that can form and beyond this the vortices may not breakdown any more into smaller vortices by increasing the rotation rate. Vortex vortex interactions decrease at higher rotations and hence may stall the breakdown of vortices. More experimental study is required to confirm this behavior of the vortex columns.

## 3.7 Velocity Fluctuation Field

Velocity fluctuation represented by root mean square velocity is a measure of turbulent intensity. Velocity fluctuation is defined as

$$V_{f_i} = \sqrt{\langle (V_i - \overline{V_i})^2 \rangle} \tag{3.3}$$

where $\overline{V_i}$ is the time averaged velocity in 'i' direction. $\langle ... \rangle$ indicates time average. The velocity fluctuation flow field is shown in figure 3.23 at various Rossby numbers and constant Rayleigh 2.7e+08.

In the rotation unaffected regime, the velocity fluctuations increase with decreasing Rossby number, from the non rotating case until entering in the rotation affected regime. After transition, in the rotation dominated regime, the fluctuations decrease with decreasing Rossby number. Fluctuations develop initially near the bottom and top plate (see figure 3.23). Ekman pumping induces higher fluctuation during the development of column propagating from the bottom and top plates toward the center of the cell.

In the rotation unaffected regime, the fluctuations of the vertical component of the velocity are higher near the sidewalls where the upward rising and downward falling plumes are present. The vertical velocity fluctuation are smaller near the center of the cell. The vertical velocity fluctuations are increasing in the center of the cell near the transition. Below the critical Rossby number, the vertical velocity fluctuations are decreasing. At fast rotation, the upward rising vertical columns and downward falling vertical columns are adjacent to each other. The vertical velocity fluctuation are higher in the region where these columns interact. Our measurement time (67 seconds)

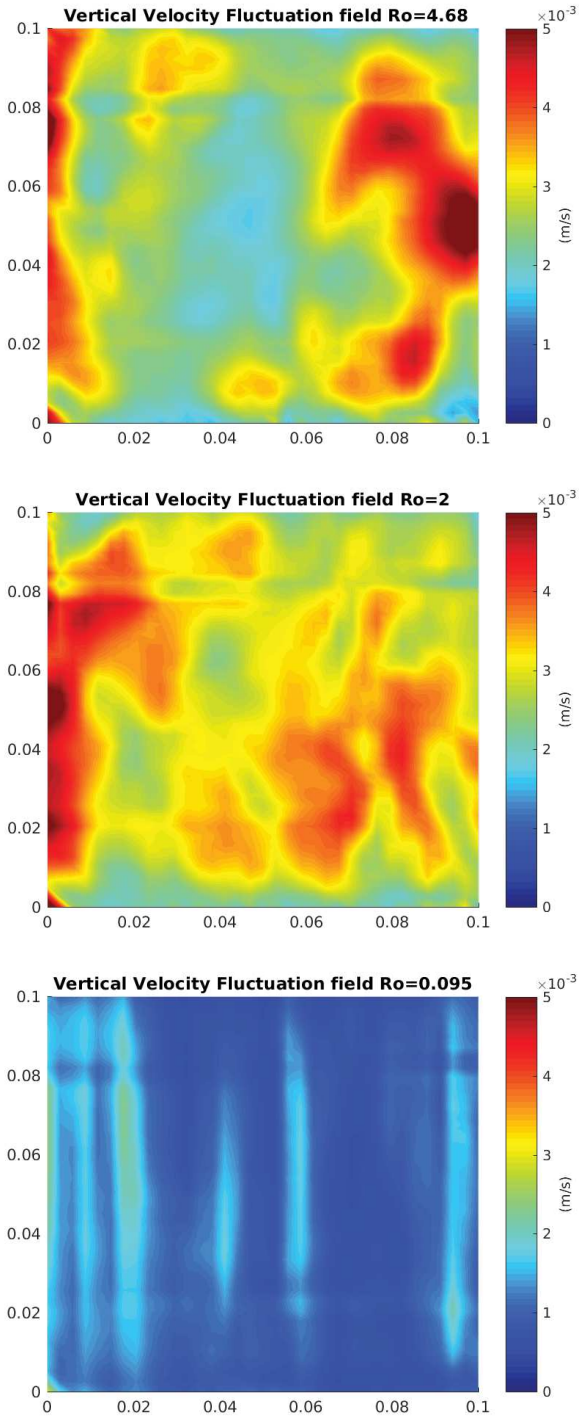


FIGURE 3.23: Vertical velocity fluctuation at Ro = 4.68 (top), Ro = 2 (middle) and Ro = 0.1 (bottom) for Ra = 2.7e+08.

is too small to avoid bias coming from the slow moving columns. Hence, the vertical velocity fluctuation contour at fast rotation shows thin vertical stripes extending from top plate to the bottom plate, indicating the regions where columns interact. The interaction between columns decreases with increasing rotation. Hence the vertical velocity fluctuation also decreases

with decreasing Rossby values in the rotation affected and rotation dominated regime.

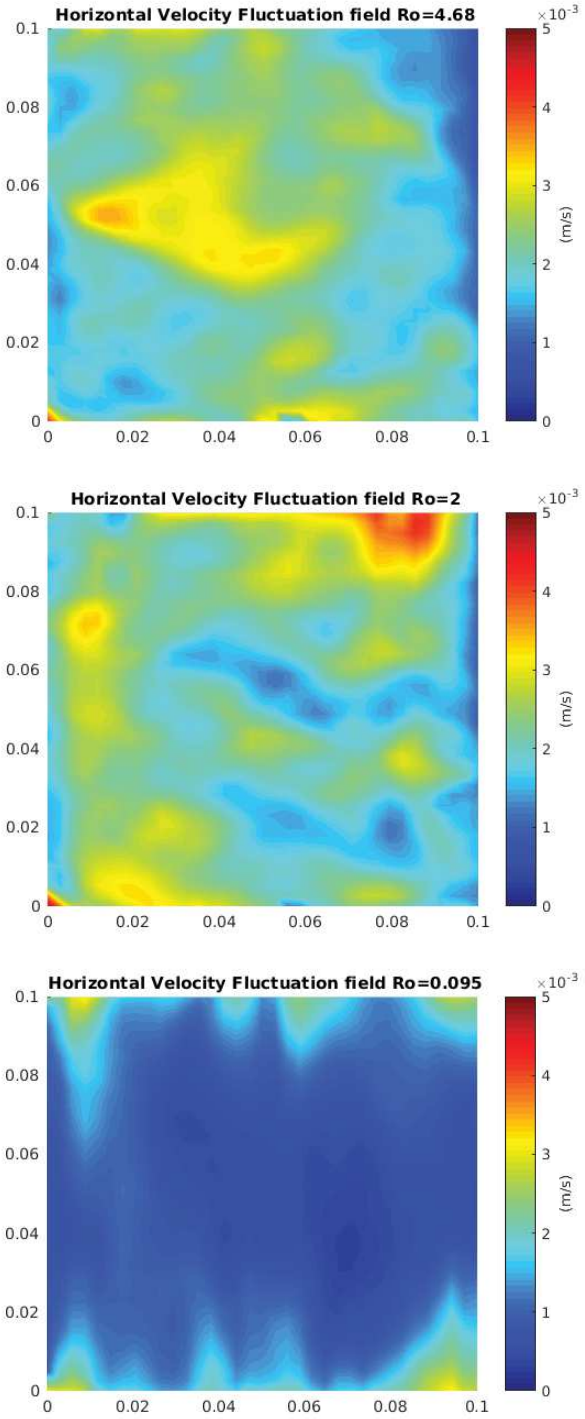


FIGURE 3.24: Horizontal velocity fluctuation at Ro = 4.68 (top), Ro = 2 (middle) and Ro = 0.1 (bottom) for Ra = 2.7e+08..

In the rotation unaffected regime, the fluctuation of the horizontal component of the velocity are higher near the top and bottom plates due to the presence of numerous plumes emerging from one end of the plate to the other. The fluctuations of the horizontal component of the velocity increase near the top and bottom plates as Rossby number decreases (see figure 3.24 ). This is due to the development of vorticity in the boundary layers. In the center of the cell, the fluctuations of the horizontal component of the velocity are increasing with decreasing Rossby number upto the transition from rotation unaffected regime to the rotation affected regime. Beyond this transition, the fluctuations of the horizontal component of the velocity are decreasing with decreasing Rossby number or increasing rotation rate. For a better understanding of these contours, fluctuation of the horizontal component of the velocity is averaged at each height and plotted for various Rossby number values (see figure 3.25 ).

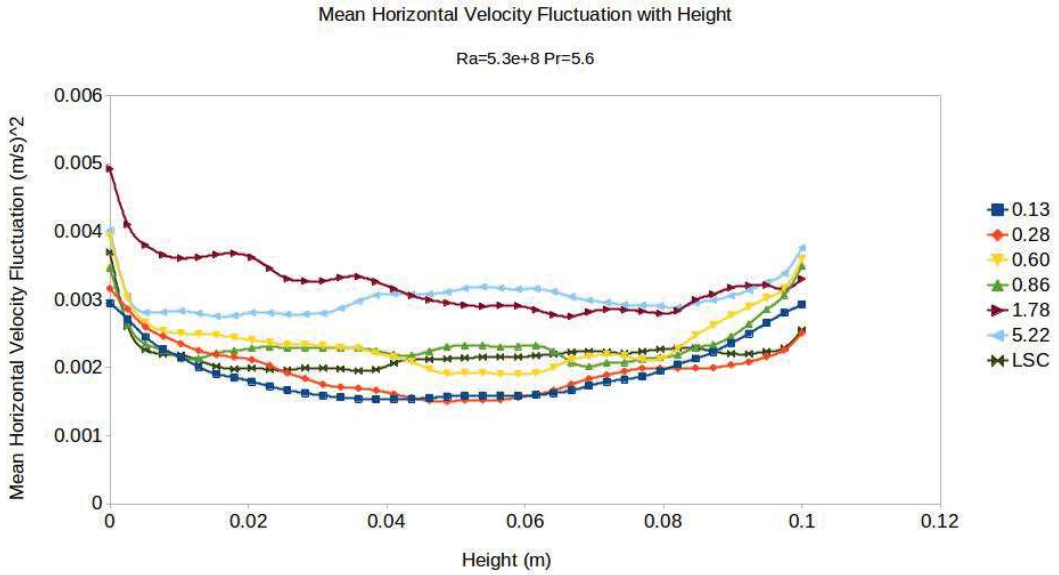


FIGURE 3.25: Mean horizontal velocity fluctuation at various heights for Ra = 5.3e+08 for different Rossby numbers.

From the plot 3.25 we can understand that the fluctuations of the horizontal component of the velocity are higher near the side walls compared to the center of the cell. Also, the fluctuations of the horizontal component of the velocity are higher near the critical Rossby number $\approx 2.5$.

To further quantify these observations, velocity fluctuations are compared at three different heights (at the mid height of the cell and at approximately 5%

away from the top and bottom plates). The normalized velocity fluctuations with respect to Rossby number are plotted in figure 3.26.

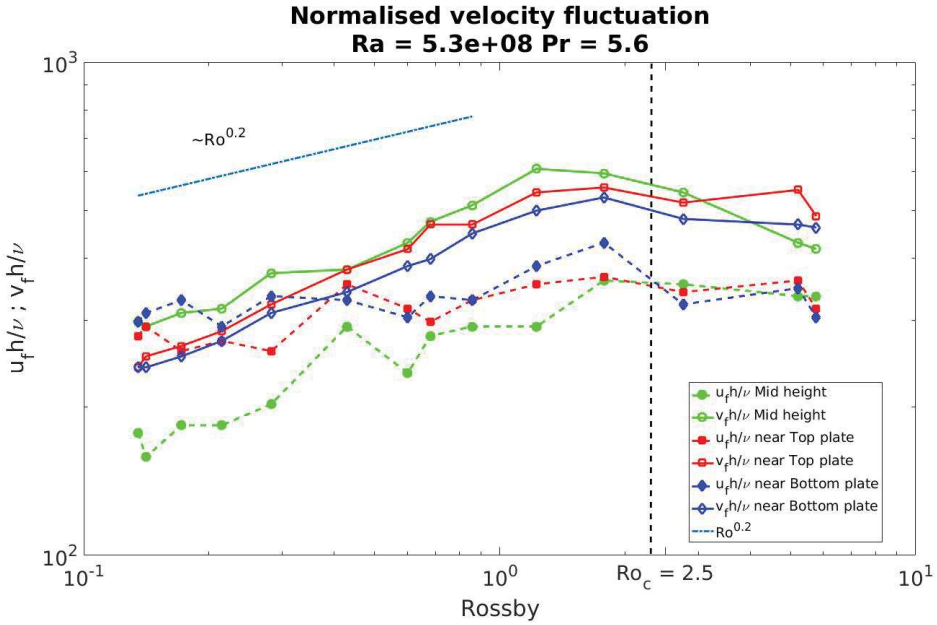


FIGURE 3.26: Normalized horizontal fluctuation with Rossby at Ra = 5.3e+08

From the graph we can observe that the fluctuations have a scaling of around $Ro^{0.2}$ in the regime of rotation affected and rotation dominated regime. The scaling is in agreement with Kunnen et al., 2010 and (Rajaei et al., 2018) results. The fluctuations show a strong anisotropy: fluctuations of the vertical component of the velocity are higher than the fluctuations of the horizontal component of the velocity at the mid height and near top and bottom plates. The vorticity developed in the boundary layers contributes to the fluctuations in the horizontal component of velocity. As rotation increases, the turbulence is suppressed and this causes the fluctuation in the horizontal component of velocity to decrease. Hence, the decrease in the net fluctuations of the horizontal component of velocity are not as strong as the decrease in the fluctuation of the vertical component of the velocity (Rajaei et al., 2018).

The fluctuations are also non-homogeneous : there is significant difference in the fluctuation of the horizontal component of the velocity at mid height of the cell compared to the fluctuation near the top and bottom plates. This may be caused by the fact that the vorticity is stronger near the boundary layers. At the mid height the vorticity decreases and columns spin in the opposite direction. Hence, contribution to the fluctuation of the horizontal component of the velocity is higher near the top and bottom plates. Fluctuations of the

horizontal component of the velocity are decreasing at a faster rate near the center of the cell. The change in vorticity direction near the center explains the slight increase in the fluctuation of the vertical component of the velocity at the mid height, in comparison to the fluctuation of the vertical component of the velocity near the top and bottom plates.

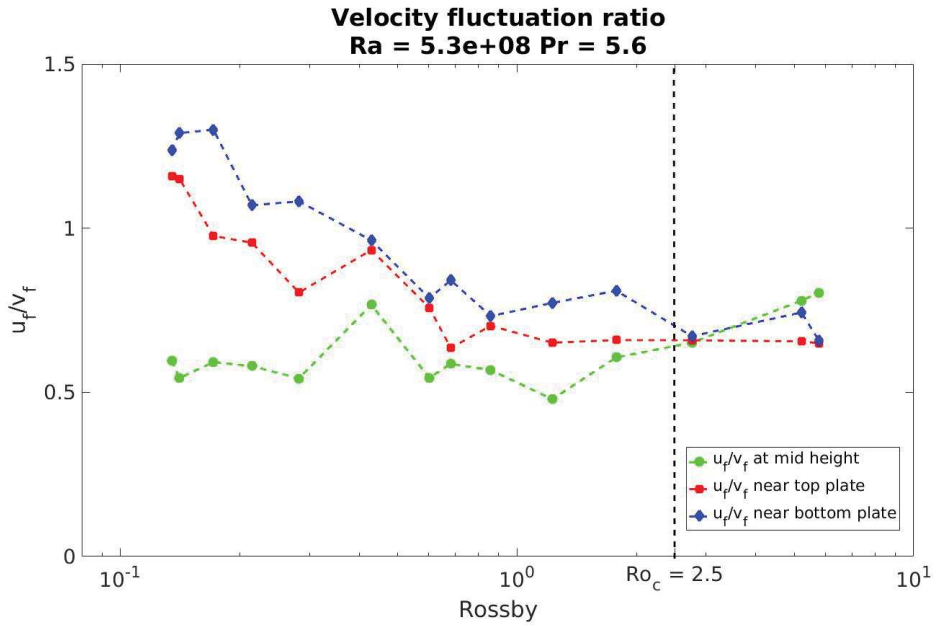


FIGURE 3.27: Ratio of horizontal and vertical fluctuation with Rossby at Ra = 5.3e+08.

An inverse anisotropy ratio is defined using the velocity fluctuation as $1/RU = u^{rms}/v^{rms}$ (see Rajaei et al., 2018). The fluctuation ratio at various heights coincides near the critical Rossby number $\approx 2.5$. The graph changes slope near the critical Rossby. The fluctuation ratio increases with decreasing Rossby number near the top and bottom plates. This is due to higher fluctuation of the horizontal component of the velocity near the top and bottom plates. The rate of decrease in vertical velocity fluctuation is stronger than the rate of decrease of horizontal velocity fluctuation near the top and bottom plates. The fluctuation ratio is not varying much in the mid height of RBC cell. At the mid height, the vorticity is minimum and columns change the direction of spin. Hence the rate of decrease in both horizontal and vertical velocity fluctuations is approximately similar.

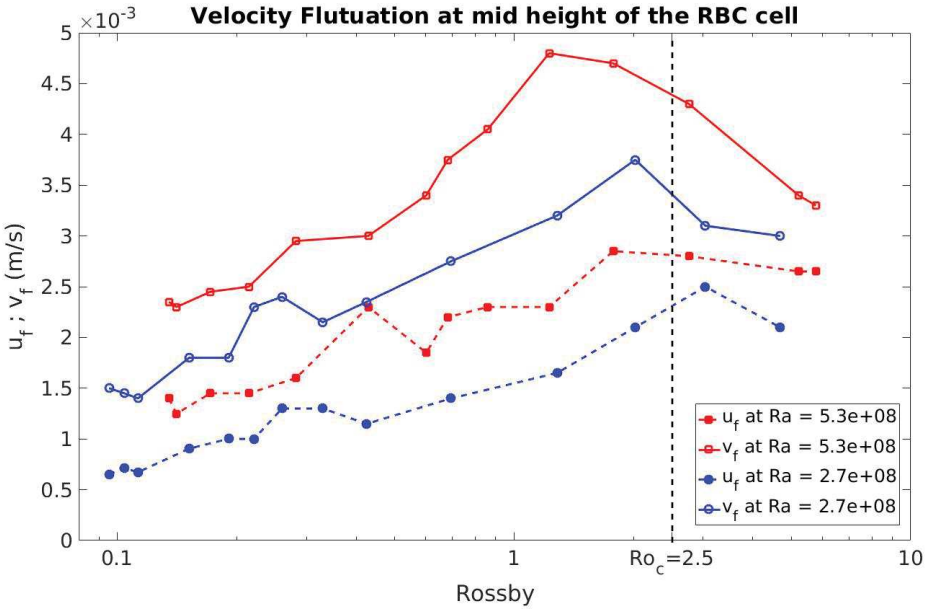


FIGURE 3.28: Horizontal and vertical velocity fluctuations at mid height for Ra = 5.3e+08 and 2.7e+08

Figure 3.28 shows the velocity fluctuations at mid height of the cell for different Rayleigh values. At both Rayleigh values, the vertical velocity fluctuations are higher than the horizontal velocity fluctuations. Fluctuations are also higher near the transition from rotation unaffected regime to the rotation affected and rotation regime. The fluctuations increase in magnitude with an increase in Rayleigh number values as the turbulence increases with increasing Rayleigh number.

## 3.8 Onset of convection

To study the onset of convection in rotating Rayleigh Bénard convection, we conducted experiments at a mean temperature of 40 degrees for a constant rotation rate of 2.7 rad/s and at various Rayleigh numbers. The onset of convection is given by Chandrasekhar, 1961 as $Ra_c = 8.6956Ek^{4/3}$ . In our experimental conditions, the onset of convection according to Chandrasekhar's formula is at Ra = 3.1e+07. Figure 3.29 shows the onset of convection at various Rayleigh numbers and at constant rotation rate of 2.7 rad/s. In the figure the columns are begining to form at Rayleigh number of 8.2e+07 and develop more and more as Rayleigh number increases.

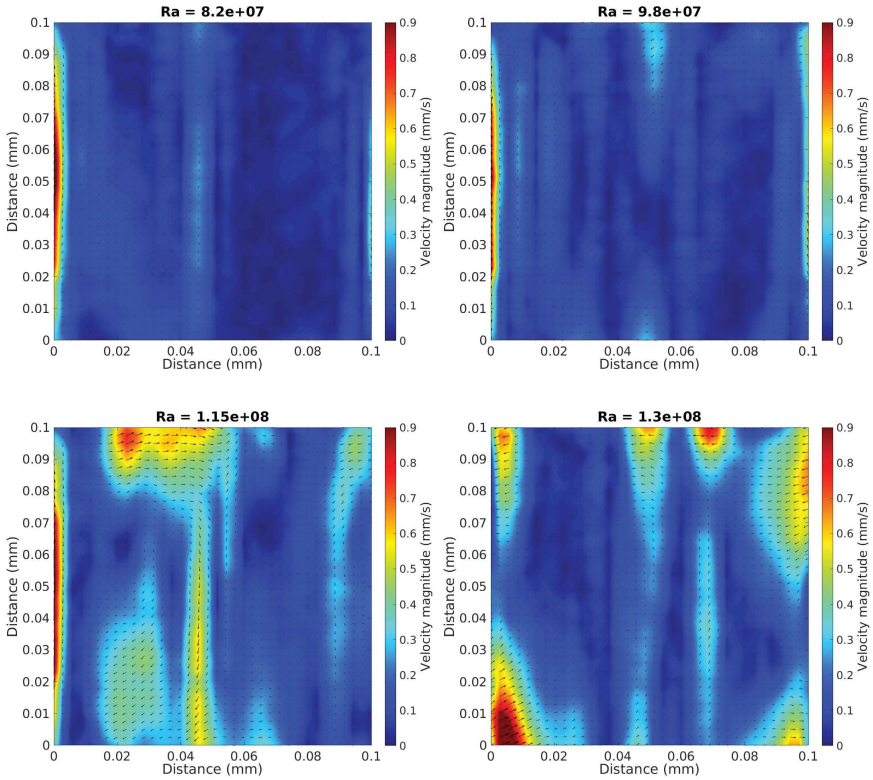


FIGURE 3.29: Mean velocity flow field at a rotation rate of 2.7 rad/s and for Ra = 8.2e+07, 9.84e+07, 1.15e+08 and 1.3e+08

The fluid flow noticed at the sidewalls in the figure 3.29 at low Rayleigh numbers is caused by the lack of insulation of the sidewalls in our experimental setup. The columns are well formed at Rayeigh number > 9.84e+07. The mean vertical velocity is plotted at various Rayleigh numbers in the figure 3.30.

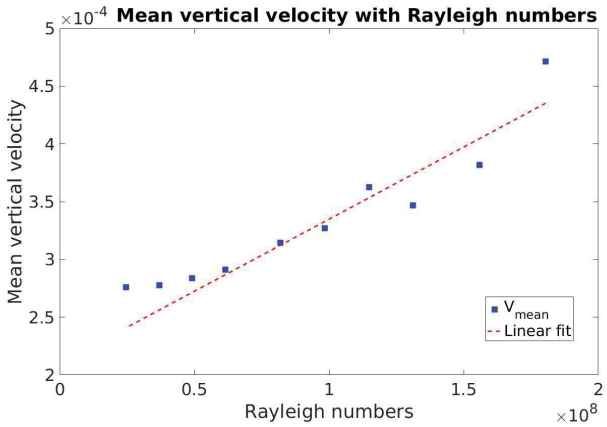


FIGURE 3.30: Mean vertical velocity at various Rayleigh numbers and at a rotation rate of 2.7 rad/s

From the plot we can observe that the mean velocity is constant until Ra = 3.6e+7 which is close to the Chandrasekhar's critical Rayleigh number = 3.1e+07. The slope changes for Ra > 3.6e+07. The mean vertical velocity increases almost linearly with increasing Rayleigh numbers. To be more accurate, further experiments are required to study the onset of convection at various Rossby numbers and Rayleigh numbers and especially focusing near the convective onset Ra = 3.1e+07.

## 3.9 Conclusion

The velocity flow field was studied at various Rossby number and Rayleigh numbers using PIV experimental technique. In the rotation unaffected regime, large scale circulation is the dominant flow structure. For Ro < 1.2 the flow field changes from large scale circulation to the vertical columns due to vorticity induced by Ekman pumping . The strength of large scale circulation increases with increasing rotation rate in the rotation unaffected regime. In the rotation affected regime, the horizontal velocity is out of phase and vertical velocity is in phase when we compare the regions near the top and bottom plate. The vorticity of columns decreases as one moves away from the regions near the plate toward the mid height of the cell. Columns rotate in opposite direction in the regions near the top and bottom plates. The direction of rotation changes in the mid way as the columns extend from one plate to the other. This is in agreement with theoretical predictions of Veronis, 1959. The number of columns increases as the rotation speed increases. The width of columns decreases with increase in rotation. Spatial auto correlation of velocity shows periodicity due to the presence of columns in the rotation affected regime. This periodicity is absent in the rotation unaffected regime. Velocity fluctuations show strong anisotropy : vertical velocity fluctuations are higher than horizontal velocity fluctuations. The horizontal velocity fluctuations are higher in the regions near the top and bottom plates compared to the mid height of the cell. The vorticity developed near the boundary layers increases the horizontal fluctuations in the regions near the top and bottom plates. Our experiment results are in agreement with the results of Kunnen et al., 2008 Rajaei et al., 2016. The present work provides additional information on the velocity dynamics in the regions near the bottom plate in comparison to the top plate. Onset of convection is studied at rotation rate of 2.7 rad/s and at various Rayleigh numbers. The mean vertical velocity with respect to Rayleigh numbers changes the slope near Ra > 3.6e+07

which is close to the critical Rayleigh number (Ra = 3.1e+07) for the onset of convection calculated from Chandrasekhar's formula. Mean vertical velocity increases linearly with increasing Rayleigh numbers.

# Chapter 4

# Temperature field in Rayleigh Bénard convection

## 4.1 Introduction

In this chapter, the temperature field is measured in the mid vertical plane of RBC cell, with and without rotation at various Rayleigh and Rossby numbers. The temporal evolution of plumes in the rotation unaffected and rotation affected regimes is studied to understand the dynamics of plumes. It is found that plumes with small tails are found in the rotation unaffected regime of Rayleigh Bénard convection. Plumes form long tails as rotation increases. Long vertical columns /streak structures are formed, extending from the bottom plate to the top plate in the rotation affected regime. The hot and cold vertical columns alternate when viewed in the horizontal direction in the mid vertical plane of RBC cell.

## 4.2 Temperature contours

### 4.2.1 Without rotation

The figure 4.1 shows the temporal evolution of the temperature field in non rotating Rayleigh Bénard convection at Ra = 8.6e+08. Cold plumes (yellow) are falling from the top plate and hot plumes (blue) are rising from the bottom plate. The cold and hot plumes organize themselves into large scale circulation. The plume have the shape of mushroom with short tails. The temperature difference inside the bulk is less than $5^{\circ}C$ even though the temperature difference between the bottom plate and top plate is $30^{\circ}C$. This

confirms that the boundary layers contain most of the temperature gradient. Figure 4.2 shows instantaneous temperature field without rotation at Ra = 2.7e+08. The heat transfer from the plates to the bulk decreases with decreasing Rayleigh number. The number of plumes decreases with decreasing Rayleigh number.

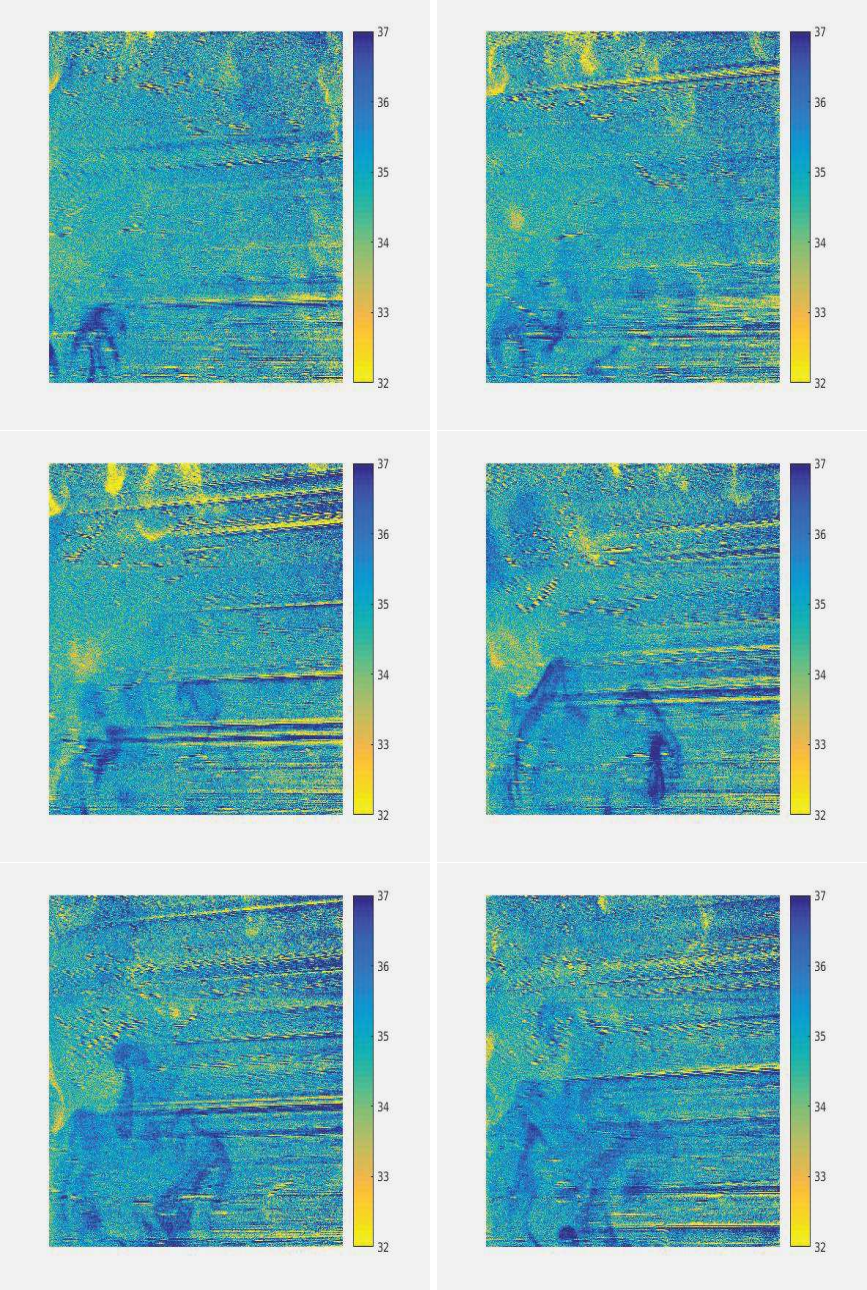


FIGURE 4.1: Instantaneous temperature field without rotation at $\Delta T = 30^{\circ}C$ and Ra = 8.6e+08. Images are 10s apart.

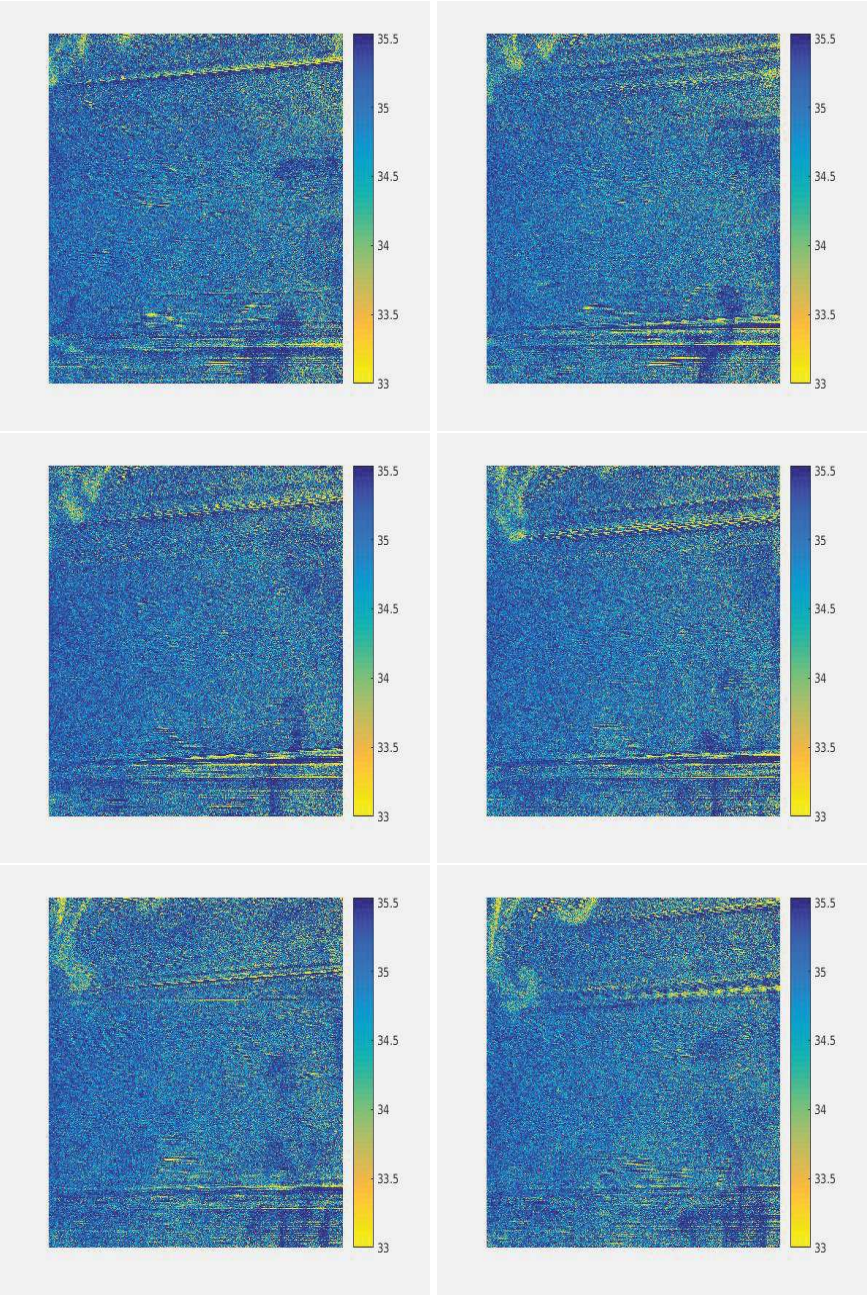


FIGURE 4.2: Instantaneous temperature field without rotation at $\Delta T = 10^{\circ}C$ and Ra = 2.7e+08. Images are 10s apart.

### 4.2.2 With rotation

The hot and cold plumes rising and falling from the bottom and cold plates respectively, form long columns extending from one plate to the other, in the rotation affected regime. The instantaneous temperature fields of Rayleigh Bénard convection under rotation at Ro = 1.9 and Ra = 8.6e+08 is given in figure 4.3. We can notice that the vertical streak like structures form and they swirl as they extend from one plate to the other. This swirling motion is visible in the cold (yellow) plumes in the instantaneous temperature field of figure 4.3. In the rotation affected regime, the vorticity developed in boundary layers, restricts the detachment of the plumes from the boundary layer and hence, the plumes visible in figure 4.3 are forming long tails attached to boundary layers before eventually detaching from the boundary layer.

When the rotation speed is further increased, the number of columns forming inside the cell increases. Figure 4.4 shows the instantaneous temperature contour at Ro = 0.15 and Ra = 8.6e+08. The columns are well formed in figure 4.4 compared to the columns formed in figure 4.3. The hot (blue) and cold (yellow) columns form alternately when viewed in a vertical plane. The hot and cold plumes extend vertically from one plate to the other. The number of columns increase with increase in rotation speed. Figure 4.5 shows the temperature field at Ro = 0.08 and Ra = 2.7e+08. The heat transfer increases with increasing Rayleigh numbers (see figure 4.5 and 4.4). At the lowest Rossby number in the rotation affected regime, the columns are well formed extending from one plate to the other in the vertical direction. The columns decrease in width as the rotation rate is increased.

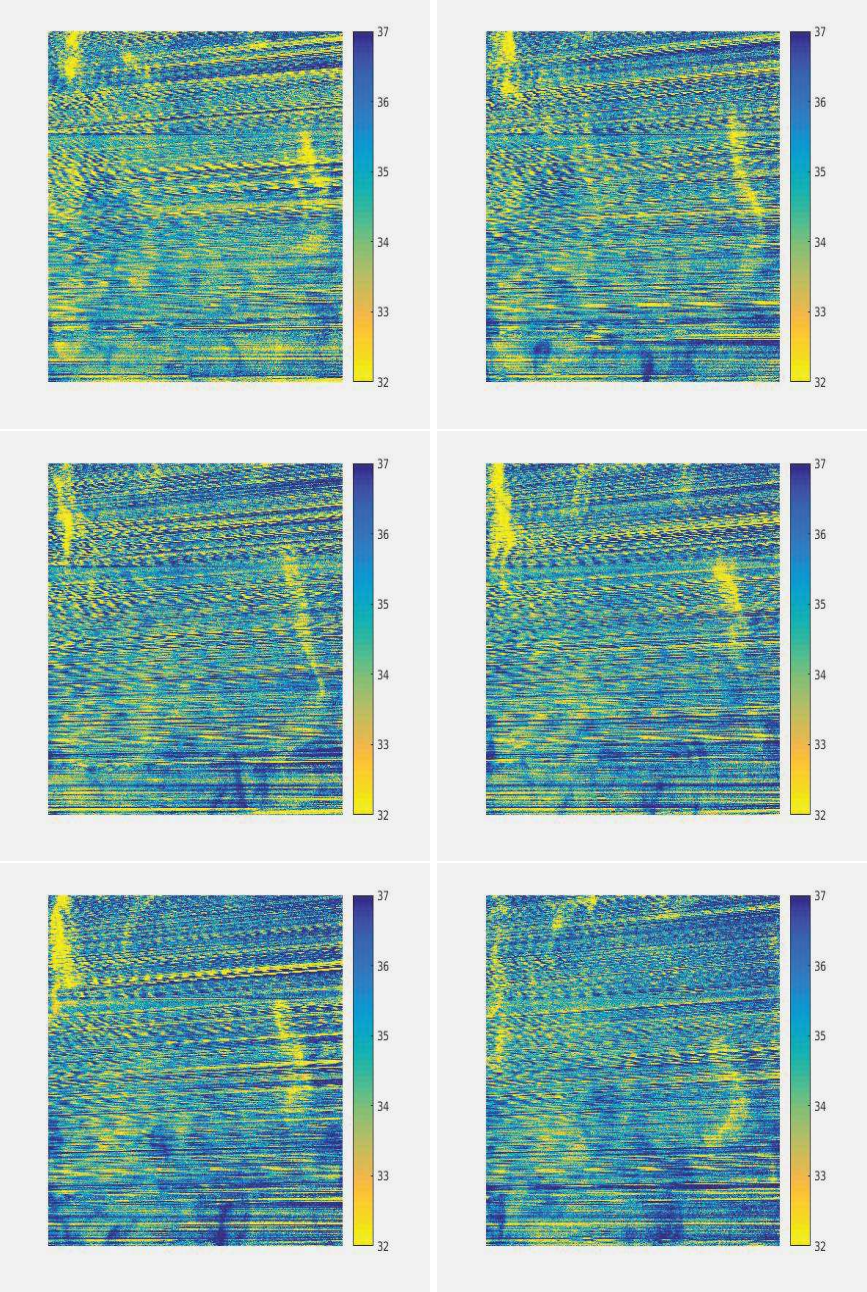


FIGURE 4.3: Instantaneous temperature field at Ro = 1.9, $\Delta T = 30^{\circ}c$ and Ra = 8.6e+08. Images are 10s apart.

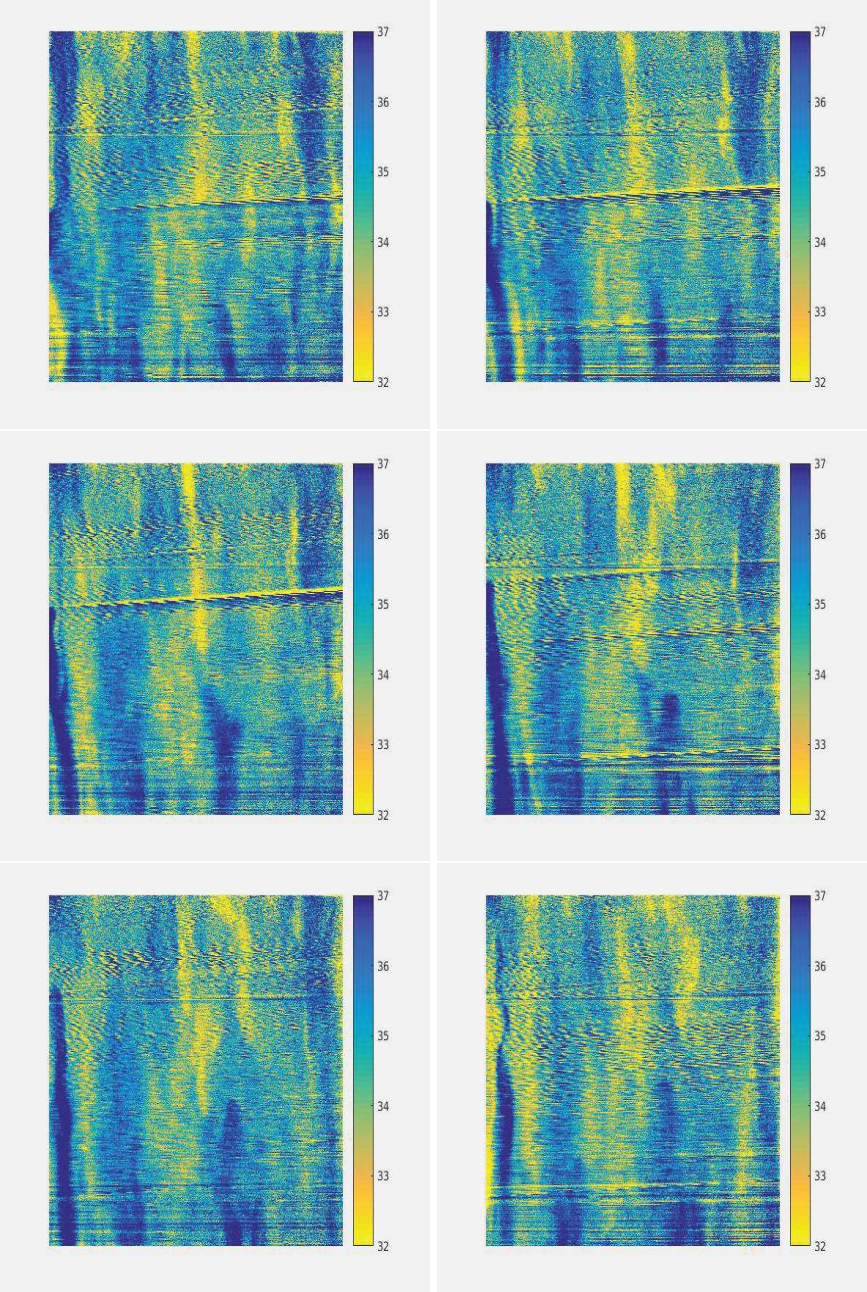


FIGURE 4.4: Instantaneous temperature field at Ro = 0.15, $\Delta T = 30^{\circ}c$ and Ra = 8.6e+08. Images are 10s apart.

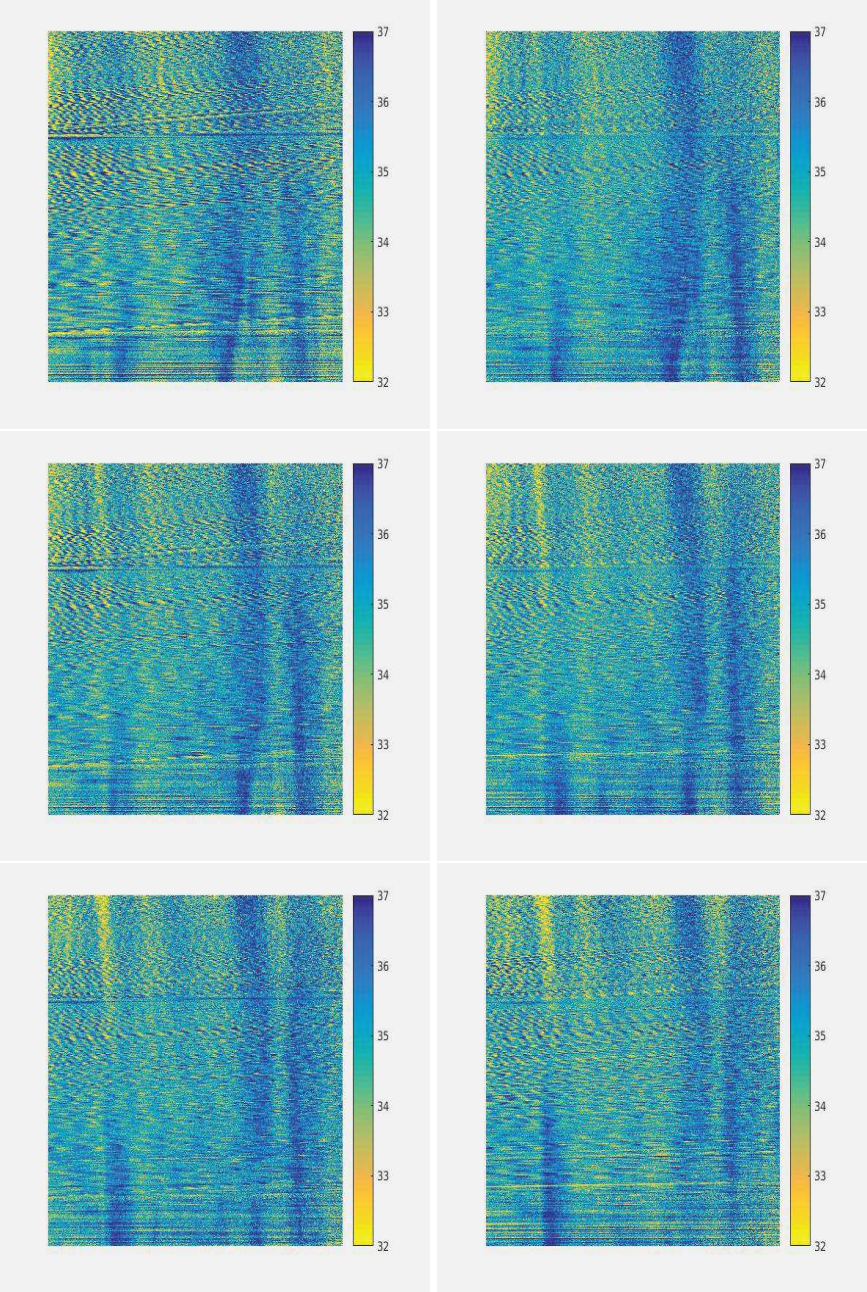


FIGURE 4.5: Instantaneous temperature field at Ro = 0.08 $\Delta T = 10^{\circ}c$ and Ra = 2.7e+08. Images are 10s apart.

## 4.3 Conclusion

Preliminary results of LIF experiments were presented in this chapter. The flow field transition from large scale circulation in rotation unaffected regime to vertical columns in the rotation affected regime is visible in the instantaneous temperature contours. The plumes swirl vertically from one plate to the other in the rotation affected regime. The hot and cold vertical columns are rising and falling alternatively, when viewed in the vertical plane of symmetry of the RBC cell. The number of columns increases with increasing rotation at constant Rayleigh number. Mushroom shape of the plume is not visible under rotation. In the rotation affected regime, at moderate rotation speed, plumes rise and fall with longer tails compared to the plumes in large scale circulation in the rotation unaffected regime. Increase in rotation causes the plumes to be elongated vertically. As the Ekman vorticity in the boundary layers becomes stronger in the rotation affected regime, the plumes are restricted to detach from the boundary layer and hence form long tails attached to boundary layers.

We have investigated different dyes such as Fluroscent di sodium, Keton Red, Rhodamine 560, Sulphorodhamine..etc at different concentrations. The sensitivity of the dye combination of Rhodamine 560 and Keton Red with concentration of $10^{-5} mol/l$ and $10^{-6} mol/l$ respectively, is found to be best suited in our experimental conditions, to measure the temperature field in Rayleigh Bénard convection. The diffraction lines are not removed successfully. This can be improved by using fine grid to calibrate the transformation required to divide the respective images of the two dyes.

# Chapter 5

# Path instability of rising bubbles

## 5.1 Abstract

*Above a critical size, bubbles rising in a liquid undergo a first instability in their path, followed by several others. Small bubbles rise in straight path whereas, beyond critical size of bubbles, they oscillate. The Bond number (ratio of buoyancy forces to surface tension) and the Galileo number (ratio of gravitational force to viscous force) are the parameters allowing us to define the marginal stability curve and the different instability domains of rising bubbles. Until recently, it was believed that the wake behind the bubble is solely responsible for the path instability (Magnaudet et al., 2007). But a recent study has shown that the path instability does not solely result from a wake instability (Cano-Lozano et al., 2013). The deformation of the bubble also plays an important role in the determining of the threshold of transition from a straight to an oscillatory path (Zhou et al., 2017) . As far as marginal stability curve is concerned there is no general agreement in the existing literature. For this reason, an experimental investigation is necessary to bring new reliable data. In the present work, the path instability of a bubble is studied experimentally in deminaralized water and silicon oil of different viscosities (5cst, 10cst, 500cst ) in a square cross section column. A solenoidal valve and a pressurized tank are used to inject bubbles of various sizes in the bottom of the column. In our studies, we have observed the transition from straight path to various flow regimes such as helical or zig-zag path. Our experimental results allowed us to obtain three points of the marginal stability curve. In the case of water and 5cst silicon oil, a very good agreement with numerical results of Zhou et al., 2017 is obtained. Our observation yield a lower critical Galileo number for the 10cst silicon oil than numerically predicted. The experimental results show a parabolic increase of the amplitude of oscillation with $\sqrt{Ga}$, characteristic of a super critical Hopf bifurcation. The non dimensional frequency of oscillation is also in agreement with numerical simulation of Zhou et al., 2017 .*

## 5.2 Introduction

Bubble rising inside a liquid is an old and intriguing research topic that has caught the interest of researchers since centuries. This seemingly simple problem poses many interesting questions that are not yet completely understood. Bubble dynamics is present in many natural phenomena like aerosol transfer from sea, oxygen dissolution in lakes and in industrial applications like bubble column reactors, petroleum industry, multi phase heat exchangers, nuclear reactor cooling system and many other. The path and shape of a bubble rising in a fluid, change depending on the gravitational force, type of fluids involved and the properties of the interface between the fluids. One of the earliest research on bubble dynamics was conducted by Leonardo Da Vinci. He states in his book the Codex Leicester : "The air which is submerged together in water returns to the air, penetrating water in a sinuous movement...Every impetuous movement bends towards the less resistance as it flies from the greater".

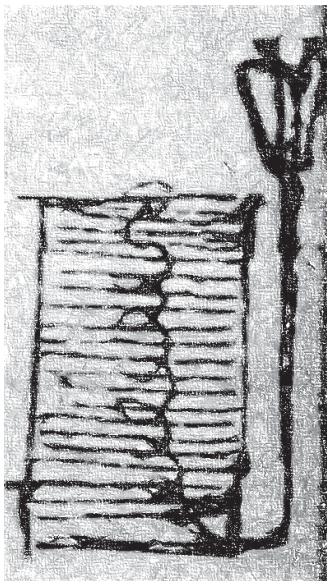

FIGURE 5.1: Bubble oscillation sketch by Leonardo Da Vinci from his book The Codex Leicester

These remarks of Leonardo Da Vinci were futher explained in detail by Ohl et al., 2003. Considering an air bubble immersed inside water, since the density of air is less than the density of water, the air cannot remain under water and rises upward naturally until it reaches the surface. Water which is heavy, exerts force around the lighter air bubble. These hydrodynamic forces coupled with the multi degree freedom of bubbles, create interesting shapes and path as it rises in the liquid. Especially the dynamics of bubble path is different

from that of rigid bodies where no slip condition is observed. It is known that very small bubbles rise in rectilinear path. Whereas, beyond critical size the bubbles start to oscillate and form various paths such as planar zigzag, sprial or helical path Haberman et al., 1953. Extensive research has been carried out to define the instability threshold at which the transition from rectilinear to the oscillatory path arises. Earlier research experiments used non purified water and hence the bubble was subject to contamination ( Hartunian et al., 1957 Lunde et al., 1998). The shear free condition of bubble surface is no longer valid under the effect of surface contamination. It transforms the nearly total stress free conditions to no slip conditions which causes the bubble to oscillate at lower thresholds than expected. Duineveld, 1995 studied the effect of contamination and conducted experiments in hyper clean water at high Reynolds numbers. It was believed that the wake behind the bubble was solely responsible for the path instability of the rising bubble. Hence, many experiments were carried out to visualize the wake behind the rising bubbles by using dyes by Lunde et al., 1998, particle image velocimetry by Zenit et al., 2009, laser doppler anemometry by Ellingsen et al., 2001 and thermographic schlieren setup by Vries, 2002 Veldhuis, 2007.

Since experiments can suffer from surface contamination and other intrusive effects, with the advancement of numerical codes, path instability has been studied numerically where contamination by surfactants can be fully avoided. The bubble shape deformation during its path, changes the hydrodynamic forces acting on the bubble. To simplify this problem, initial numerical analysis focused on bubble with fixed shapes (Mougin et al., 2001 Magnaudet et al., 2007) and recently on fixed realistic bubble shapes by Cano-Lozano et al., 2013. Zhou et al., 2017 conducted numerical analysis on bubbles without fixed shape allowing the deformable bubble to affect the instability of bubble shape and path.

### 5.2.1 Mathematical Formulation

Assume that the bubble has a constant volume 'V' and an equivalent diameter 'd' with a free surface of constant surface tension $'\sigma'$. The bubble is rising in a liquid of density $'\rho'$ and kinematic viscosity $'\nu'$. The motion of air inside the bubble is neglected due to the low density and viscosity of air compared to the density and viscosity of the surrounding liquid. The non dimensional equations of flow inside liquid using 'd', equivalent diameter defined as the

diameter of a sphere of volume V, as length scale and $U_g = \sqrt{gd}$ as velocity scale and $\rho U_g^2$ as pressure scale are expressed as

$$\frac{\partial \mathbf{v}}{\partial t} + [(\mathbf{v} - \mathbf{u}) \cdot \nabla]\mathbf{v} + \nabla p - \nabla \cdot (\frac{2}{Ga}\tau) = 0 \tag{5.1}$$

and

$$\nabla \cdot \mathbf{v} = 0 \tag{5.2}$$

where as $\tau = 1/2, (\nabla \mathbf{v} + \nabla \mathbf{v}^T)$

Boundary conditions at the bubble surface (considered as a free surface):

$$-p\mathbf{n} + \frac{2}{Ga}\tau \cdot \mathbf{n} - \frac{1}{Bo}\kappa \mathbf{n} = -(p_b - z)\mathbf{n} \tag{5.3}$$

where $\kappa$ stands for curvature.

### 5.2.2 Non Dimensional Numbers

To characterize the dynamics of bubble, various researchers used different non dimensional numbers such as Reynolds number $(Re = Ud/\nu)$, aspect ratio $(\chi = d_{major}/d_{minor})$ of bubble (Mougin et al., 2001 Magnaudet et al., 2007), Morton number$(Mo = g\mu^4/\rho\sigma^3 = Bo^3/Ga^4)$(Haberman et al., 1953), Eotvos number $(Eo = \rho g R^2/\sigma)$ (Tripathi et al., 2015) and Weber number$(We = \rho U^2 d/\sigma)$(Hartunian et al., 1957)..etc. The Reynolds number may not be an appropriate parameter, since the terminal velocity is the result of bubble dynamics and is not known a priory and, moreover, it is not constant as soon as instability sets in.

Bubbles can be considered as a constant volume of zero density and viscosity enclosed by a variable free surface. In such assumption, two parameters such as Galileo number and Bond number can be used to determine the instability threshold.

**Galileo Number** : Ratio of gravitational force and viscous force.

$$Ga = \frac{\sqrt{gd^3}}{\nu} \tag{5.4}$$

**Bond Number** : Ratio of gravitational force and surface tension force.

$$Bo = \frac{\rho g d^2}{\sigma} \tag{5.5}$$

In this thesis, we use Galileo number and Bond number to define the marginal stability curve and to compare with the numerical results of Zhou et al., 2017.

In most experimental studies found in the literature, the threshold of instability, were found at higher Galileo numbers such as at Ga = 390 by Ellingsen et al., 2001 and Ga > 500 by Veldhuis, 2007. Zenit et al., 2009 Zenit et al., 2008 observed the onset of zigzag trajectory in silicon oil for $Bo = 2$; $Ga = 150$, $Bo = 2.5$; $Ga = 176$, $Bo = 3.2$; $Ga = 85$ and $Bo = 3.9$; $Ga = 99$. In the present work, we have conducted experiments in a large parameter range of $0 < Bo < 20$ and $15 < Ga < 200$ using de-mineralized water and silicon oil of 5cst and 10cst viscosities.

The first numerical simulations were achieved in the non deformable fixed shape bubbles. Figure 5.2 shows the marginal stability curve from studies of Cano-Lozano et al., 2013 using fixed but realistic bubble shapes. Tripathi et al., 2015 also studied the onset of instability on three dimensional bubbles using Volume of Fluid (VOF) method. Their study coarsely covered a large domain of the Eo-Re parameter space and has few points near the instability threshold. Zhou et al., 2017 used linear stability analysis to study the onset of instability accounting for the bubble shape deformation. Although Zhou et al., 2017 and Tripathi et al., 2015 have similar mean trend near to the instability, Zhou et al., 2017 found a non monotonous marginal stability curve. Initially, their instability curve decreases at low bond numbers. After reaching a minimum of $Ga \approx 73$ at $Bo \approx 2$ , the instability curve increases to a maximum of $Ga \approx 100$ at $Bo \approx 8$ before falling again to $Ga \approx 70$ at $Bo \approx 20$ for large Bond numbers see figure 5.2. The curves of Cano-Lozano et al., 2013 and Zhou et al., 2017 are significantly different. It may have been caused by the non deformable bubble in the studies of Cano-Lozano et al., 2013.

### 5.2.3 Objective of present work

It is evident from the figure 5.2 that, a common agreement on the threshold of instability has not been achieved yet. The curves plotted by various researchers are also found to have significant difference especially at very low Bond numbers. Numerical simulations based on fixed grid methods (Cano-Lozano et al., 2013) might not give accurate results considering the thin boundary layer of bubble which changes drastically during the path. The parametric studies they provide are also too sparse to describe a precise instability threshold and establish the marginal stability curve reliably. The

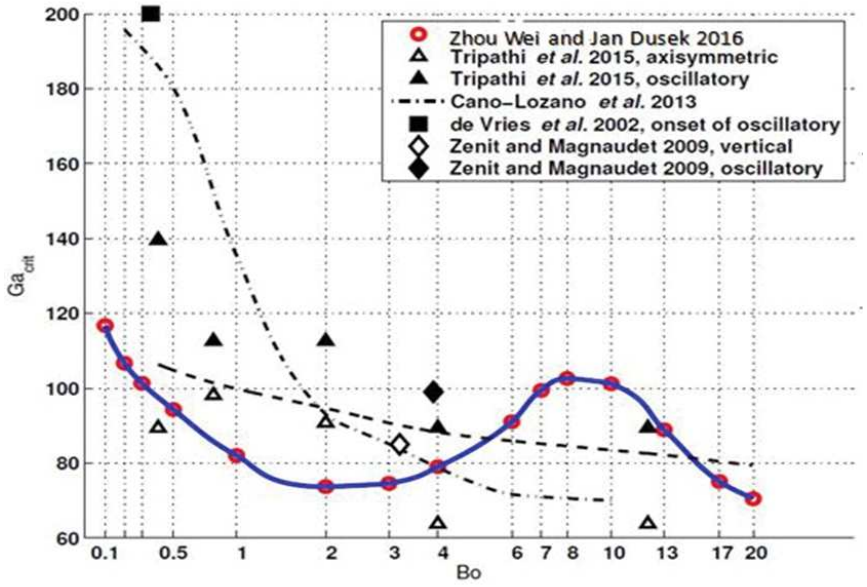


FIGURE 5.2: Marginal Stability curve. Zhou et al., 2017

results of Zhou et al., 2017 predict unexpected shape deformation in the linear regime of instability amplification. Hence experimental investigation of instability in bubble path is needed to set the precise threshold of instability.

Earlier theoretical considerations related the instability of the path of bubbles to the wake instability behind the bubble (Magnaudet et al., 2007). More recently, it appeared (Cano-Lozano et al., 2013) that path instability occurs even in the absence of wake instability even for bubbles with frozen shape. The shape deformation facilitates moreover the instability onset as documented in the numerical study of Zhou et al., 2017. Hence it is important to study the shape oscillations of the bubble near to the instability threshold.

In this work, various shapes of bubbles and their path are studied at different Bond and Galileo numbers. Non polar liquids such as silicon oil of viscosity 5cst and 10cst are used as working fluid to eliminate the effect of possible contamination. Also at very low Bond numbers, demineralized water is used to focus on the instability threshold. Our work focuses on validating the marginal stability curve plot by Zhou et al., 2017 using experimental image visualization technique inspired from Ohl et al., 2003.

## 5.3 Experimental Setup

The experimental setup consists of a tank of square cross section 10cm x 10cm and 50cm height , filled with the working fluid (demineralized water, silicon

oil viscosity 5cst , 10cst). Silicon oil is less subject to contamination by traces of surfactant or polymers which can change the surface tension and the rigidity at the interface. Bubbles of different diameter are injected into the working fluid from below the vessel using needle connected to solenoid valve and a compressed air reservoir. Back Light illumination is used for ombroscopy of the bubbles. Four mirrors are arranged to simultaneously record the bubble path in two orthogonal planes. High speed camera records the bubble motion from the front (500 image/s). Images are post processed using image processing tools in Matlab to reconstruct the path of the bubble.

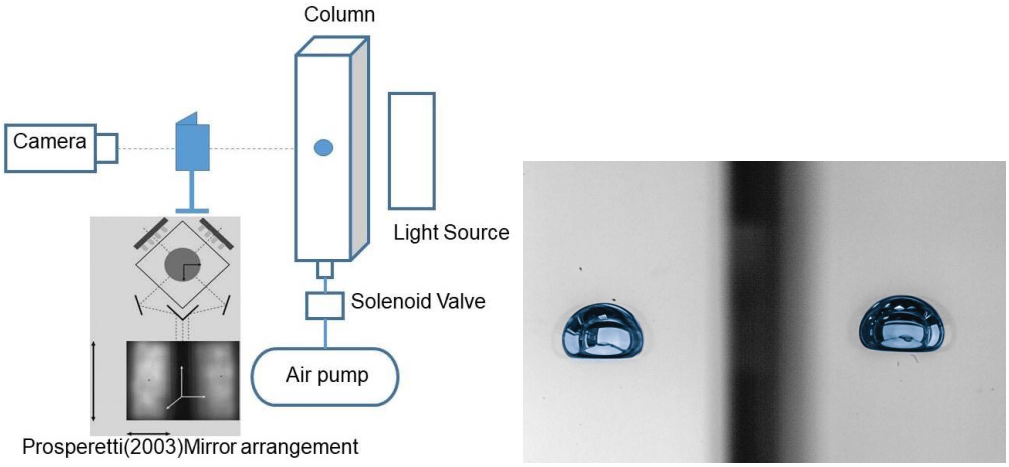


FIGURE 5.3: Experiment setup for 2D visualization of bubble (left) and Bubble image recorded simultaneously in two orthogonal planes.(right)

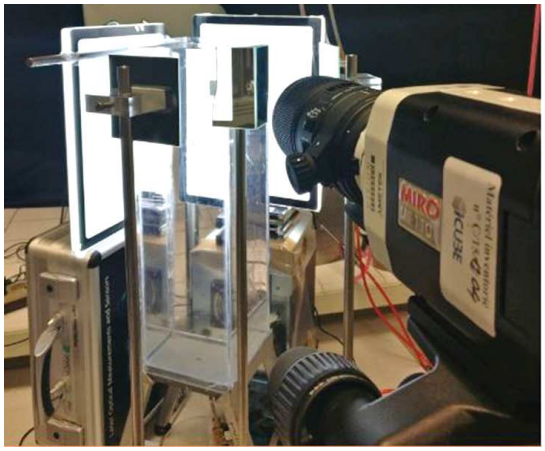

FIGURE 5.4: Experimental Setup

## 5.4 Bubble flow Regimes

Small bubbles are spherical in shape while rising in a liquid. As the bubble diameter increases, the shape of the bubble changes to oblate spheroids, flat front and rounded back. The changes in bubble shape are accounted to the pressure field caused by the viscous effects (Zenit et al., 2008). Small bubbles rise in rectilinear path. Beyond critical size, they begin to oscillate and form a planar zig-zag path. Some studies also observed that the planar zig-zag path of constant amplitude later changes to a spiral path (Mougin et al., 2001). The different regimes observed in the present experiment are commented in the following paragraphs.

### 5.4.1 Rectilinear regime

The bubbles are smaller in size. They follow straight vertical trajectory as they rise in a liquid. The wake has the shape of the two stable counter rotating vortices. The flow around the bubble is axi-symmetric. Extensive study on wake behind the bubble as presented by Cano-Lozano et al., 2013. The present experimental study can not visualize the wake behind the bubble. But, the shape and path of the bubble can be recorded using our experimental setup. Figure 5.5 shows the planar rectilinear path of a bubble of equivalent diameter 3.5 mm in two orthogonal planes( XZ and YZ, where Z is the vertical axis along the trajectory). The Bond number is 5.5 and Galileo number is 60.4. The bubble reached a terminal velocity of 0.185 m/s.

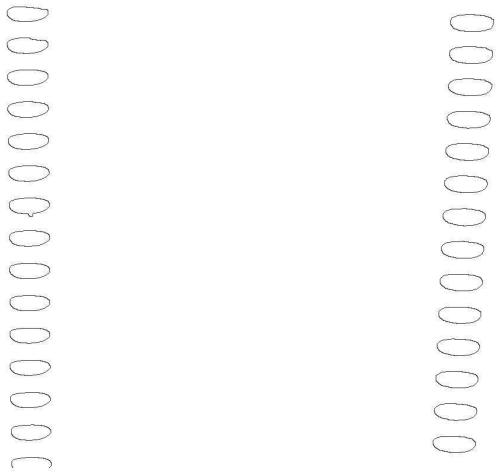

FIGURE 5.5: Bubble rectilinear path in two orthogonal planes XZ (left) YZ(right) at Bo=5.5 and Ga = 60.4 in silicon oil 10cst

The bubble shown in figure 5.5 is in the stable regime below the instability curve. Although the bubble is not spherical, it remains axi-symmetric. The bubble is rising vertically. The slight inclination observed in the YZ plane comes from the misalignment of the mirror and it is not real. The time difference between two successive bubble images is 10ms. The bubble shape does not vary since the Galileo number is very low due to a small diameter of the bubble.

### 5.4.2 Planar Zigzag regime

If the bubble size increases slightly to 3.6 mm, the bubble enters in the oscillation regime. Figure 5.6 shows the planar zigzag path of the bubble at Ga = 64.6 and Bo = 6.1. This bubble is slightly above the critical instability curve. Although oscillation is not evident in the YZ plane, the oscillation has just started and it follows a zig-zag path in XZ plane. The time difference in the successive bubble images is 10ms.

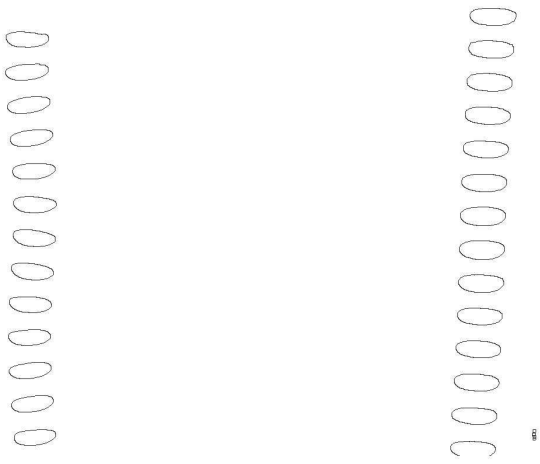

FIGURE 5.6: Bubble planar zigzag trajectory in two orthogonal planes XZ (left) YZ(right) at Bo=6.1 and Ga = 64.6 in silicon oil 10cst.

Initially, the bubble path is vertical with the minor axis parallel to the vertical axis. The bubble experiences a lateral drift perpendicular to the path direction. It can also be observed that the bubble tilts with respect to the vertical direction. The largest inclination occurs at mean horizontal position when the horizontal velocity is the largest (Cano-Lozano et al., 2013). If the shape of the bubble is observed in the YZ plane on the right of figure 5.6, it appears that the bubble minor axis expands and compresses. This indicates that the bubble is tilting in the plane of zig-zag motion. The bubble is rising with

a velocity of 0.19 m/s. Bubble path can be fitted with sinusoidal function $y(t) = Acos(wt + \phi)$. The frequency of oscillation is found to be 5.9 Hz. The path of bubble in XZ, YZ and XY plane is shown in figure 5.7

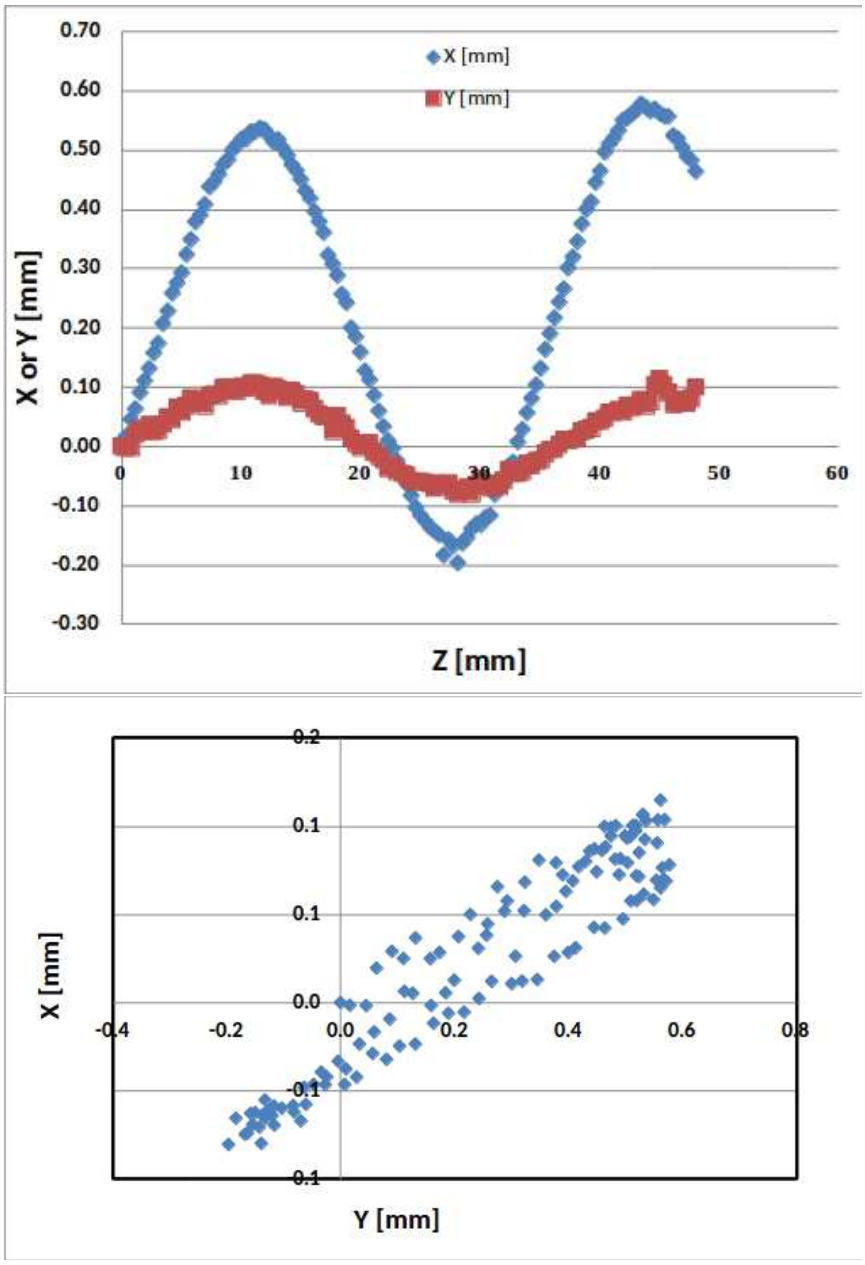


FIGURE 5.7: Planar Zigzag path of bubble in side view of XZ,YZ plane (top) and top view of XY plane (bottom)

Amplitude of oscillation in the XZ plane is higher than the YZ plane as observed in figure 5.6 and figure 5.7. The path of the bubble in the horizontal XY plane shows that the path is nearly perfectly 2D (see figure 5.7).

FIGURE 5.8: Bubble helical path in two orthogonal planes XZ (left) YZ(right) at Bo=10 and Ga = 94 in silicon oil 10cst

### 5.4.3 Helical regime

Further away from instability threshold for large bubbles, we can observe helical regime. In this regime the bubble follows a elliptical spiraling path. After reaching terminal velocity the path looks like a circular helix when observed in 3D. This regime is observed for higher Bond numbers ($Bo \approx 10$). It is characterized by vortices wrap around one another behind the bubble (Cano-Lozano et al., 2013). The path of the bubble of diameter 6.3 mm, Bo = 10 and Ga = 94 is show in figure 5.9.The time difference in successive bubble image is 7 ms. The amplitude of oscillation is high in both XZ and YZ planes. By fitting a sinusoidal, we find the frequency of oscillation as 6.8 Hz. It can also be observed that the bubble shape changes drastically during its path in both the planes.

## 5.5 Marginal Stability Curve

All the experiment points are plotted on the marginal stability curve of Zhou et al., 2017. From the figure 5.10 we can notice that the threshold is in agreement with numerical results for water and silicon oil of 5 cst. For the experiments with Silicon oil 10 cst, we found a lower threshold than the estimated threshold of Zhou et al., 2017. At lower Bond number of $Bo \approx 0.1$, our experimental threshold of water bubbles suggest that the instability is about $Ga \approx 100$ unlike the threshold estimated by Cano-Lozano et al., 2013 which is at $Ga \approx 200$ .

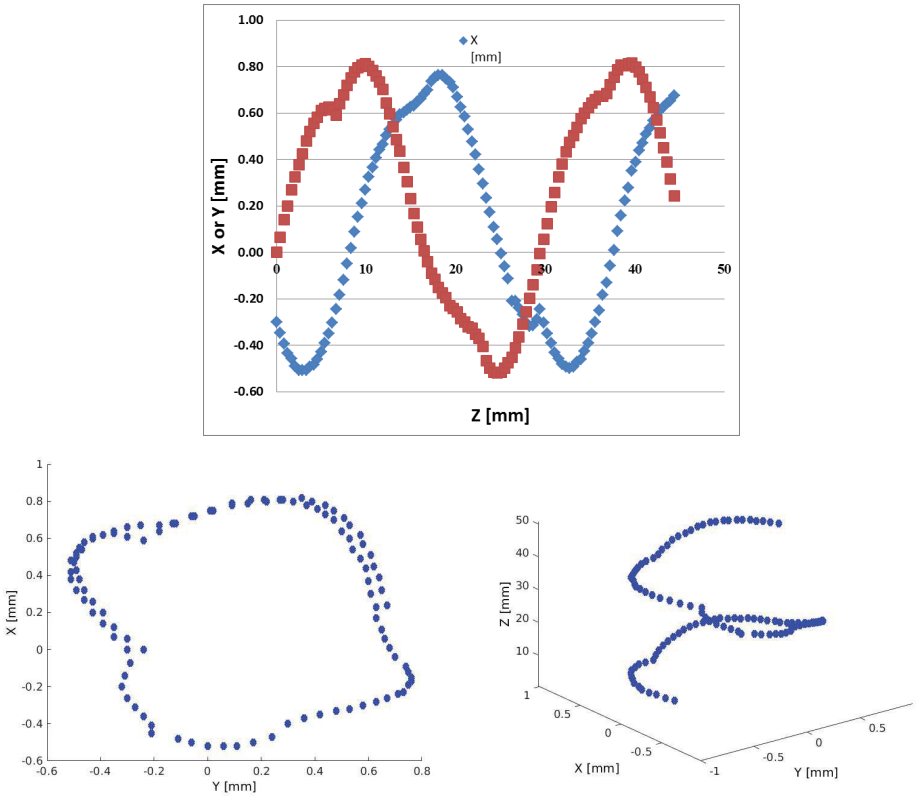


FIGURE 5.9: Helical path of bubble in side view of XZ,YZ plane (top),top view of XY plane (bottom left) and 3D view of path (bottom right)

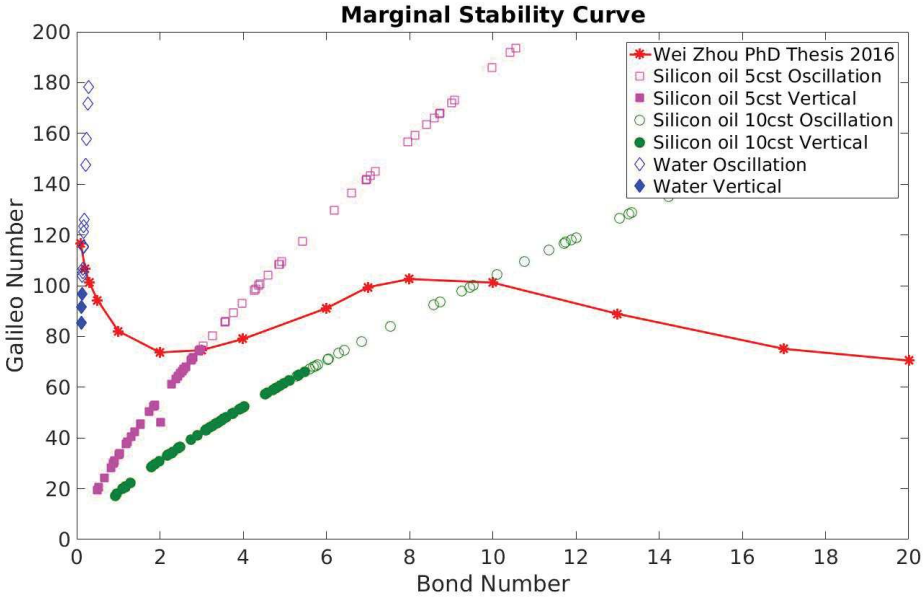


FIGURE 5.10: Marginal Stability curve of present work and Zhou et al., 2017 Open symbols : oscillating path and closed symbols : vertical path

The threshold values of instability from the current experiments are given in table 5.1

TABLE 5.1: Threshold values of water, silicon oil of 5 cst and 10 cst observed experimentally.

| Critical value | Bond | Galileo | Reynolds |
|---|---|---|---|
| Water | 0.17 | 122 | 170 |
| Silicon oil 5 cst | 3.1 | 77 | 95 |
| Silicon oil 10 cst | 5.6 | 60.4 | 65 |

Critical values of diameter, velocity and frequency of oscillation at the onset of oscillations are given in table 5.2.

TABLE 5.2: Characteristics of bubble at the instability threshold.

| Critical value | Viscosity [Pa.s] | Diameter [mm] | Velocity [m/s] | Frequency [Hz] |
|---|---|---|---|---|
| Water | 0.001 | 1.1 | 0.155 | 11 |
| Silicon oil 5 cst | 0.005 | 2.7 | 0.196 | 6.7 |
| Silicon oil 10 cst | 0.01 | 3.5 | 0.185 | 5.9 |

## 5.6 Frequency and Amplitude of oscillation

By fitting the bubble path by a sinusoidal function, we measured the frequency and amplitude of oscillation of bubble rising in silicon oil of 10 cst. The non dimensional frequency $= Frequency * \sqrt{d/g}$. is approximately constant and equal to 0.15. This value is relatively in agreement with theoretical calculations of Zhou et al., 2017 predicting rather a frequency of 0.2.

Amplitude of oscillation of the bubble path shows a super critical bifurcation with an increase that can be fitted with a parabola $\sqrt{Ga}$ (see figure 5.12). This shows that the saturation is reached at the registered position and is a typical behavior of Hopf bifurcation.

## 5.7 Conclusion and Perspective

From the current experimental work, we are able to find only three points on the marginal stability curve. The experimental threshold values are in agreement with the numerical simulation results of Zhou et al., 2017 for bubbles rising in demineralized water and silicon oil of 5 cst. However, we found a

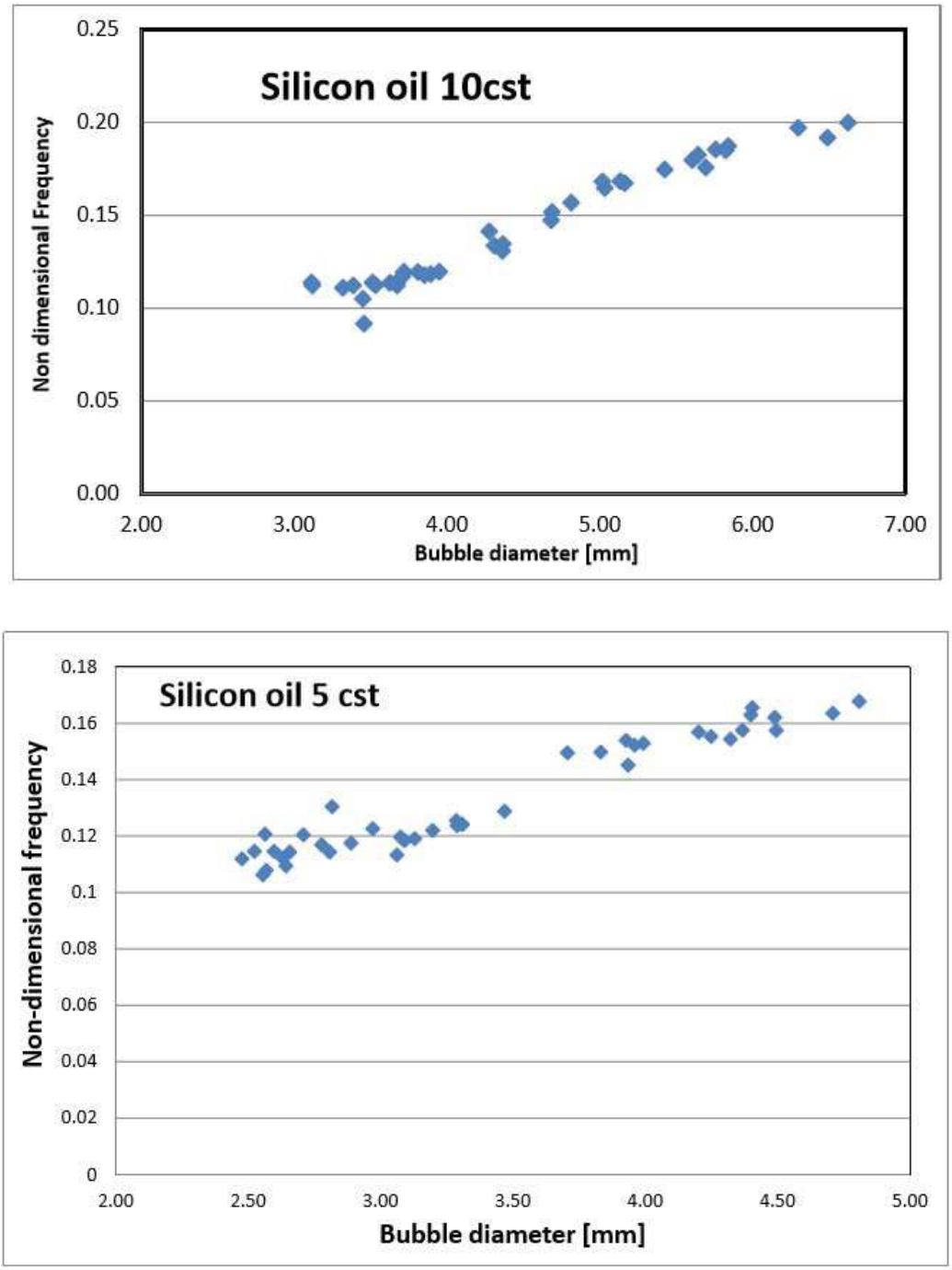


FIGURE 5.11: Non dimensional frequency of oscillation of the rising bubble in silicon oil of 10cst and 5cst.

lower threshold in bubbles rising in silicon oil of 10 cst. Further experiments are required in silicon oils of various viscosities to obtain more points on the instability threshold curve. Various regimes of bubble path and shape were studied using simple optical setup and image processing technique. Experimental value of the non dimensional frequency of bubble oscillation (10)

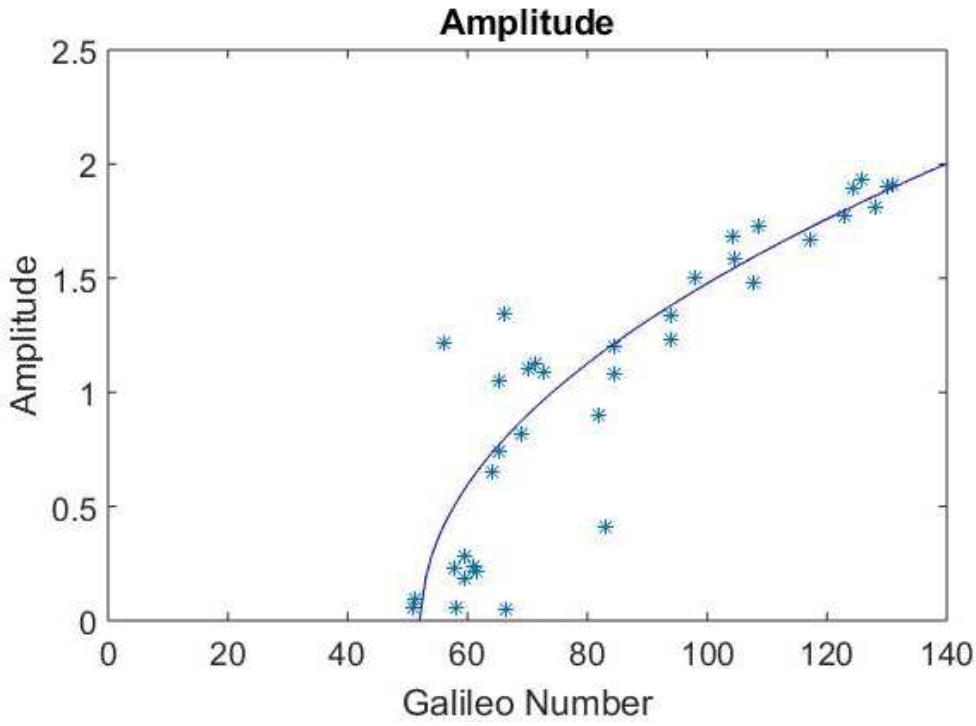


FIGURE 5.12: Amplitude of oscillation of bubble in silicon oil of 10cst : parabolic fit indicates hopf bifurcation

are in agreement with theoretical calculations of Zhou et al., 2017 . An indication of Hopf bifurcation is observed in the amplitude of oscillation. The oscillation amplitude increases in super critical parabolic shape with $\sqrt{Ga}$, indicating that the saturation is achieved. From our experiment, it is evident that the shape of the bubble has major impact on the path instability of rising bubble.

One of the major challenges in this experiment is to find an efficient method to control the bubble diameter. Although the solenoid valve and pressurized tank helped us to control the bubble diameter to a certain extent, the existing setup could not provide bubbles of specific diameter, in order to focus on bubbles near the threshold of instability. A longer channel is required to record the bubble path in the saturated regime, above the initial perturbations. A camera placed on the top of the setup also would help in visualizing the shape deformations of the bubble. This is especially interesting to validate with the existing numerical results on bubble shape deformations (Zhou et al., 2017).

# Chapter 6

# Conclusion

In this PhD thesis, three different types of experiments were conducted to visualize the fluid flow fluctuations in two fluid mechanics problems namely, *Rayleigh Bénard Convection* and *Bubble rising in a liquid*. Different visualization techniques such as Laser Induced Fluorescence and Particle Image Velocimetry were applied to study the flow field.

## 6.1 Rayleigh Bénard Convection

Rayleigh Bénard convection has been studied with and without rotation, at various Rossby number and Rayleigh number values. Flow field transition in the rotation unaffected and rotation affected regimes was studied in the complete mid symmetrical vertical plane of the Rayleigh Bénard cell of aspect ratio 1. The flow field is analyzed at three different heights of RBC cell, 5% of the cell height near the bottom plate, mid height and 95% of the cell height near the top plate. The following conclusions can be drawn from the present study.

- Large scale circulation was found to be the dominant flow structure in rotation unaffected regime. The vertical columns form under the effect of Ekman pumping in the rotation affected regime. The vorticity is developed initially in the boundary layers. The columns expand in the complete vertical extent for Rossby numbers < 0.1. Large scale circulation can not be found for Rossby numbers < 1.2.
- The strength of large scale circulation increases near the transition from rotation unaffected to rotation affected regime. In the rotation affected regime and the rotation dominated regime, the strength of large scale circulation is approximately zero, which indicates that the dominant

flow structure is not large scale circulation in the rotation affected regime and rotation dominated regime.

- The vorticity developed in the boundary layers, decreases as one moves away from the boundary into the bulk. The vorticity changes sign, i.e. columns change the direction of rotation in the mid way. Hence, the columns are rotating in opposite direction at the top and bottom plates. This is confirmed in our experimental study of the cross correlation of the horizontal velocities. The cross correlation of horizontal velocities in the regions near the top and bottom plates, show that the velocities are out of phase.

- The cross correlation of vertical velocity are in phase, in the regions near the top and bottom plates. This explains that the vertical columns extend from one plate to the other. Periodicity is found in the cross correlation of vertical velocity in rotation affected regime. This explains that the columns are alternatively rising and falling when observed along the horizontal direction of the cell. No periodicity is found for the vertical velocity in the rotation unaffected regime.

- The spatial auto correlation of the vertical velocity was studied for various Rossby and Rayleigh numbers. The periodicity in the auto correlation of vertical velocity is absent in the rotation unaffected regime and it is present in the rotation affected regime and rotation dominated regime. The first minimum of auto-correlation was considered as the correlation parameter that defines the width of the columns. The first minimum of auto correlation of vertical velocity decreases with increasing Rossby number due to increasing number of columns with increasing rotation rate. The first minimum was found to be approximately equal , for different Rayleigh numbers (5.3e+08, 2.7e+08), at low Rossby numbers in the rotation dominated regime. This indicates that the width of columns seems to level off below a specific rotation rate.

- Velocity fluctuation field was studied in the complete mid vertical plane. Velocity fluctuations increase in the rotation unaffected regime until the critical Rossby number (Ro = 2.5). Beyond the critical rotation rate, in the rotation affected regime the velocity fluctuations decrease with increasing rotation speed. Fluctuations show a strong anisotropy : vertical velocity fluctuations are higher than horizontal velocity fluctuations. The anisotropy is also spatial. When one compares the horizontal

velocity fluctuations at the mid height of the cell, the horizontal velocity fluctuations are higher near the top and bottom plates, due to strong vorticity near the boundary layers. The fluctuation ratio $(u_{rms}/v_{rms})$ is the same at various height in the cell, at the critical Rossby = 2.5. In the rotation affected regime, the fluctuation ratio increases with decreasing Rossby number near the top and bottom plates. The rate of decrease of the vertical velocity fluctuation is stronger than the rate of decrease of the horizontal velocity fluctuation near the top and bottom plates. Our experimental results are in agreement with the results of Rajaei et al., 2016. Our experimental results provide complementary information on the fluctuations in the regions near the bottom plate. Fluctuations also increase with increasing Rayleigh numbers as turbulence increases with increasing Rayleigh numbers.

- Onset of convection was studied at constant rotation rate (2.7 rad/s) and various Rayleigh numbers. The velocity magnitude contours are studied for various Rayleigh numbers. The columns are well formed at Ra > 1.15e+08 extending from one plate to the other. Since the convection is in the vertical direction, the mean vertical velocity was measured for various Rayleigh numbers. The mean vertical velocity changes slope for Ra > 3.6e+08 (near to value from Chandrasekhar formula Ra = 3.1e+08), and increases linearly with increasing Rayleigh numbers. Further experiments are required particularly focussing near the convective onset Ra = 3.1e+08.

- The 2 dyes 2 bands laser induced fluorescence technique was used to study the temperature field of Rayleigh Bénard convection with and without rotation. We conducted LIF experiment using various fluorescent dyes to find out combination of dyes which are highly sensitive to temperature . We found that the fluoroscein disodium and sulforhodamine dye combination yielded higher sensitivity to temperature but the solution is sensitive to pH and unstable with the time. The solution of Rhodamine 560 and Keton Red yielded high sensitivity with temperature and no sensitivity to pH. The experimental results show transition from large scale circulation in the rotation unaffected regime to the vertical columns in the rotation affected regime. The plumes have mushroom shape at moderate rotation speed. Instantaneous temperature field shows hot and cold plumes swirling up and down in the vertical extent of the cell at moderate rotation speed (0.1 < Ro < 2.5). In

the rotation affected regime, the vorticity developed in the boundary layers restricts the detachment of the plumes and hence, plumes form longer tails attached to the boundary layer, before eventually detaching from the boundary layer. For the higher rotational speed at Rossby = 0.1 , the flow field is dominated by rotation and the mushroom shape of the plume is not visible anymore. The hot and cold columns extend from one plate to the other. The hot and cold vertical columns occur alternatively, in the horizontal direction of the cell, when viewed in the vertical plane of aymmetry the cell.

## 6.2 Instability of rising bubbles

Path of the bubbles of different diameters, rising in silicon oil of 5 cst, 10 cst, 500 cst and demineralized water was observed experimentally in a square cross section cell of 50cm height. The transition from straight path for very small diameter bubbles to the oscillating path with various flow regimes such as zig-zag and helical path were observed. Bubbles start to oscillate while rising in demineralized water for diameter > 1.1 mm which correspond to Bo > 0.17 and Ga > 122. In the case of bubbles rising in silicon oil of 5cst, the threshold of instability is found at Bo = 3.1 and Ga = 77. Our experimental results yield three points on the marginal instability curve. For experiments in purified water and silicon oil of 5cst, our experimental threshold values are in agreement with the numerical results of Zhou et al., 2017. Experiments conducted on bubbles rising in silicon oil of 10 cst resulted in lower threshold values than that predicted by Zhou et al., 2017. In silicon oil 10 cst, the bubbles start to oscillate for diameter > 3.5 mm which correspond to Bo = 5.6 and Ga = 60.4. The Non dimensional frequency $(frequency * \sqrt{d/g})$ of bubble oscillation is found to be approximately equal to 0.15 for bubbles of various diameters in silicon oil of 10 cst. This result is in partial agreement with the theoritical predictions of Zhou et al., 2017. An indication of Hopf bifurcation is observed in the amplitude of oscillation. The oscillation amplitude increases in super critical parabolic shape with $\sqrt{Ga}$, indicating that the saturation is achieved.

## 6.3 Perspectives

The LIF experiments conducted in rotating Rayleigh Bénard convection can be extended to rotation dominated regime to observe the transition from rotation affected regime to rotation dominated regime. The present results on temperature flow field remain qualitative due to the defects in images such as defraction lines caused by the difference in density of rising hot and falling cold plumes. An algorithm to remove the defraction lines has to be developed in the further study. The LIF experiment setup in the present work can be further improved by using finer grid to calibrate the image transformation required for the division of two images obtained from the two dyes. With these modifications the quantitative temperature measurements in the vertical mid plane should be obtained.

The experimental study can also be extended for various Prandtl numbers and for variable aspect ratio of cell to define their effects on the critical Rossby number. More investigation is required in the rotation unaffected regime to investigate the large scale flow dynamics under the affect of rotation. The multiple transitions of Nusselt number with decreasing Rossby number in the rotation unaffected regime, as observed in the results of Wei et al., 2015, could be explained in more detail with the help of more experimental results on the fluid flow transitions in the rotation unaffected regime. It is necessary to develop three dimensional flow visualization experiment setup in order to completely understand the dynamics of vortical columns in the rotation affected regime.

The experiments conducted to study the path instability of rising bubbles, could be extended to various viscous liquids to obtain more points on the marginal stability curve. The shape oscillations could be studied by using an additional camera to view from top of the cell. Three dimensional shape and path of the bubble can be reconstructed using the top (XY plane) view along with the XZ and YZ plane view obtained in this experiment. The length of the column should be increased to see the multiple transitions that occur while the bubble is rising. The present setup could not control the size of the bubbles effectively. A robust experiment setup is needed to have proper control on the size of the bubbles. The initial perturbation caused while inducing the bubble into the column should also be reduced.

# Bibliography

Ahlers, Guenter et al. (2006). "Non-Oberbeck–Boussinesq effects in strongly turbulent Rayleigh–Bénard convection". In: *Journal of fluid mechanics* 569, pp. 409–445.

Ahlers, Guenter, Siegfried Grossmann, and Detlef Lohse (2009). "Heat transfer and large scale dynamics in turbulent Rayleigh-Bénard convection". In: *Reviews of modern physics* 81.2, p. 503.

Alards, Kim MJ et al. (2018). "Directional change of tracer trajectories in rotating Rayleigh-Bénard convection". In: *Physical Review E* 97.6, p. 063105.

BEEsLEy, DAViD et al. (2008). "A laboratory demonstration of Coriolis effects on wind-driven ocean currents". In: *Oceanography* 21.2, pp. 72–76.

Bénard, Henri (1900). "Étude expérimentale des courants de convection dans une nappe liquide.—Régime permanent: tourbillons cellulaires". In: *Journal de Physique Théorique et Appliquée* 9.1, pp. 513–524.

Boubnov, BM and GS Golitsyn (1990). "Temperature and velocity field regimes of convective motions in a rotating plane fluid layer". In: *Journal of Fluid Mechanics* 219, pp. 215–239.

Boussinesq, J_ (1903). "Theorie Analytique de la Chaleur vol 2 (Paris: Gauthier-Villars)". In:

Brown, Eric, Alexei Nikolaenko, and Guenter Ahlers (2005). "Reorientation of the large-scale circulation in turbulent Rayleigh-Bénard convection". In: *Physical review letters* 95.8, p. 084503.

Brown, Eric and Guenter Ahlers (2006). "Rotations and cessations of the large-scale circulation in turbulent Rayleigh–Bénard convection". In: *Journal of Fluid Mechanics* 568, pp. 351–386.

Bruchhausen, Matthias, Fabrice Guillard, and Fabrice Lemoine (2005). "Instantaneous measurement of two-dimensional temperature distributions by means of two-color planar laser induced fluorescence (PLIF)". In: *Experiments in fluids* 38.1, pp. 123–131.

Cano-Lozano, JC, P Bohorquez, and C Martínez-Bazán (2013). "Wake instability of a fixed axisymmetric bubble of realistic shape". In: *International Journal of Multiphase Flow* 51, pp. 11–21.

Castaing, Bernard et al. (1989). "Scaling of hard thermal turbulence in Rayleigh-Bénard convection". In: *Journal of Fluid Mechanics* 204, pp. 1–30.

Castillo-Castellanos, Andres, Anne Sergent, and Maurice Rossi (2016). "Reversal cycle in square Rayleigh–Bénard cells in turbulent regime". In: *Journal of Fluid Mechanics* 808, pp. 614–640.

Chandrasekhar, S (1961). "Hydrodynamic and hydromagnetic stability". In: *Oxford University Press,Oxford*.

Chavanne, X et al. (2001). "Turbulent Rayleigh–Bénard convection in gaseous and liquid He". In: *Physics of Fluids* 13.5, pp. 1300–1320.

Coppeta, J and C Rogers (1998). "Dual emission laser induced fluorescence for direct planar scalar behavior measurements". In: *Experiments in Fluids* 25.1, pp. 1–15.

Crimaldi, JP (2008). "Planar laser induced fluorescence in aqueous flows". In: *Experiments in fluids* 44.6, pp. 851–863.

Duineveld, PC (1995). "The rise velocity and shape of bubbles in pure water at high Reynolds number". In: *Journal of Fluid Mechanics* 292, pp. 325–332.

Dunn, Michael G (2001). "Convective heat transfer and aerodynamics in axial flow turbines". In: *ASME Turbo Expo 2001: Power for Land, Sea, and Air*. American Society of Mechanical Engineers, V004T06A001–V004T06A001.

Ekman, Vagn Walfrid et al. (1905). "On the influence of the earth's rotation on ocean-currents." In:

Ellingsen, Kjetil and Frederic Risso (2001). "On the rise of an ellipsoidal bubble in water: oscillatory paths and liquid-induced velocity". In: *Journal of Fluid Mechanics* 440, pp. 235–268.

Funfschilling, Denis and Guenter Ahlers (2004). "Plume motion and large-scale circulation in a cylindrical Rayleigh-Bénard cell". In: *Physical review letters* 92.19, p. 194502.

Funfschilling, Denis, Eric Brown, and Guenter Ahlers (2008). "Torsional oscillations of the large-scale circulation in turbulent Rayleigh–Bénard convection". In: *Journal of Fluid Mechanics* 607, pp. 119–139.

Greenspan, HP (1968). "The theory of rotating fluids Cambridge University Press". In: *Cambridge, England* 1.

Grooms, Ian et al. (2010). "Model of convective Taylor columns in rotating Rayleigh-Bénard convection". In: *Physical review letters* 104.22, p. 224501.

Grossmann, Siegfried and Detlef Lohse (2000). "Scaling in thermal convection: a unifying theory". In: *Journal of Fluid Mechanics* 407, pp. 27–56.

– (2004). "Fluctuations in turbulent Rayleigh–Bénard convection: the role of plumes". In: *Physics of fluids* 16.12, pp. 4462–4472.

Haberman, William L and RK Morton (1953). *An experimental investigation of the drag and shape of air bubbles rising in various liquids*. Tech. rep. David Taylor Model Basin Washington DC.

Hartunian, Richard Aram and WR Sears (1957). "On the instability of small gas bubbles moving uniformly in various liquids". In: *Journal of Fluid Mechanics* 3.1, pp. 27–47.

Heimpel, Moritz and Jonathan Aurnou (2007). "Turbulent convection in rapidly rotating spherical shells: A model for equatorial and high latitude jets on Jupiter and Saturn". In: *Icarus* 187.2, pp. 540–557.

Horn, Susanne and Olga Shishkina (2014). "Rotating non-Oberbeck–Boussinesq Rayleigh–Bénard convection in water". In: *Physics of Fluids* 26.5, p. 055111.

– (2015). "Toroidal and poloidal energy in rotating Rayleigh–Bénard convection". In: *Journal of Fluid Mechanics* 762, pp. 232–255.

Ingersoll, Andrew P (1990). "Atmospheric dynamics of the outer planets". In: *Science* 248.4953, pp. 308–315.

Jablonski, Aleksander (1933). "Efficiency of anti-Stokes fluorescence in dyes". In: *Nature* 131.3319, p. 839.

Jeffreys, Harold (1926). "LXXVI. The stability of a layer of fluid heated below". In: *The London, Edinburgh, and Dublin Philosophical Magazine and Journal of Science* 2.10, pp. 833–844.

Jenkins, D. R. (1988). "Interpretation of shadowgraph patterns in Rayleigh-Bénard convection". In: *Journal of Fluid Mechanics* 190, 451–469. DOI: 10.1017/S0022112088001405.

Johnston, James P (1998). "Effects of system rotation on turbulence structure: a review relevant to turbomachinery flows". In: *International Journal of rotating machinery* 4.2, pp. 97–112.

Julien, K et al. (1996a). "Hard turbulence in rotating Rayleigh-Bénard convection". In: *Physical Review E* 53.6, R5557.

– (1996b). "Rapidly rotating turbulent Rayleigh-Bénard convection". In: *Journal of Fluid Mechanics* 322, pp. 243–273.

Julien, K et al. (2012). "Statistical and physical balances in low Rossby number Rayleigh–Bénard convection". In: *Geophysical & Astrophysical Fluid Dynamics* 106.4-5, pp. 392–428.

Kadanoff, Leo P (2001). "Turbulent heat flow: structures and scaling". In: *Physics today* 54.8, pp. 34–39.

Kraichnan, Robert H (1962). "Turbulent thermal convection at arbitrary Prandtl number". In: *The Physics of Fluids* 5.11, pp. 1374–1389.

Kundu, Pijush K, Ira M Cohen, and DW Dowling (2008). *Fluid Mechanics 4th*.

Kunnen, RPJ, HJH Clercx, and Bernardus J Geurts (2008). "Breakdown of large-scale circulation in turbulent rotating convection". In: *EPL (Europhysics Letters)* 84.2, p. 24001.

Kunnen, RPJ, Bernardus J Geurts, and HJH Clercx (2010). "Experimental and numerical investigation of turbulent convection in a rotating cylinder". In: *Journal of fluid mechanics* 642, pp. 445–476.

Kunnen, RPJ, HJH Clercx, and GJF Van Heijst (2013). "The structure of side-wall boundary layers in confined rotating Rayleigh–Bénard convection". In: *Journal of fluid mechanics* 727, pp. 509–532.

Kunnen, Rudie PJ et al. (2011). "The role of Stewartson and Ekman layers in turbulent rotating Rayleigh–Bénard convection". In: *Journal of fluid mechanics* 688, pp. 422–442.

Kunnen, Rudie PJ, Yoann Corre, and Herman JH Clercx (2014). "Vortex plume distribution in confined turbulent rotating convection". In: *EPL (Europhysics Letters)* 104.5, p. 54002.

Labergue, Alexandre et al. (2012). "Study of the droplet size effect coupled with the laser light scattering in sprays for two-color LIF thermometry measurements". In: *Experiments in fluids* 52.5, pp. 1121–1132.

Landau, Lev Davidovich and Evgenii Mikhailovich Lifshits (1959). *Fluid mechanics, by LD Landau and EM Lifshitz*. Vol. 11. Pergamon Press Oxford, UK.

Lemoine, F et al. (1999). "Simultaneous temperature and 2D velocity measurements in a turbulent heated jet using combined laser-induced fluorescence and LDA". In: *Experiments in fluids* 26.4, pp. 315–323.

Lunde, Knud and Richard J Perkins (1998). "Shape oscillations of rising bubbles". In: *In Fascination of Fluid Dynamics*. Springer, pp. 387–408.

Magnaudet, Jacques and Guillaume Mougin (2007). "Wake instability of a fixed spheroidal bubble". In: *Journal of Fluid Mechanics* 572, pp. 311–337.

Malkus, WILLEM VR (1954). "Discrete transitions in turbulent convection". In: *Proceedings of the Royal Society of London. Series A. Mathematical and Physical Sciences* 225.1161, pp. 185–195.

Maqua, Christophe, Guillaume Castanet, and Fabrice Lemoine (2008). "Bi-component droplets evaporation: Temperature measurements and modelling". In: *Fuel* 87.13-14, pp. 2932–2942.

Marshall, John and Friedrich Schott (1999). "Open-ocean convection: Observations, theory, and models". In: *Reviews of Geophysics* 37.1, pp. 1–64.

Mougin, Guillaume and Jacques Magnaudet (2001). "Path instability of a rising bubble". In: *Physical review letters* 88.1, p. 014502.

Nakajima, Tsuyoshi, Motoyasu Utsunomiya, and Yuji Ikeda (1991). "Simultaneous measurement of velocity and temperature of water using LDV and fluorescence technique". In: *Applications of Laser Techniques to Fluid Mechanics*. Springer, pp. 34–53.

Niemela, J et al. (2001). "The wind in confined thermal turbulence". In: *J. Fluid Mech* 449, pp. 169–178.

Niemela, JJ et al. (2000). "Turbulent convection at very high Rayleigh numbers". In: *Nature* 404.6780, p. 837.

Nieves, David, Antonio M Rubio, and Keith Julien (2014). "Statistical classification of flow morphology in rapidly rotating Rayleigh-Bénard convection". In: *Physics of Fluids* 26.8, p. 086602.

Oberbeck, Anton (1879). "Über die Wärmeleitung der Flüssigkeiten bei Berücksichtigung der Strömungen infolge von Temperaturdifferenzen". In: *Annalen der Physik* 243.6, pp. 271–292.

Ohl, CD, A Tijink, and Andrea Prosperetti (2003). "The added mass of an expanding bubble". In: *Journal of fluid mechanics* 482, pp. 271–290.

Pedlosky, Joseph and JS Robertson (1988). *Geophysical fluid dynamics by Joseph Pedlosky*.

Petracci, Alberto, René Delfos, and Jerry Westerweel (2006). "Combined PIV/LIF measurements in a Rayleigh-Bénard convection cell". In: *13th International Symposium on Applications of Laser Techniques to Fluid Mechanics, Lisbon*.

Portegies, JW et al. (2008). "A model for vortical plumes in rotating convection". In: *Physics of Fluids* 20.6, p. 066602.

Prandtl, Ludwig (1932). "Meteorologische anwendung der strömungslehre". In: *Beitr. Phys. Atmos* 19, pp. 188–202.

Raffel, Markus et al. (2018). *Particle image velocimetry: a practical guide*. Springer.

Rajaei, Hadi et al. (2016). "Transitions in turbulent rotating convection: A Lagrangian perspective". In: *Physical Review E* 93.4, p. 043129.

Rajaei, Hadi, Rudie PJ Kunnen, and Herman JH Clercx (2017). "Exploring the geostrophic regime of rapidly rotating convection with experiments". In: *Physics of Fluids* 29.4, p. 045105.

Rajaei, Hadi et al. (2018). "Velocity and acceleration statistics in rapidly rotating Rayleigh–Bénard convection". In: *Journal of fluid mechanics* 857, pp. 374–397.

Rayleigh, Lord (1916). "LIX. On convection currents in a horizontal layer of fluid, when the higher temperature is on the under side". In: *The London, Edinburgh, and Dublin Philosophical Magazine and Journal of Science* 32.192, pp. 529–546.

Reynolds, Osborne (1883). "XXIX. An experimental investigation of the circumstances which determine whether the motion of water shall be direct or sinuous, and of the law of resistance in parallel channels". In: *Philosophical Transactions of the Royal society of London* 174, pp. 935–982.

Ribeiro, Adolfo et al. (2015). "Canonical models of geophysical and astrophysical flows: Turbulent convection experiments in liquid metals". In: *Metals* 5.1, pp. 289–335.

Rossby, HT (1969). "A study of Bénard convection with and without rotation". In: *Journal of Fluid Mechanics* 36.2, pp. 309–335.

Sakakibara, Jun and Ronald J Adrian (1999). "Whole field measurement of temperature in water using two-color laser induced fluorescence". In: *Experiments in Fluids* 26.1-2, pp. 7–15.

Schlichting, Hermann et al. (1974). *Boundary-layer theory*. Springer.

Shishkina, Olga and Claus Wagner (2006). "Analysis of thermal dissipation rates in turbulent Rayleigh–Bénard convection". In: *Journal of Fluid Mechanics* 546, pp. 51–60.

Sreenivasan, Katepalli R, Alexander Bershadskii, and JJ Niemela (2002). "Mean wind and its reversal in thermal convection". In: *Physical Review E* 65.5, p. 056306.

Stasiek, JA and TA Kowalewski (2002). "Thermochromic liquid crystals applied for heat transfer research". In: *Optoelectronics review* 10.1, pp. 1–10.

Stellmach, S et al. (2014). "Approaching the asymptotic regime of rapidly rotating convection: boundary layers versus interior dynamics". In: *Physical review letters* 113.25, p. 254501.

Stevens, Richard JAM et al. (2009). "Transitions between turbulent states in rotating Rayleigh-Bénard convection". In: *Physical review letters* 103.2, p. 024503.

Stevens, Richard JAM, Herman JH Clercx, and Detlef Lohse (2010a). "Boundary layers in rotating weakly turbulent Rayleigh–Bénard convection". In: *Physics of fluids* 22.8, p. 085103.

– (2010b). "Optimal Prandtl number for heat transfer in rotating Rayleigh–Bénard convection". In: *New journal of physics* 12.7, p. 075005.

– (2013). "Heat transport and flow structure in rotating Rayleigh–Bénard convection". In: *European Journal of Mechanics-B/Fluids* 40, pp. 41–49.

Stewartson, K (1957). "On almost rigid rotations". In: *Journal of Fluid Mechanics* 3.1, pp. 17–26.

– (1966). "On almost rigid rotations. Part 2". In: *Journal of fluid mechanics* 26.1, pp. 131–144.

Thielicke, William and Eize Stamhuis (2014). "PIVlab–towards user-friendly, affordable and accurate digital particle image velocimetry in MATLAB". In: *Journal of Open Research Software* 2.1.

Tripathi, Manoj Kumar, Kirti Chandra Sahu, and Rama Govindarajan (2015). "Dynamics of an initially spherical bubble rising in quiescent liquid". In: *Nature communications* 6, p. 6268.

Van Santen, Helmar, Chris R Kleijn, and Harry EA Van Den Akker (2000). "On turbulent flows in cold-wall CVD reactors". In: *Journal of crystal growth* 212.1-2, pp. 299–310.

Veldhuis, Christian (2007). "Leonardo's paradox: Path and shape instabilities of particles and bubbles". In:

Veronis, G (1959). "Cellular convection with finite amplitude in a rotating fluid". In: *Journal of Fluid Mechanics* 5.3, pp. 401–435.

Vorobieff, Peter and Robert E Ecke (1998). "Vortex structure in rotating Rayleigh-Benard convection". In: *Physica D: Nonlinear Phenomena* 123.1-4, pp. 153–160.

– (2002). "Turbulent rotating convection: an experimental study". In: *Journal of Fluid Mechanics* 458, pp. 191–218.

Vries, Antoine Wilhelmus Gerardus de (2002). "Path and wake of a rising bubble." In:

Wei, Ping, Stephan Weiss, and Guenter Ahlers (2015). "Multiple transitions in rotating turbulent Rayleigh-Bénard convection". In: *Physical review letters* 114.11, p. 114506.

Weiss, S. et al. (2010a). "Finite-Size Effects Lead to Supercritical Bifurcations in Turbulent Rotating Rayleigh-Bénard Convection". English. In: *Physical Review Letters* 105.22, pp. 224501–1/4. ISSN: 0031-9007.

Weiss, Stephan et al. (2010b). "Finite-size effects lead to supercritical bifurcations in turbulent rotating Rayleigh-Bénard convection". In: *Physical review letters* 105.22, p. 224501.

Weiss, Stephan and Guenter Ahlers (2011). "The large-scale flow structure in turbulent rotating Rayleigh–Bénard convection". In: *Journal of Fluid Mechanics* 688, pp. 461–492.

Weiss, Stephan, Ping Wei, and Guenter Ahlers (2015). "Rayleigh- and Prandtl-number dependence of the large-scale flow-structure in weakly-rotating turbulent thermal convection". In: *APS Division of Fluid Dynamics Meeting Abstracts*, p. M10.002.

Weiss, Stephan, Ping Wei, and Guenter Ahlers (2016). "Heat-transport enhancement in rotating turbulent Rayleigh-Bénard convection". In: *Physical Review E* 93.4, p. 043102.

Xi, Heng-Dong, Siu Lam, and Ke-Qing Xia (2004). "From laminar plumes to organized flows: the onset of large-scale circulation in turbulent thermal convection". In: *Journal of Fluid Mechanics* 503, pp. 47–56.

Xi, Heng-Dong and Ke-Qing Xia (2007). "Cessations and reversals of the large-scale circulation in turbulent thermal convection". In: *Physical Review E* 75.6, p. 066307.

– (2008a). "Azimuthal motion, reorientation, cessation, and reversal of the large-scale circulation in turbulent thermal convection: a comparative study in aspect ratio one and one-half geometries". In: *Physical Review E* 78.3, p. 036326.

– (2008b). "Flow mode transitions in turbulent thermal convection". In: *Physics of Fluids* 20.5, p. 055104.

Xi, Heng-Dong et al. (2009). "Origin of the temperature oscillation in turbulent thermal convection". In: *Physical review letters* 102.4, p. 044503.

Zenit, Roberto and Jacques Magnaudet (2008). "Path instability of rising spheroidal air bubbles: a shape-controlled process". In: *Physics of Fluids* 20.6, p. 061702.

– (2009). "Measurements of the streamwise vorticity in the wake of an oscillating bubble". In: *International Journal of Multiphase Flow* 35.2, pp. 195–203.

Zhong, Fang, Robert Ecke, and Victor Steinberg (1991). "Asymmetric modes and the transition to vortex structures in rotating Rayleigh-Bénard convection". In: *Physical review letters* 67.18, p. 2473.

Zhong, Fang, Robert E Ecke, and Victor Steinberg (1993). "Rotating Rayleigh–Bénard convection: asymmetric modes and vortex states". In: *Journal of Fluid Mechanics* 249, pp. 135–159.

Zhong, Jin-Qiang and Guenter Ahlers (2010). "Heat transport and the large-scale circulation in rotating turbulent Rayleigh–Bénard convection". In: *Journal of Fluid Mechanics* 665, pp. 300–333.

Zhou, Quan et al. (2009). "Oscillations of the large-scale circulation in turbulent Rayleigh–Bénard convection: the sloshing mode and its relationship with the torsional mode". In: *Journal of Fluid Mechanics* 630, pp. 367–390.

Zhou, Quan and Ke-Qing Xia (2010). "Physical and geometrical properties of thermal plumes in turbulent Rayleigh–Bénard convection". In: *New Journal of Physics* 12.7, p. 075006.

Zhou, Sheng-Qi, Chao Sun, and Ke-Qing Xia (2007). "Measured oscillations of the velocity and temperature fields in turbulent Rayleigh-Bénard convection in a rectangular cell". In: *Physical Review E* 76.3, p. 036301.

Zhou, W and J Dušek (2017). "Marginal stability curve of a deformable bubble". In: *International Journal of Multiphase Flow* 89, pp. 218–227.

## Liste des communications effectuées au cours de la thèse

- MOTURI V. M., FUNFSCHILLING D., DUSEK J., *Experimental study of the path instability of rising bubbles,* GDR Film Cisaillé, Aussois, les 4-6 Janvier 2017 (communication orale)

- MOTURI V. M., DUSEK J., FUNFSCHILLING D., *Structure of plumes in Turbulent Rayleigh-Bénard convection,* CFM (Congrès Français de Mécanique), Lille, les 28 Aout – 1er Septembre 2017 (communication orale)

- MOTURI V. M., FUNFSCHILLING D., DUSEK J., *Experimental study of the path instability of rising bubbles,* CFM (Congrès Français de Mécanique), Lille, les 28 Aout – 1er Septembre 2017 (communication orale)

- MOTURI V. M., DUSEK J., FUNFSCHILLING D., *Structure of plumes in Turbulent Rayleigh-Bénard convection,* Séminaire de l'école doctorale MSII, Strasbourg, 8 Septembre 2017 (poster)

- FUNFSCHILLING D., MOTURI V. M., DUSEK J., *Experimental study of the path instability of rising bubbles,* IGAFD (Interdisciplinary Geo-Astro Fluid Dynamics) CNRS Paris, October 16-18, 2017 (communication orale)

- MOTURI V. M., DUSEK J., FUNFSCHILLING D., *Structure of plumes in Turbulent Rayleigh-Bénard convection,* IGAFD (Interdisciplinary Geo-Astro Fluid Dynamics), CNRS Paris, October 16-18, 2017 (communication orale)

- FUNFSCHILLING D., MOTURI V., DUSEK J., *Experimental Study on Path Instability of Rising Bubbles,* GDR Ruissellement et films cisaillés, Journées des 18, 19 et 20 décembre 2017

- MOTURI V., FUNFSCHILLING D., DUSEK J., *Structure of Plumes in Turbulent Rayleigh Bénard Convection,* GDR Ruissellement et films cisaillés, Journées des 18, 19 et 20 décembre 2017

- MOTURI V., FUNFSCHILLING D., DUSEK J., *Visualization of plumes in high Pandtl Rayleigh Bénard convection,* International Conference on Rayleigh-Bénard Turbulence, 14-18 May 2018 University of Twente – Enschede – The Netherlands

- FUNFSCHILLING D., MOTURI V., DUSEK J., *Structure of Plumes in Rayleigh-Bénard turbulent convection,* International Conference on Rayleigh-Bénard Turbulence, 14-18 May 2018 University of Twente – Enschede – The Netherlands

- MOTURI V., FUNFSCHILLING D., DUSEK J., *Rotating Turbulent Rayleigh-Bénard convection,* Journées du Département Mécanique, 23 Mai 2019, ICube Strasbourg (Oral communication).

- MOTURI V., FUNFSCHILLING D., WEISS S., *Rotating Turbulent Rayleigh-Bénard convection,* International Symposium, From pattern formation to turbulence, 17-21 June 2019, Kloster Banz, Bavaria, Germany (Oral communication)
- MOTURI V., FUNFSCHILLING D., DUSEK J., *Path instabilities of rising bubbles,* International Colloquium on Bluff Body Flows (ICBBF) 4-5 July 2019, Strasbourg France (Oral communication)